Topological Phenomena in Tensor Network States of Quantum Spin Systems

Von der Fakultät für Mathematik, Informatik und Naturwissenschaften der RWTH Aachen University zur Erlangung des akademischen Grades eines Doktors der Naturwissenschaften genehmigte Dissertation

vorgelegt von
Mohsin Iqbal, M.Sc.
aus Karachi

Berichter: Priv.-Doz. Dr. rer. nat. Norbert Schuch
Prof. Dr. rer. nat. Stefan Weßel

Tag der mündlichen Prüfung: 03. May 2018

Diese Dissertation ist auf den Internetseiten der Universitätsbibliothek online verfügbar.

میری امی اور ابو کے نام

To my parents

Abstract

The focus of our investigations in this thesis is quantum spin systems in two dimensions. We examine phase transitions between topologically distinct phases of quantum matter using the framework of tensor network states. We study the phenomena of anyon condensation and confinement in the context of tensor network states where these two notions offer a robust probe to characterize the universal features of quantum phase transitions. We do a comprehensive study of the numerical methods enabled by the tensor network formalism for the study of quantum phase transitions. We map out the phase diagram of certain exotic phases of quantum matter (namely the $D(\mathbb{Z}_4)$ quantum double, the toric code, and the double semion model) and identify the order and the universality classes of the phase transitions between these distinct topological phases. We analyze the phase boundaries of the toric code and the double semion model which exhibit first and second order phase transitions.

We investigate the class of $\mathbb{Z}_2$-invariant tensor network states while taking in to account the spin rotation and lattice symmetries. The resulting tensor network states allow us to map the phase diagram of $\mathbb{Z}_2$ spin liquids. The behavior of the system at the phase boundaries of $\mathbb{Z}_2$ spin liquid is governed by the condensation of spinons and visions. We also present our preliminary findings regarding the $\mathbb{Z}_4$-invariant tensors with $SU(2)$ symmetry. This approach enables us to study the spin liquid states of the toric code and the double semion model in a unified framework.

We give a local tensor description for the approximate ground states of the Heisenberg antiferromagnet on the kagome lattice by using the variational manifolds of just three and five parameters in the gapped $\mathbb{Z}_2$ spin liquid phase. The approximation of the ground states we construct have an energy density that is remarkably close to the results from the state-of-the-art density matrix renormalization group and the exact diagonalization method. By analyzing the deconfinement of anyonic excitations, we also present our findings regarding the vicinity of the variational ground state in gapped $\mathbb{Z}_2$ spin liquid phase.

Zusammenfassung

Der Fokus unserer Untersuchungen in dieser Arbeit liegt auf Quantenspinsystemen in zwei Dimensionen. Wir untersuchen Phasenübergänge zwischen topologisch unterschiedlichen Phasen von Quantenmaterie mit Hilfe von Tensornetzwerkzuständen. Wir untersuchen die Phänomene der Anyon-Kondensierung und des Anyon-Confinement im Kontext von Tensornetzwerkzuständen, wo diese Konzepte ein robustes Mittel zur Charakterisierung der universellen Eigenschaften von Quantenphasenübergängen bieten. Wir führen eine umfassende Studie der numerischen Methoden zur Untersuchung von Quantenphasenübergängen durch, die durch den Tensornetzwerkformalismus erschlossen werden. Wir vermessen das Phasendiagramm von bestimmten exotischen Phasen von Quantenmaterie (der $D(\mathbb{Z}_4)$ "quantum double" Modelle, des "toric code" und des "double semion" Modells) und identifizieren die Ordnung und die Universalitätsklassen der Phasenübergänge zwischen diesen verschiedenen topologischen Phasen. Wir analysieren die Phasengrenzen des "toric code" und des "double semion" Modells, welche Phasenübergänge sowohl erster alsauch zweiter Ordnung aufweisen.

Wir untersuchen die Klasse der $\mathbb{Z}_2$-invarianten Tensornetzwerkzustände, bei denen wir Spinrotation und Gittersymmetrien mit einbeziehen. Die daraus resultierenden Tensornetzwerkzustände erlauben es uns, das Phasendiagramm von $\mathbb{Z}_2$-Spinflüssigkeiten zu vermessen. Das Verhalten des Systems an den Phasenrändern der $\mathbb{Z}_2$-Spinflüssigkeit wird durch die Kondensierung von Spinonen und Visonen bestimmt. Zudem präsentieren wir unsere Ergebnisse bezüglich der $\mathbb{Z}_4$-invarianten Tensoren mit $SU(2)$ Symmetrie. Diese Herangehensweise ermöglicht es uns, die Spinflüssigkeitszustände des toric code und des double semion Modells in einem einheitlichen Rahmen zu analysieren.

Wir präsentieren eine lokale Tensor-Beschreibung des näherungsweisen Grundzustands des Heisenberg Antiferromagneten auf dem Kagomegitter, wozu wir eine variationelle Mannigfaltigkeit von lediglich drei bzw. fünf Parametern in der $\mathbb{Z}_2$ Spinflüssigkeitsphase benötigen. Die Approximation der Grundzustände, die wir konstruieren, haben eine Energiedichte die bemerkenswert nah an den Ergebnissen liegt, die mit den Methoden hochoptimierter DMRG und exakter Diagonalisierung erzielt werden. Mithilfe der Analyse des Deconfinement von anyonischen Anregungen präsentieren wir ebenfalls unsere Ergebnisse bezüglich der Umgebung des variationellen Grundzustands in Spinflüssigkeitsphasen mit Bandlücke.

Contents

Chapter 1

Introduction

The field of quantum information has seen an unprecedented development in the recent years, and remarkable improvements have been made in our understanding of entanglement [1, 2]. Furthermore, there has been a cross-fertilization of ideas between the fields of quantum information and many-body strongly correlated systems. The framework of tensor networks is an embodiment of ideas which have been developed during the last three decades by hybridizing different concepts from the two fields of quantum computing and quantum many-body systems.

The most important lesson that has been learned is the realization that the entanglement plays a very crucial role in determining the physics of strongly correlated systems. The starting point in our quest for understanding the properties of the strongly correlated systems has to be the study of the 'structure' of entanglement between the different constituents of the system. The idea of tensor network states (which are also referred as projected entangled pair states (PEPS)) enables a systematic approach to investigate correlations between different components of the system [3]. And once we have that information, it is possible to construct a finite description of an infinite object (i.e., the many-body quantum state) in terms of local tensors. The tensor network approach has solved the representability problem for the class of quantum states which is relevant to describe the low energy properties of the systems and where the complexity of a naive approach would grow exponentially with the system size. It has also been the backbone of the new numerical tools which have allowed for the large-scale simulation of quantum systems on classical computers.

The existence of strong correlations in many body systems acts both as a curse and as a blessing. While on the one hand, the added complexity from these correlations prevents an explanation using the traditional approaches which are centered around the mean field theory, the strong coupling between subsystems also enrich the phase

diagram of strongly correlated spin systems. And these correlations are responsible for the emergence of 'exotic' phases of matter which are topologically ordered [4]. The topologically ordered phases cannot be described by the conventional ideas of local order parameter and symmetry breaking which were developed by Lev Landau during the first half of the last century [5, 6]. Topologically ordered systems lack the presence of local order parameters which are used to differentiate between distinct phases. Furthermore, topologically ordered systems allow for the presence of particles with anyonic exchange statistics and the seminal work of Kitaev et al. [7, 8] have shown that certain properties of topologically ordered systems can be used for the implementation of a fault-tolerant quantum computer.

A crucial insight into our understanding of topological order has been made during the last decade from the studies of topological systems using the framework of tensor networks. It has been found that a subtle structure in the local tensors is necessary for the description of topologically ordered systems [9–11]. Tensor networks have also played a very vital role in the better understanding of the quantities which act as the most natural analog of order parameters for the topologically ordered systems [12, 13]. A unified theory of quantum phases allows for the possibility of anyons (quasi-particle excitations) from a well-defined set. And in any quantum phase, there is a distinct subset of anyons which are deconfined (i.e., these anyons can independently exist) while the rest of the anyons are confined. Another closely related phenomenon is the idea of anyon condensation which characterizes the distinguishability between the topological sectors of an anyon and the quantum vacuum. The formalism of tensor networks enables us to quantify these qualitative notions. As a result, we can use the condensation and confinement of anyons as order parameters for topologically ordered systems. This approach is robust enough to be used for the study of phase transitions between distinct topological phases. The study of the class of topologically ordered systems and their phase transitions using these ideas is one of the leading topics of this thesis.

Historically, the earliest example of the state with a non-trivial topological order is resonating valence bond state. Anderson first studied the resonating valence bond state for the description of high-T_c superconductors [14]. Later, it was observed that the quantum phase of the resonating valence bond states shows features which are the hallmarks of a topologically ordered system [15]. Furthermore, by using the tools which have been developed using the formalism of tensor networks, it was shown rigorously that the topological order of the disordered spin-liquid resonating valence bond states on the kagome lattice is of the same type as the topological order of the Kiteav toric code model on the honeycomb [16, 17]. In this thesis, we extend the ideas of anyon condensation and confinement to construct the phase diagram of simplest spin liquids (namely the spin liquid of toric code topological order) [18]. Moreover, we also study the phase diagram

of another class of spin liquids where the topological order is characterized by the double semion model [19].

The realization of a quantum phase with a non-trivial topological order can be an important step for the implementation of a reliable quantum computer. One of the most challenging hurdles in this direction is due to the presence of many-body interactions in the Hamiltonian (e.g., in the case of Kiteav's toric code each interaction involves four sites), and these interactions can be very hard to engineer. Remarkably, it has been proposed by using the numerical method of density matrix renormalization group (DMRG) that the class of frustrated spin systems on the kagome lattice, where underlying Hamiltonians contain only nearest neighbor Heisenberg interactions, can have ground states which exhibit the topological order of the same type as the toric code model [20, 21]. Although there is a growing consensus on the conclusion that the ground states have the topological nature of toric code type, the debate is still open. One source of uncertainty is because the variational manifold in DMRG computations is characterized by an exceedingly large number of parameters. In this thesis, we construct a class of highly entangled quantum states where the variational manifold is parametrized by only very few parameters and an approximation of ground states with remarkably low energies can be obtained.

In short, the three main topics of this thesis are the study of anyon condensation and topological phase transitions, the investigation of the phase diagrams of the toric code and double semion spin liquids, and the construction of an efficient local tensor network description for the ground state of Heisenberg antiferromagnet on the kagome lattice in the gapped spin liquid phases. In the end, we also digress to analyze the geometric structure of reduced density matrices for the ground states of the Heisenberg antiferromagnet on the square lattice.

This thesis has been organized as follows,

- In the second chapter, we start by reviewing the fundamental notions of entanglement and tensors. We discuss the basic idea behind tensor network formalism and the modeling of many-body wavefunctions using tensor networks.
- Chapter 3 contains an overview of numerical tools and methods that have been developed using the formalism of tensor networks. We use these techniques later for the computation of quantities which are relevant to examine the topological phenomena in spin systems.
- In chapter 4, we present our findings regarding the study of topological order and topological phase transitions in a class of many-body systems which could be referred to by the $\mathbb{Z}_4$ topological order.

- In chapter 5, we construct the phase diagram of gapped $\mathbb{Z}_2$ spin liquid and present our findings regarding the phase diagram of double semion spin liquid.
- In Chapter 6, we give a constructive description of the quantum states which form good candidates for the ground state of the Heisenberg antiferromagnet on the kagome lattice.
- Chapter 7 contains the conclusions of this thesis and an outlook.

Publications

Most of the results in this thesis are based on the following publications/preprints:

Mohsin Iqbal, Kasper Duivenvoorden, and Norbert Schuch,
Study of anyon condensation and topological phase transitions from a $\mathbb{Z}_4$ topological phase using Projected Entangled Pair States,
arXiv:1712.04021 [cond-mat.str-el], 2017.

Mohsin Iqbal, Didier Poilblanc and Norbert Schuch,
Semionic resonating valence-bond states,
Phys. Rev. B 90, 115129, 2014.

Another publication where I contributed to the construction and analysis of $\mathbb{Z}_4$ family of states and did the numerics:

Kasper Duivenvoorden, Mohsin Iqbal, Jutho Haegeman, Frank Verstraete
and Norbert Schuch,
Entanglement phases as holographic duals of anyon condensates,
Phys. Rev. B 95, 235119, 2017.

Chapter 2

Tensor network states

One significant innovation in the context of Hamiltonian complexity is the development of Area laws which provide bounds on the entanglement entropy of different quantum systems. They have played a role which is similar to the role of complexity classes in the field of computational complexity. On the one hand, these bounds have justified our inability to solve certain quantum systems (i.e., the systems where entanglement entropy does not satisfy Area laws) as that would require an ansatz which contains highly entangled wavefunctions. On the other hand, the bounds provided by the Area laws have enabled the development of variational ansatzes which contain only the relevant quantum states.

Historically, the density matrix renormalization group (DMRG) is the first method which used the variational ansatz of tensor network states in 1D (i.e., matrix product states) to find the ground states of local Hamiltonians [22–24]. From the analytic point of view, the AKLT state (i.e., the ground state of AKLT Hamiltonian) is the first example of the non-trivial matrix product state [25].

The outline of the chapter is as follows. Firstly we begin with the brief description of the fundamental idea of entanglement. We describe the notion of a tensor and the basic operation of the tensor trace which is a natural mean for the composition of tensors. We then explain the formalism of tensor network states. Following on, we describe the tensor network construction of two wavefunctions (which are important for the purposes of this thesis) and the intuition behind the construction. In the last section, we give an application of tensor networks as a tool which can be used for finding the solution of certain classical counting problems.

2.1 Entanglement

Entanglement refers to the inseparability of a quantum state of a given system in terms of the constituting subsystems. The fundamental postulates of quantum mechanics for composite systems allow for the possibility of quantum states which cannot be decoupled as the tensor product of individual subsystems. Here, our discussion is restricted to the entanglement in pure quantum states. A quantum state is said to be 'entangled' if it cannot be written as a product state [26], i.e., for the bipartition A-B, a quantum state $|\psi\rangle_{\mathrm{AB}}$ is entangled if

$$|\psi\rangle_{\mathrm{AB}} \neq |\psi\rangle_{\mathrm{A}}|\psi\rangle_{\mathrm{B}}. \tag{2.1}$$

The quantum states of the form (2.1) give rise to some of the most counter intuitive effects in quantum mechanics which have applications in the field of quantum computing [27].

2.1.1 Entanglement entropy

The above described qualitative notion of entanglement can be quantified by using the Schmidt decomposition. Schmidt's theorem states that any bipartite quantum state can be decomposed as,

$$|\psi\rangle_{\mathrm{AB}} = \sum_i \lambda_i |i\rangle_{\mathrm{A}}|i\rangle_{\mathrm{B}}, \tag{2.2}$$

where $|i\rangle_{\mathrm{A}}$ ($|i\rangle_{\mathrm{B}}$) are orthonormal states of system A (B), and λ_i's are called the Schmidt coefficients with the property that the sum of their squares is equal to 1.

An important feature of Schmidt decomposition is that it allows us to retrieve the reduced density matrices of sub-systems A and B directly, i.e.,

$$\rho_{\mathrm{A}} = \sum_i \lambda_i^2 |i\rangle_{\mathrm{A}}\langle i|_{\mathrm{A}} \ , \quad \rho_{\mathrm{B}} = \sum_i \lambda_i^2 |i\rangle_{\mathrm{B}}\langle i|_{\mathrm{B}} \tag{2.3}$$

The appearance of Schmidt coefficients $\{\lambda_i\}$ in (2.2) and (2.3) reveals a fundamental connection between the 'inseparability' of a pure state and the 'mixedness' of the quantum states of the sub-systems. Entanglement of the quantum state is the same as the entropy of the reduced matrices, and one way to quantify these two notions is by using the measure known as *entanglement entropy*, and which can be defined as,

$$S = \sum_i \lambda_i^2 \log \lambda_i^2. \tag{2.4}$$

2.1.2 Entanglement structure of the ground states and Area laws

Entanglement entropy S is an extensive quantity, and for a generic quantum state, entanglement entropy of a region 'A' is expected to grow with the volume of the region A. But, remarkably for the ground states of the gapped local Hamiltonians the scaling of S of restrictive. The submanifolds of the full Hilbert space which are home to the ground states of local Hamiltonians share a similar restrictive scaling in the growth of their entanglement entropy. Given a bipartition A-B, the entanglement entropy grows in proportion to the surface area of the interface between region A and B.

$$S \propto A, \tag{2.5}$$

where A is the surface area. The relation (2.5) is termed as Area law. Area law has been proved rigorously for 1D systems by Hasting et al. [28], and there also exists a strong numerical evidence for the higher dimensional systems. The intuition behind (2.5) is the insight that the 'correlations' in the ground states of the gapped local Hamiltonian tend to live at the boundary of regions.

Remarkably, the relation (2.5) also holds for the ground state of topological systems with an additive correction (also called topological entanglement entropy) to compensate for long range entanglements [29–31].

2.2 Tensor

A tensor A with n-indices is a $d_1 \times d_2 \ldots \times d_n$ array of complex numbers (in general, this could be the elements of any field, but for this thesis, we restrict to the complex field $\mathbb{C}$).

It is very convenient to use graphical representations for the manipulations of tensors, e.g., the entries of the tensor A can be denoted as,

$A_{i_1 i_2 \ldots i_n} :=$ 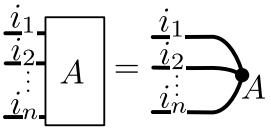 (2.6)

Each index i_k of A can take a value from a set $\mathbf{B}_k$ (the elements of $\mathbf{B}_k$ are the basis vectors of the vector space associated with the index) and $\|\mathbf{B}_k\| = d_k$. It is conventional to label the elements of the set $\mathbf{B}_k$ by a number from $\{0, 1, ..., d_k - 1\}$, but it is important to note that the value of an index is intrinsically a label for the element of $\mathbf{B}_k$.

Furthermore, tensors provide a natural way to generalize bilinear functions. In analogy with a matrix which for the given basis can specify a bilinear function, $f : \mathbb{C}^{d_1} \times \mathbb{C}^{d_2} \to \mathbb{C}$. The entries of a tensor, for the given basis, can encode a multi-linear function,

$$g : \mathbb{C}^{d_1} \times \mathbb{C}^{d_2} \times ...\mathbb{C}^{d_n} \to \mathbb{C}.$$

2.2.1 Parallel string processor

Another useful approach, which is reasonably intuitive in the context of quantum information, is to consider tensors as machines which could process strings in parallel.

We begin by first defining the notion of a 'string'. Given an alphabet $\Sigma^k = \{0, 1, ..., d_k-1\}$ that is a set of d_k letters, an n-letter string is an element of $\Sigma^1 \times \Sigma^2 \times ...\Sigma^n$. E.g., '0011' is a 4-letter string, if the alphabets $\Sigma^k = \{0, 1\}\ \forall\ k$.

Now, a tensor can be interpreted as a quantum machine which takes as an input a fixed length string and produces a fixed length output string. But in contrast to a classical device, a tensor can also process a superposition of strings. To elaborate we consider a flip tensor X. The tensor X has $2n$ indices (n input plus n output indices), each index takes a value from the alphabet $\Sigma = \{0, 1\}$. The tensor X process the value on the input index and puts it on the output index after doing a flip. If $n = 2$, then the action of flip tensor can be represented as,

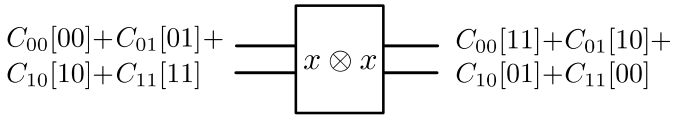

, (2.7)

where $x = \begin{bmatrix} 0 & 1 \\ 1 & 0 \end{bmatrix}$ is a Pauli matrix.

2.2.2 Tensor trace

A vital operation which enables the composition of tensors is tensor trace. It corresponds to picking two indices from the same or different tensors and identifying these indices with each other by summing over their possible values. Given two tensors $A_{i_1 i_2 i_3, i}$ and $B_{j_1 j_2 j_3, j}$, the trace operation on one of their indices can be given by,

$$C_{i_1 i_2 i_3, j_1 j_2 j_3} = \sum_i A_{i_1 i_2 i_3, i} B_{j_1 j_2 j_3, i} =$$

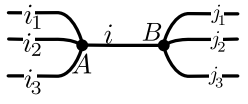

. (2.8)

2.3 Tensor network states

One of the most severe difficulties in the study of many-body systems lies in representing the quantum state efficiently on a classical computer. The size of the state space grows exponentially with the system size and the specification of the generic quantum state,

$$|\psi\rangle = \sum_{i_k \in \{0,1,...d-1\} \forall k} C_{i_1,i_2,...i_N} |i_1, i_2, ...i_N\rangle, \tag{2.9}$$

requires $O(d^N)$ complex numbers.

As we discussed earlier in Sec. 2.1, Area laws put a strict bound on the entanglement entropy for the ground state of gapped local Hamiltonians. The most significant development which has enabled to take advantage of low entanglement entropy requirements for the ground state was made in [3], where Verstraete et al. constructed a class of many-body wavefunctions which they termed as projected entangled pair states (PEPS). PEPS by construction satisfy the Area law of entanglement entropy with a very important property that these states have an efficient description in terms of local tensors. The class of projected entangled pair states can also be referred as tensor network states.

The important idea is first to identify the entanglement structure (i.e., how the individual constituents of the systems are connected with each other) and then use it for the representation of many-body wavefunctions. The *entanglement degrees* or the *virtual indices* of tensors in the tensor network or PEPS framework enable a natural approach to encode the quantum correlations. The transformation from the global object to a description in terms of local tensors can be given as,

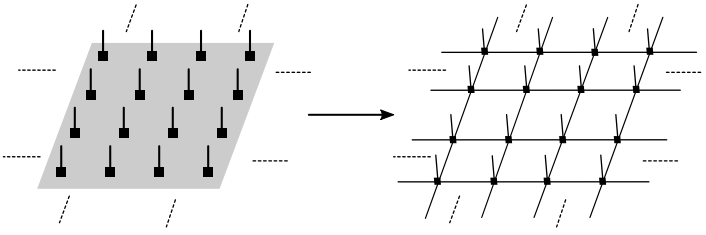

The applications of PEPS have been two-fold. On the one hand, they have to lead to the development of numerical methods for the finding the ground states of local Hamiltonians where the underlying ansatz is characterized by the tensor network states. On the other hand and perhaps more importantly, the analysis of local tensors and the study of their symmetries and different structures have revealed the otherwise hidden nature of quantum phases in strongly correlated systems.

2.4 Modeling wavefunctions using tensor networks

The tensor network framework enables a local description of objects (i.e., many body wavefunctions) with highly non-local components. The modeling of many-body quantum state in terms of a local tensor involves an analysis of the properties of the wavefunction at the smallest possible scale. The idea is to identify a set of local configurations (i.e., a set of 'tilling patterns') that the wavefunction can take and a set of rules under which these tiling patterns can be glued to form all the valid *global configurations*. The local tensor can be thought of as a device in which the information about the set of tiling patterns and the set of gluing rules can be encoded.

Furthermore, the global wavefunction is not only a superposition of *extended objects*, but different configurations in the superpositions could also have different amplitudes. If there is an underlying local rule which pertains to the generation of the overall amplitude of the configuration, then that rule can also be enforced in the local tensor.

In the following, we will describe the tensor network construction of two quantum states, namely the toric code model and the nearest neighbor resonating valence bond state. The first proposed tensor network description of these wavefunctions can be found in [32, 33]. These two states contain the following two features which are the essential ingredients to highlight the power of tensor network methods fully.

- Different configurations in the superposition contain objects which can be as large as the system itself.
- The number of possible configurations is constrained, but it is large enough that there is no efficient way to enumerate all of them.

2.4.1 Toric code model

The quantum state we first construct is the ground state of Kiteav's toric code Hamiltonian on the hexagonal lattice [7], where each site on the edge of the lattice is comprised of a qubit. The state can be understood as the superposition of all the possible closed loop string configurations. Here we refer to qubit in the state $|1\rangle$ ($|0\rangle$) as a 'string' ('empty site'). The wavefunction can be written pictorially as,

$|\psi_{\mathrm{TC}}\rangle =$ 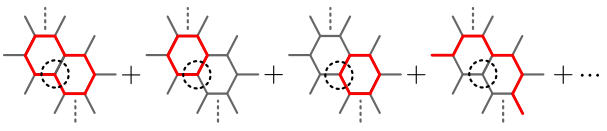 (2.10)

The above diagram gives the local view of different global configurations. Red lines on the edges indicate strings. At any vertex of the hexagonal lattice, there could be four possible configurations. In the above representation, the vertex marked by a dashed circle shows the four possibilities. Either there is a string on the two legs of the vertex, or all the vertices are free. The four local configurations can be encoded by defining a vertex tensor as,

$$E = \begin{array}{c} \alpha_1 \\ \alpha_2 \quad \alpha_3 \end{array} = \begin{cases} 1 & \alpha_1 + \alpha_2 + \alpha_3 = 0 \bmod 2 \\ 0 & \text{otherwise,} \end{cases} \tag{2.11}$$

where $\alpha_1, \alpha_2, \alpha_3 \in \{0, 1\}$. The entries of vertex tensor E are non-zeros only if the parity of $\alpha_1 + \alpha_2 + \alpha_3$ is even. After placing the tensor E on each vertex of the hexagonal lattice, the next step is to define the on-site tensor P.

$$P = \begin{array}{c} s \\ \alpha_1 \quad \alpha_2 \end{array} = \delta_{\alpha_1 s}\delta_{\alpha_2 s} \tag{2.12}$$

where $s \in \{0, 1\}$. The tensor P copies the information on the edge (i.e., whether or not there is a string on the edge) to the physical index. The resulting tensor network of the toric code wavefunction on the hexagonal lattice can be written as,

$$|\psi_{\text{TC}}\rangle = \tag{2.13}$$

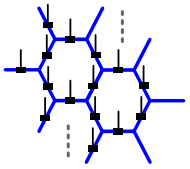

2.4.2 Resonating valence bond state

The resonating valence bond state was introduced by Linus Pauling [34] as an approach to extend the resonance of bonds in the benzene ring to the whole lattice. The resonating valence bond wavefunction is a superposition of all the nearest neighbor singlet pairings (or coverings). The singlets could be long ranged in general, but here we restrict to nearest neighbor pairings on the kagome lattice. The reason for using the kagome lattice will become apparent later in the thesis. The superposition of different singlet pairings can be written pictorially as,

$$|\psi_{\text{RVB}}\rangle = \tag{2.14}$$

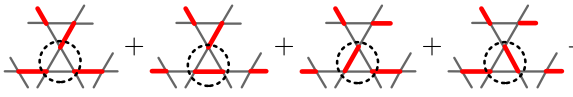

Red lines on the edge indicate a singlet. Locally each triangle of the kagome lattice could be in one of the four possible configurations (this can be seen in the case of the triangle with the dashed circle). In three configurations there is a singlet on one edge

of the triangle and one configuration all the edges are free. Similar to the case of toric code, the singlet configurations can be encoded by defining a vertex tensor E, and it is placed inside each triangle of the kagome lattice.

$E =$ 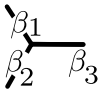 $= \begin{cases} \sigma_{\beta_2\beta_3} & \beta_1 = 2 \\ \sigma_{\beta_3\beta_1} & \beta_2 = 2 \\ \sigma_{\beta_1\beta_2} & \beta_3 = 2 \\ 1 & \beta_1 = \beta_2 = \beta_3 = 2 \\ 0 & \text{otherwise,} \end{cases}$ (2.15)

where $\beta_1, \beta_2, \beta_3 \in \{0, 1, 2\}$, and the matrix $\sigma = \text{diag}\left(\frac{1}{\sqrt{2}}\begin{pmatrix} 0 & -1 \\ 1 & 0 \end{pmatrix},\ 0\right)$. The next step is to define an on-site tensor which ensures that each vertex is paired with exactly one vertex via a singlet.

$P =$ 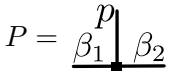 $= \begin{cases} \delta_{\beta_1 p} & \beta_2 = 2 \\ \delta_{\beta_2 p} & \beta_1 = 2 \\ 0 & \text{otherwise,} \end{cases}$ (2.16)

where $p \in \{0, 1\}$. By placing each vertex tensor E inside each triangle and on-site tensor P at each vertex of the kagome, we get the tensor network of resonating valence bond wavefunction.

$|\psi_{\text{RVB}}\rangle =$ 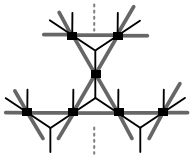 (2.17)

2.5 Tensor networks as a counting device

Tensor networks also offer a robust tool which could be used to count the number of possible solutions in different *enumeration problems*. Local tensors can be used to locally impose multiple constraints, and the contraction of these tensors can be used to simultaneously sum up the number of possible solutions.

Here, we review two problems from Project Euler (https://projecteuler.net) and we use these two problems to highlight the usefulness of this approach.

2.5.1 Problem 15: Lattice paths

We are given a 2D grid (Fig. 2.1a) with two points of interest (S and D) at the diagonal corners and the goal is to find the number of possible paths from S to D. Each path also has the constraint that it can be traversed only by making moves to the right and down (https://projecteuler.net/problem=15).

Tensor network solution

Given a solution (a path from S to D), each edge on the grid has two possibilities. It is either free or lies in the path, and these possibilities can be labeled as '0' and '1' respectively. Furthermore, for every vertex in the grid except the boundary and corner vertices, we have the following possibilities for every solution.

1. All the edges of the vertex are free, i.e., they can be labeled as '0'.
2. The vertex is traversed by the path. The path hits the vertex from the left or top edge, so exactly one these edges lies in the path. Similarly, the path leaves the vertex from the right or the bottom edge, and exactly one of these edges is occupied.

The following definition of the vertex tensor A summarized the above possibilities (or constraints).

$$A_{abcd} = \quad \begin{matrix} & d & \\ a & + & c \\ & b & \end{matrix} \quad = \begin{cases} 1 & if\ a = b = c = d = 0 \\ 1 & if\ a \oplus d = b \oplus c = 1 \\ 0 & \text{otherwise} \end{cases} \tag{2.18}$$

Here, we label the four indices (one corresponding to each edge) by a, b, c and d, and each index could take two values '0' and '1'.

The vertices at the boundary of the grid also have similar constraints for every solution.

1. All the edges from the vertex are free.
2. Assuming that the vertex is on the left boundary and the vertex lies in the path. The path hits the vertex from the top and leaves either from the right edge and or from the bottom.

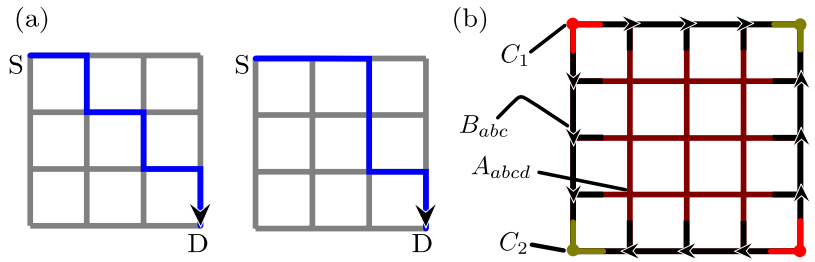

FIGURE 2.1: (a) Two possible solutions with endpoints at the diagonal corners. (b) Tensor network to count the number of paths on a 4×4 grid.

These constraints on the boundary vertices can be specified as

$$B_{abc} = \quad = \begin{cases} 1 & if\ a = b = c = 0 \\ 1 & if\ a = 1, b \oplus c = 0 \\ 0 & \text{otherwise} \end{cases} \tag{2.19}$$

Note that the arrowhead points in the direction of the index labeled as b.

Vertices at the start 'S' and at the destination 'D' of the path have the constraint that exactly one of their edges lies in the path. Similarly, the vertices at the off-diagonal corners of the grid have the constraint that either both of their edges are occupied, or both of them are free. We specify these constraints by the following definition of corner tensors.

$$C_1 = \quad = \begin{cases} 1 & if\ a \neq b \\ 0 & \text{otherwise} \end{cases}, \qquad C_2 = \quad = \begin{cases} 1 & if\ a = b \\ 0 & \text{otherwise} \end{cases}, \tag{2.20}$$

The contraction of resulting tensor network (Fig. 2.1b) gives a number which represents the sum of all the possibilities. It is important to emphasize the robustness of this approach. The tensor network description can be easily modified to find the number of paths with different endpoints and different lattice structures.

2.5.2 Problem 393: Migrating ants

Consider an $n \times n$ square lattice. Each square contains exactly one ant (Fig. 2.2a). All the ants want to move simultaneously to the neighboring squares. The swapping of homes between two ants is not allowed (i.e., no two ants can cross the same edge simultaneously). The problem is to count the number of all the possible migrations (https://projecteuler.net/problem=393).

Tensor network solution

For every solution (a possible migration of ants), we get a pattern of arrows on the dual lattice of the 2D grid. A possible migration of ants is given in Fig. 2.2b. Incoming (outgoing) arrow on the edge of a vertex specifies the direction of entering (leaving) ant. So, for every solution, each side on the dual grid is in one of the three possible states. In one case it is free, and in the other two cases, it has an arrow on it pointing in one of the two possible directions. We label these possibilities by '0', '1', and '2' respectively.

On the four edges of every vertex, we have exactly one incoming arrow and one outgoing arrow, and the two edges are free. These constraints can be summarized as

$$A_{a_1a_2a_3a_4} = \quad = \begin{cases} 1 & if\ a_1 + a_2 + a_3 + a_4 = 3,\ (a_i = a_j = 0,\ i \neq j) \\ 0 & \text{otherwise} \end{cases} \tag{2.21}$$

Each of the four indices a_i can take three values '0', '1', and '2'.

In the case of vertices at the boundary, the constraints are given by

$$B_{a_1a_2a_3} = \quad = \begin{cases} 1 & if\ a_1 + a_2 + a_3 = 3,\ a_i = 0 \\ 0 & \text{otherwise} \end{cases} \tag{2.22}$$

On the three edges of boundary vertex, we have one incoming arrow, one outgoing arrow and precisely one edge is free.

Edges of the corner vertex have exactly one incoming arrow and one outgoing arrow.

$$C = \quad = \begin{cases} 1 & if\ a_1 + a_2 = 3 \\ 0 & \text{otherwise} \end{cases}. \tag{2.23}$$

By contracting out the indices of the tensor network on the dual lattice (Fig. 2.2c), we get the count of all the possible ant migrations.

2.6 Summary

We have reviewed that the Area laws bound the scaling of entanglement entropy in the ground states of local Hamiltonians. The formalism of tensor network states allows us to access the quantum states which satisfy Area law by construction and take advantage of the low requirements of entanglement entropy for the ground states of gapped local

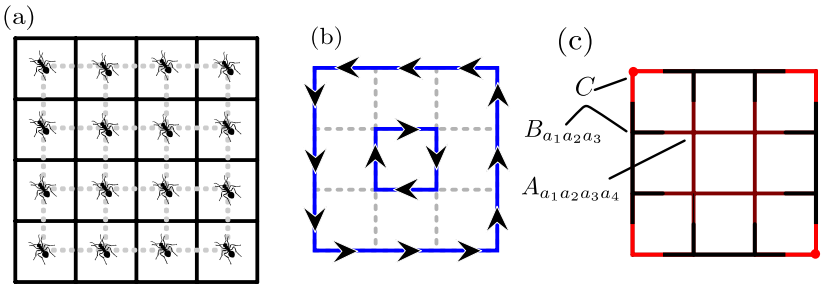

FIGURE 2.2: (a) 4×4 grid. Dashed gray lines indicate the dual lattice. (b) A possible solution (migration of ants). Blue lines with an arrow on the edges of dual lattice indicate the direction of ant movement. (c) Tensor network construction of the dual lattice.

Hamiltonians. Furthermore, the tensor networks give an efficient description of many-body quantum states that scales polynomially with the system size.

Chapter 3

Numerical methods

The tensor network formalism enables an efficient description of many-body wavefunctions in the form of local tensors which can be studied analytically. The manifold which is defined by the tensor network states essentially contains all the information about the properties of the system at low temperature where the underlying Hamiltonian contains only local interactions. This insight has lead to the development of numerical techniques which use tensor network states with finite bond dimension as an ansatz for finding the ground states of the system. These techniques can be divided into two broad categories, (1) time-evolving block decimation (TEBD) algorithms [35–37], and (2) variational methods such as density matrix renormalization group (DMRG) [22]. Both approaches have their variants to deal with systems in the thermodynamic limit [38, 39]. These methods are developed enough that they can be used reliably in the case of 1D systems, and recently there have also been some major developments in the case of 2D systems [40, 41].

But an essential problem in the case of 2D systems is that even the complexity of finding an exact contraction of a tensor network grows exponentially with the system size. The contraction of tensors is an essential step in finding the expectation value of local operators and a lot of effort in the recent years has been invested in obtaining an approximate contraction of tensor networks [42]. Furthermore, it is also essential that the numerical methods should allow us to handle an infinitely large number of particles (the same way we observe in the natural world), only then it would be possible to see the emergence of exotic phenomena like topological order in the quantum simulations. So the focus of our discussion in this chapter will be on the strategies for the contraction of semi-infinite (i.e., infinite cylindrical geometries with finite perimeter) and infinite tensor networks. Along the way, we also describe the computation of quantities which are essential for determining the entanglement behavior and the quantum phase of the

system. All the tensor network techniques which we review in the chapter will be used in our studies of topological phenomena and quantum phase transitions in the later chapters.

3.1 Semi-infinite systems

The physical properties of finite systems suffer from strong boundary effects, and to have a reliable estimate of an observable; one has to do finite size scaling by growing the systems' size in two dimensions. One approach to partially solve the scaling problem is to do computations on infinite systems with cylindrical geometries. This approach can be implemented without incurring a significant overhead in the complexity, and the main advantage of this method is that it does not suffer from boundary effects, and only by examining the behavior of the computed quantity as the function of the perimeter of the cylinder, it is possible to get a very good approximation.

In the next subsection, we will first elaborate the underlying setup and describe the method for computing the expectation values of local observables. In the later subsections, we will explain an approach for calculating the entanglement spectrum and entanglement entropy for cylindrical geometries which was first described in [43, 44]. In the end, we will define a procedure for computing the fidelity of quantum states and the fidelity susceptibility which are some of the essential probes to investigate the behavior of quantum phase transitions.

3.1.1 Expectation value of local observables

Consider a system on the infinite cylinder ($N_h \to \infty$) with the finite perimeter N_v. The translation invariant description of the quantum state $|\psi\rangle$ is given by an on-site tensor A with a physical index of dimension d and four virtual indices each of dimension D. Quantum state $|\psi\rangle$ as a tensor network on the cylinder can be given as,

$|\psi\rangle =$ 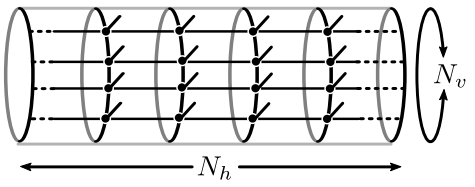 , where $A =$ 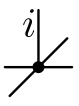 (3.1)

Now to proceed with the contraction of the tensor network in a systematic manner, we define trivial and non-trivial double tensors as $\mathbb{E} := \sum_i A^i \otimes A^{i*}$ and $\mathbb{E}_O := \sum_{i,j} A^i O^{ij} \otimes A^{j*}$

respectively. The non-trivial double tensor $\mathbb{E}_O$ is obtained by sandwiching the local operator O between the physical indices of on-site tensors. These tensors can be represented graphically as

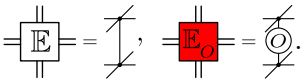

(3.2)

By using the above definitions of double tensors; the expectation value of a local observable O which is acting on a site in the middle of an infinitely long cylinder can be graphically represented as,

$\langle\psi|O|\psi\rangle =$

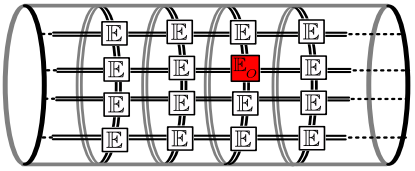

(3.3)

An object of fundamental importance which will also appear later for doing numerics in the case of infinite systems is the transfer operator which is obtained by blocking a chain of double tensors $\mathbb{E}$ in one direction. In this case, the transfer operator $\mathbb{T}$ is defined as,

$\mathbb{T} :=$

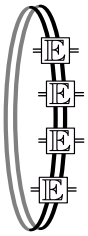

(3.4)

After defining the transfer operator, the next important step in computing the expectation value of local observables is the calculation of the fixed points of the transfer matrix. Let $(\sigma_L|$ and $|\sigma_R)$ be the left and right eigenvectors of the transfer operator with the largest eigenvalue λ_0, i.e., the transfer operator acts on $(\sigma_L|$ and $|\sigma_R)$ in the following manner,

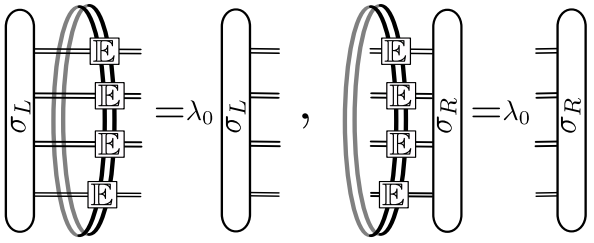

(3.5)

It is important to note here that the memory requirements for storing the transfer operator $\mathbb{T}$ grow as $(D^4)^{N_v}$, and so it is not feasible to explicitly construct the transfer matrix. This problem can be fixed by computing the left and right eigenvectors by an iterative eigenvalue solver. These routines do not explicitly require the transfer operator

as an input, but the only action of transfer operator on an input vector has to be specified. Although the simple usage of iterative solvers restricts the computation of eigenvectors to cylinders with small perimeter, it is possible to use implementations of iterative solvers which have been optimized to fully exploit the computational power of shared and distributed memory architectures or even the GPUs.

Assuming that the largest eigenvalue of transfer operator is unique, in the thermodynamic limit, the contribution from only the largest eigenvector survives, and so the expectation value can be written as,

$$\langle\psi|O|\psi\rangle \approx \lim_{N_h\to\infty} \lambda_0^{N_h-1}(\sigma_L|\mathbb{T}_O|\sigma_R),$$

where $\mathbb{T}_O$ is the transfer operator with a non-trivial double tensor $\mathbb{E}_O$. The normalized expectation value of the local observable can be calculated as,

$$\begin{aligned}\langle\hat{O}\rangle &:= \frac{\langle\psi|O|\psi\rangle}{\langle\psi|\psi\rangle} \\ &\approx \frac{\lambda_0^{N_h-1}\,(\sigma_L|\mathbb{T}_O|\sigma_R)}{\lambda_0^{N_h}\,(\sigma_L|\sigma_R)} = \frac{(\sigma_L|\mathbb{T}_O|\sigma_R)}{\lambda_0\,(\sigma_L|\sigma_R)}.\end{aligned} \tag{3.6}$$

3.1.2 Entanglement spectrum

Area laws quantify the entanglement entropy of a region in terms of the region's boundary for the ground state of gapped quantum systems. Following this observation, a remarkable result came from the understanding of perhaps an even more profound connection between the whole entanglement spectrum of the region in the *bulk* and the energy spectrum of certain *boundary models* [45]. Furthermore, in the context of tensor networks it was shown by Cirac et al. in [43] that the boundary of the region can be assigned a Hamiltonian whose spectrum corresponds to the entanglement spectrum of the bulk. Moreover, tensor network formalism not only enables the construction of states with an entanglement structure prescribed by the Area laws, it also allows for the construction of these boundary Hamiltonians which act on the entanglement degrees of the tensor network.

The method to compute the entanglement spectrum of the system on infinite cylinder ($N_h \to \infty$) with finite perimeter (N_v) was described by Schuch et al. in [44]. Given a translation invariant tensor network state for an infinite system partitioned in the

middle,

$|\psi\rangle_{AB} =$ 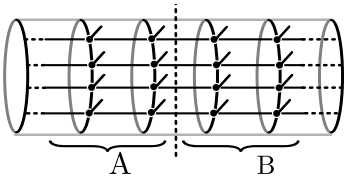

, (3.7)

with dimensions d and D for the physical and virtual indices respectively. The size of the reduced density matrix grows exponentially with N_h and N_v and it is an infinite object as $N_h \to \infty$. But quite remarkably the spectrum of ρ_A can be computed by relating the reduced density matrix to a finite object via an isometry (see [44]), i.e.,

$$\rho_A = V\sqrt{\sigma_L}\sigma_r\sqrt{\sigma_L}V^\dagger, \tag{3.8}$$

where σ_L and σ_r are the left and right fixed points of the transfer operator as we discussed earlier in (3.5) and $\sqrt{\sigma_L}\sigma_R\sqrt{\sigma_L}$ is a $D^{N_v} \times D^{N_v}$ matrix. V is an isometry and since the spectrum is preserved under the transformation by V, the entanglement spectrum of a bipartition in (3.7) can be computed by doing the eigenvalue decomposition on $\sqrt{\sigma_L}\sigma_R\sqrt{\sigma_L}$.

Once we have computed $\sqrt{\sigma_L}\sigma_R\sqrt{\sigma_L}$, the boundary Hamiltonian H_b can be obtained by taking its logarithm [43],

$$H_b := -\ln(\sqrt{\sigma_L}\sigma_R\sqrt{\sigma_L}).$$

Later, we will use the above definition for computing the boundary Hamiltonian of a twisted spin liquid state (i.e., the semionic resonating valence bond state).

3.1.3 Entanglement entropy

A measure of fundamental interest which quantifies the entanglement between subsystems A and B of a bipartition is the Von Neumann entanglement entropy $\mathcal{S}$. It is defined as

$$\mathcal{S}(\rho_A) := -\mathrm{Tr}(\rho_A \log \rho_A) \tag{3.9}$$

where ρ_A is the reduced density matrix of subsystem A. Let $\{\lambda_i\}_{i=1}^{D^{N_V}}$ be the eigenvalue decomposition of $\sqrt{\sigma_L}\sigma_r\sqrt{\sigma_L}$, then by using (3.8), the Von Neumann entanglement entropy can be computed as

$$\mathcal{S}(\rho_A) = -\sum_i \lambda_i \log \lambda_i \tag{3.10}$$

3.1.4 Fidelity per site

Quantum state fidelity defines a measure of *distinguishability* between two different states. Since for any non-zero δ, the overlap $\langle\psi(\theta)|\psi(\theta+\delta)\rangle$ between the quantum states goes to zero in the thermodynamic limit (also called Anderson's orthogonality catastrophe), a meaningful measure of the distinguishability of quantum states can only be an intensive quantity which does not depend on the system size.

An intensive quantity called fidelity per site for quantum states $|\theta_1\rangle := |\psi(\theta=\theta_1)\rangle$ and $|\theta_2\rangle := |\psi(\theta=\theta_2)\rangle$ is defined as

$$f\left(\theta_1,\theta_2\right) := \left|\frac{\langle\theta_2|\theta_1\rangle}{\sqrt{\langle\theta_2|\theta_2\rangle\langle\theta_1|\theta_1\rangle}}\right|^{1/N_h N_v} \tag{3.11}$$

The notion of quantum state fidelity was first applied by Zanardi et al. for the study of quantum phase transitions [46]. Later, applications of fidelity per site in the context of tensor networks were investigated in [47, 48].

In order to compute the fidelity per site for tensor network states on infinite cylinders, let $\lambda_0\left(\theta_i,\theta_j\right)$ be the largest eigenvalue of transfer operator $\mathbb{T}\left(\theta_i,\theta_j\right)$. Then as $N_h\to\infty$, the fidelity per site can be approximated as

$$f\left(\theta_1,\theta_2\right) \approx \left|\frac{\lambda_0(\theta_1,\theta_2)}{\sqrt{\lambda_0(\theta_2,\theta_2)\lambda_0(\theta_1,\theta_1)}}\right|^{1/N_v}. \tag{3.12}$$

3.1.5 Fidelity susceptibility

Given a quantum state parametrized by the variable θ, the *sensitivity* of fidelity per site (or the norm per site) for $|\psi(\theta)\rangle$ to an infinitesimal change in θ can be used as useful probe for the study of quantum phase transitions [49]. Fidelity susceptibility χ_F quantifies this sensitivity and it is defined as the second derivative of fidelity per site,

$$\chi_F := \lim_{\delta\to 0}\frac{2\left(1-f\left(\theta,\theta+\delta\right)\right)}{\delta^2} \tag{3.13}$$

We will later use the notion of fidelity susceptibility to characterize the behavior of quantum phase transitions.

3.2 Infinite systems

Now, we describe different numerical approaches which have been designed to handle computations for 2D systems directly in the thermodynamic limit. Our focus here would be to explain techniques which assume translation invariant local tensor network description of the 2D wavefunction and the goal would be to answer different qualitative and quantitative questions regarding its properties. In the end, we will briefly review a method by Haegeman et al. [50] to compute the spectrum of transfer operator in the thermodynamic limit by using the excitation ansatz.

We begin by describing the notion of overlap per site and a method to find an approximation of MPS with lower bond dimension. These ideas will be used to obtain the fixed points of transfer operator which is an essential ingredient to find the answers to many questions.

3.2.1 Overlap per site - 1D

Overlap per site (also called fidelity per site f, as we discussed earlier for semi-infinite 2D systems) is a measure to quantify distinguishability between two quantum states in the thermodynamic limit,

$$f(\phi,\psi) := \lim_{N\to\infty} \left| \frac{\langle\psi|\phi\rangle}{\sqrt{\langle\phi|\phi\rangle\langle\psi|\psi\rangle}} \right|^{1/N}.$$

Let A and B be the MPS tensors, and $|\psi(A)\rangle$ and $|\psi(B)\rangle$ be the corresponding translation invariant MPSs, then the overlap per site can be computed as

$$f = \frac{\lambda_{AB}}{\sqrt{\lambda_{AA}\lambda_{BB}}} \tag{3.14}$$

where λ_{AB} is the largest eigenvalue of the double tensor $\mathbb{E}_{AB} = \sum_i A_i \otimes B_i^\dagger$, which is obtained by contracting the physical indices of A and B.

3.2.2 Approximation of MPSs

We describe an approach to truncate the bond dimension of an MPS in the thermodynamic limit. An extensive review of different approximation techniques can be found in [42]. The idea is to find an MPS of lower bond dimension χ with reduced density matrices which best approximate the density matrices of the original state. First, we describe an approach which uses singular value decomposition (SVD) to truncate single site MPSs. Second, we discuss the extension of this method to truncate multi-site MPSs.

3.2.3 Single-site MPSs

We want to finds an approximation of tensor A with a tensor A' such that the overlap between $|\psi(A)\rangle$ and $|\psi(A')\rangle$ is maximized. Pictorially,

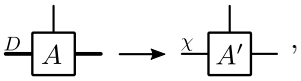

(3.15)

where $D > \chi$. An approximation with the mentioned properties can be computed by truncating the number of Schmidt coefficients to χ. The Schmidt coefficients can be accessed via the canonical representation (described by Garcia et al. [51]) of A. We want to find the matrix L such that

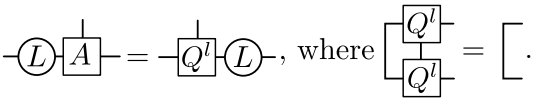

(3.16)

L can be computed by repeated applications of QR decomposition (see Algo. 1). Similarly, the matrix R which characterize the right canonical representation of A such that

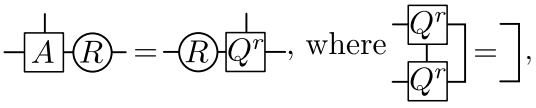

(3.17)

can be found using the similar procedure.

Given that we have the matrices L and R satisfying above two equations, we can define projections which could do truncation on the Schmidt coefficients. Since,

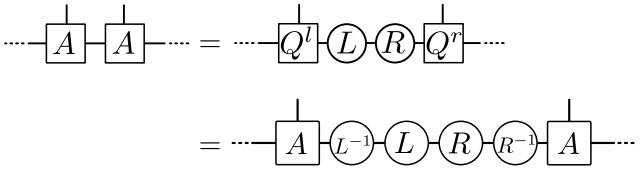

(3.18)

If $LR = U\Sigma V^\dagger$ is the singular value decomposition, where the matrix Σ contains the Schmidt coefficients for a bipartition in the middle of infinity, then

$$L^{-1}LRR^{-1} = RV\Sigma^{-1/2}\ \Sigma^{-1/2}U^\dagger L. \tag{3.19}$$

Let $P^r := RV\widetilde{\Sigma}^{-1/2}$ and $P^l := \widetilde{\Sigma}^{-1/2}U^\dagger L$ be the projectors. Matrix $\widetilde{\Sigma}$ represents Σ truncated to χ Schmidt coefficients. The approximate representation of A is obtained by applying projections P^l and P^r such that,

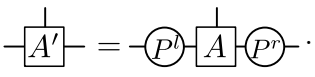

(3.20)

Algorithm 1: Find the matrix L by orthogonalization of the MPS from the left.

function LeftOrth;
Input : MPS tensor A, tolerance tol.
$A \leftarrow reshape(A)$
// The dimensions of tensor A are $D \times d \times D$. Reshape A to be a $Dd \times D$ matrix.
$A_{temp} = A$; // Initialize A_{temp} with A.
$L_{temp} = 0$, $err = 1$;
while $err > tol$ **do**
  $L = qr(A_{temp})$
  // Q-less QR-decomposition of A_{temp}. QR-decomposition is unique up to the sign of each row of L. Fix the sign, such that each diagonal entry of L is positive.
  $nL = 1/norm(L)$
  $L = nL \times L$; // Normalize the matrix L.
  $err = norm(L - L_{temp})$
  $A_{temp} = L \times A$
end
Output: L

3.2.4 Multi-site MPSs

The MPS representation of $|\psi\rangle$ is characterized by m tensors

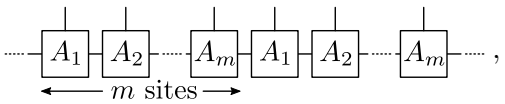

, (3.21)

and the goal is to find an approximation A'_a for each A_a with lower bond dimension. As in the case of the single site, to construct the projections, we need the Schmidt coefficients for bipartition across cuts between different A_as. First, we compute the matrices L_a and R_a for $a \in \{1, 2, ..m\}$ such that

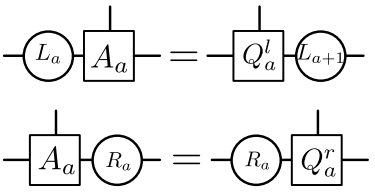

, (3.22)

where $\sum_i {Q^l_{a,i}}^\dagger Q^l_{a,i} = \mathbb{I}_{D\times D}$ and $\sum_i Q^r_{a,i} {Q^r_{a,i}}^\dagger = \mathbb{I}_{D\times D}$ for each a. This can be done by extending Algo. 1 to the case of multi-site MPSs (see Algo. 2).

Similar to single-site case, we insert an identity $L_a^{-1} L_a R_a R_a^{-1}$ between sites $a-1$ and a,

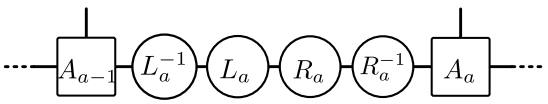

(3.23)

Algorithm 2: Find matrices $L[a]$ with $a \in \{1, 2.., m\}$ by orthogonalization from the left.

function LeftOrthMultiSite;
Input : MPS tensor $A[1:m]$, tolerance tol.
$A[1:m] \leftarrow reshape(A[1:m])$;
// The dimensions of tensors $A[a]$ are $D \times d \times D$. Reshape $A[a]$ to be $Dd \times D$ matrices.
$A_{temp}[1:m] = A[1:m]$; // Initialize A_{temp}'s with A's.
$L_{temp}[1:m] = 0$, $maxErr = 1$;
$a = 1$;
while $maxErr > tol$ **do**
  $L[a] = qr(A_{temp}[a])$
  $nL = 1/norm(L[a])$
  $L[a] = nL \times L[a]$; // Normalize the matrix $L[a]$.
  $err[a] = norm(L[a] - L_{temp}[a])$
  $A_{temp}[a] = L[a] \times A[a]$
  $a = mod(a, m) + 1$; // $mod(a, m)$ computes the remainder of m divided by a.
  if $a = 1$ **then**
    $maxErr = max(err)$
  end
end
Output: $L[1:m]$

Let $U_a \Sigma_a V_a^\dagger$ be the singular value decomposition of $L_a R_a$, then

$$\begin{aligned} L_a^{-1} L_a R_a R_a^{-1} &= R_a V_a \Sigma_a^{-1/2} \; \Sigma_a^{-1/2} U_a^\dagger L_a \\ &\approx R_a V_a \widetilde{\Sigma}_a^{-1/2} \; \widetilde{\Sigma}_a^{-1/2} U_a^\dagger L_a \end{aligned} \tag{3.24}$$

with $P_a^l := R_a V_a \widetilde{\Sigma}_a^{-1/2}$ and $P_a^r := \widetilde{\Sigma}_{a+1}^{-1/2} U_{a+1}^\dagger L_{a+1}$, the truncated representation of A_a is obtained by

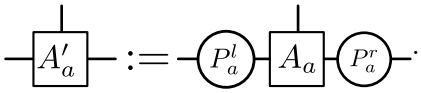

(3.25)

3.2.5 Fixed points of the transfer operator

The transfer operator is one of the fundamental objects which appears naturally in tensor network computations. It is constructed by blocking the double tensors $\mathbb{E}$ in one direction.

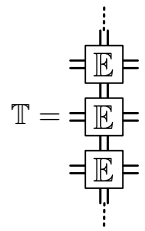

(3.26)

We say that $|l)$ and $|r)$ are the left and right fixed points of transfer operator, if $(l|\,\mathbb{T} = (l|$ and $\mathbb{T}\,|r) = |r)$. The transfer operator is an infinite object for systems in the thermodynamic limit. Now, to have a useful definition of fixed points, we assume that an MPS can represent the fixed points with finite bond dimension. Let A be an MPS tensor and the action of the double tensor $\mathbb{E}$ on A generates tensor A'.

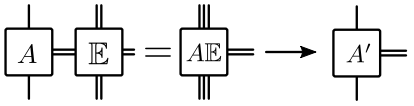

(3.27)

The arrow highlights the fact that the tensor A' is an approximation of the left tensor with bond dimension χ. We call $|l[A])$ the left fixed point of $\mathbb{T}$ if the overlap per site between $|l[A])$ and $|l[A'])$ is equal to 1 up to a certain tolerance. Similarly, it is possible to define right fixed points with an MPS structure.

In the following, we will describe a method to numerically compute the fixed points of the transfer operator which is enabled by the extension of *power iteration method* for eigenvalue problems in the thermodynamic limit and it is usually referred to as infinite matrix product state (iMPS) algorithm. First, we describe the method to compute left and right fixed points. Second, a method to compute the diagonal fixed points has been described.

Left/Right fixed points

Power iteration algorithm is the most straightforward method to compute the largest eigenvalues of matrices. The idea is to start with a random initial vector and iteratively multiply it by the matrix while normalizing the resulting vector on each iteration. The intuition is that the procedure would converge to a vector after a finite number of iterations and the only contribution in the resulting vector would be from the largest eigenvector.

iMPS algorithm works in the same spirit. It starts execution with a randomly initialized MPS approximation of a fixed point. An MPO (i.e., the transfer operator) is iteratively applied to the MPS. In each iteration, after acting with MPO, the new MPS is transformed into the canonical form. Given the canonical description, the bond dimension of MPS is truncated as we described earlier by restricting the number of Schmidt coefficients across any bipartition to a fixed bond dimension. The execution is halted when the overlap per site between two successive MPSs is equal to 1 up to a certain tolerance. These steps have been formalized in Algo. 3. It should be noted here that the convergence occurs in the fixed point approximations from two consecutive iterations and not necessarily in their local MPS tensors due to the gauge freedom [51].

Algorithm 3: Find the fixed of the transfer operator from the left.

function iMPSLeft;
Input : Double tensor $\mathbb{E}$, bond dimension χ, tolerance tol.
$A = rand$; `// Initialize` A `randomly to a` $\chi \times d \times \chi$ `tensor.`
$A_{prev} = 0$, $err = 1$;
while $err > tol$ **do**
  $A \leftarrow applyDoubleTensor(\mathbb{E}, A)$; `// Apply the double tensor` $\mathbb{E}$ `to` A `as shown in eq.`(3.27)`.`
  $nA = 1/norm(A)$
  $A = A \times nA$; `// Normalize A.`
  $A \leftarrow truncate(A, \chi)$; `// Find the approximation of` A `with bond dimension` χ`.`
  $err = |1 - overlapPerSite(A, A_{prev})|$
  `// Find the overlap per site between the last two iterations.`
  $A_{prev} = A$
end
Output: A

In each iteration of iMPS algorithm, we apply the double tensor $\mathbb{E}$ with dimensions $(D^2 \times D^2 \times D^2 \times D^2)$ to the tensor A with dimensions $(\chi \times D^2 \times \chi)$. The indices of resulting MPS tensor has dimensions $(\chi D^2 \times D^2 \times \chi D^2)$. Finding out the canonical representation of the resulting MPS is computationally the most expensive step both in terms of space (memory) and time requirements. A crucial improvement can be made in this step by exploiting the ket and bra structure of double tensors $\mathbb{E}$. The idea is to split each iteration into two steps. In the first step, we apply only the bra layer $\mathbb{E}$ to the MPS tensor. Then we compute the canonical form and approximate the resulting tensor. In the second step, the bra layer of $\mathbb{E}$ is applied to the MPS tensor.

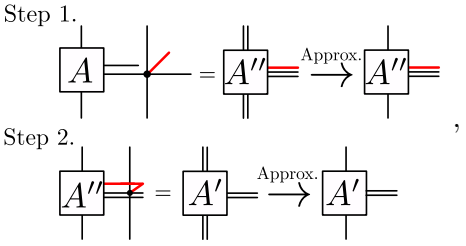

(3.28)

where the red lines represent the physical indices of 2D wavefunction.

Diagonal fixed points

Given a lattice structure or the expectation value of observables one intends to compute, sometimes it is natural to find the fixed points of the system from the diagonal direction.

Transfer operator $\mathbb{T}_{diag}$ has a 2-layer structure,

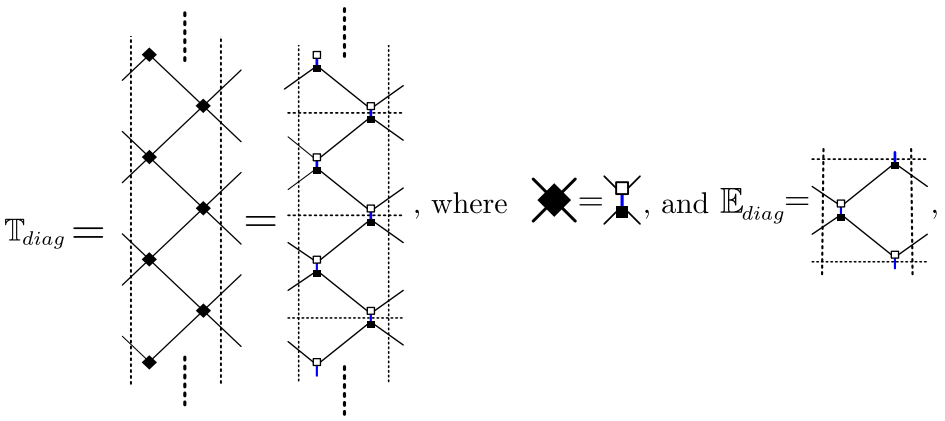

(3.29)

and for illustrative convenience, we have drawn the bra and ket indices as a single index. It is instinctive to consider MPSs with the 2-site unit cell as an ansatz for the fixed points of diagonal transfer operator $\mathbb{T}_{diag}$.

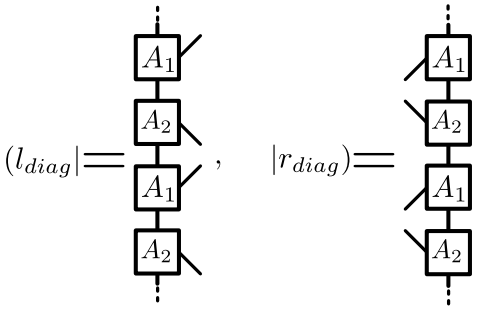

(3.30)

Similar to the case of vertical transfer operator, we randomly initialize the 2-site MPS and repeatedly apply $\mathbb{E}_{diag}$ to the MPS tensor. Each application of $\mathbb{E}_{diag}$ can be split into two steps by exploiting the 2-layer structure. The method to approximate multi-site MPSs has already been described in Sec. 3.2.4.

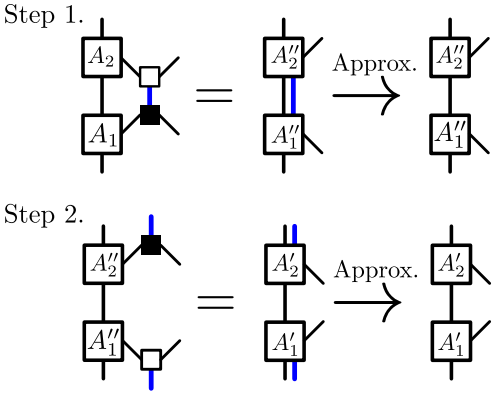

(3.31)

Furthermore, the above routine can be made more efficient by incorporating the steps described in (3.28).

3.2.6 Expectation value of observables

Now we describe methods for computing the expectation value of observables for the systems in the thermodynamic limit.

Local order parameter

Assuming that there is a routine to find the fixed points of the transfer operator, the computation of the expectation value of local observables can be reduced to the problem of contracting a finite tensor network. Here, we illustrate the steps involved in computing the expectation value of a product operator which acts diagonally on the physical indices of two lattice sites (see Fig. 3.1a). The same approach can be adapted for computing the expectation value of other local quantities. It is important to note here that we use this example to highlight the computational overhead incurred because the local operator acts diagonally and we use the left/right fixed points. The massive increase in memory and time requirements can be avoided by using the fixed points of diagonal transfer operator to compute the expectation value of 'diagonal' operators.

A dimensional reduction from the 2D to the 1D object is achieved by sandwiching the left and right fixed points of the transfer operator (see Fig. 3.1(a,b)). The 1D object is constructed from the chain of channel operators. In the middle of this infinite 1D object, we have double tensors $\mathbb{E}_{\hat{O}}$ which specify the action of local observables. The next step involves the computation of the largest eigenvectors of the channel operator from the top and bottom using an exact diagonalization method.

$\mathbb{F}\,|\rho_t) =$ 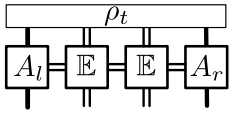

$= \lambda_0$ 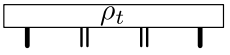

(3.32)

A similar relation also holds between $\mathbb{F}$ and ρ_b. Due to the diagonal action of operators relative to the left and right fixed points, ρ_b and ρ_t lives in $\mathbb{C}^{\chi^2 D^4}$ which is significantly large compared to $\mathbb{C}^{\chi^2 D^2}$ in the case operators with parallel action, as described in the next subsection. Now given the largest eigenvectors of the channel operator from the top and the bottom, the expectation value can be computed as,

$$\langle \hat{O}_1 \hat{O}_2 \rangle = \frac{(\rho_b|\,\mathbb{F}_{\hat{O}_1}\mathbb{F}_{\hat{O}_2}\,|\rho_t)}{\lambda_0^2(\rho_b|\rho_t)}, \tag{3.33}$$

which is shown pictorially in Fig. 3.1c.

The method has been applied to compute the expectation value of Heisenberg interactions, $S_i.S_j$, for the resonating valence bond (RVB) state on the kagome lattice (see

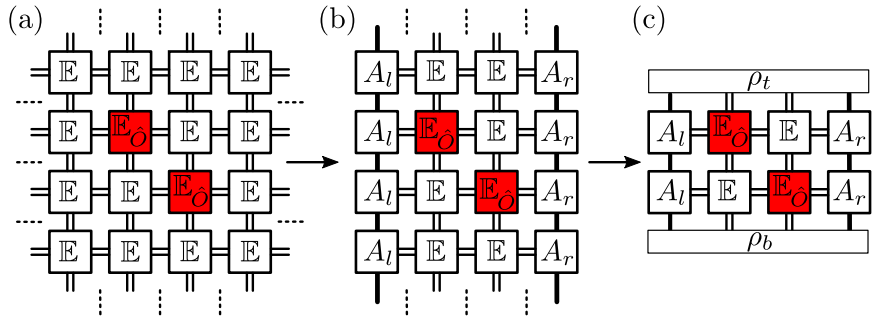

FIGURE 3.1: (a) The graphical representation of the quantity, $\langle \hat{O}_1 \hat{O}_2 \rangle$, in the thermodynamic limit. The double tensor $\mathbb{E}_{\hat{O}}$ is obtained by acting with $\hat{O}$ on the physical indices of on-site tensor A followed by a contraction with the conjugate of A. (b) Except in the middle of infinity, each slice is defined by the so-called channel operator $\mathbb{F}$. (c) The finite tensor network which represents the expectation value of the observable.

Fig. 3.2(a,b)). The tensor network description of the RVB wavefunction is given in Sec. 2.4 for the 3-site unit cell. The RVB wavefunction does not break any rotation or translation symmetry. However, the expectation values of the interactions on different edges suffer the finite χ effect, where χ is the bond dimension used for approximating the fixed points of the transfer operator. There is a finite splitting in the value of different interactions which vanishes with increasing bond dimension (see Fig. 3.2c).

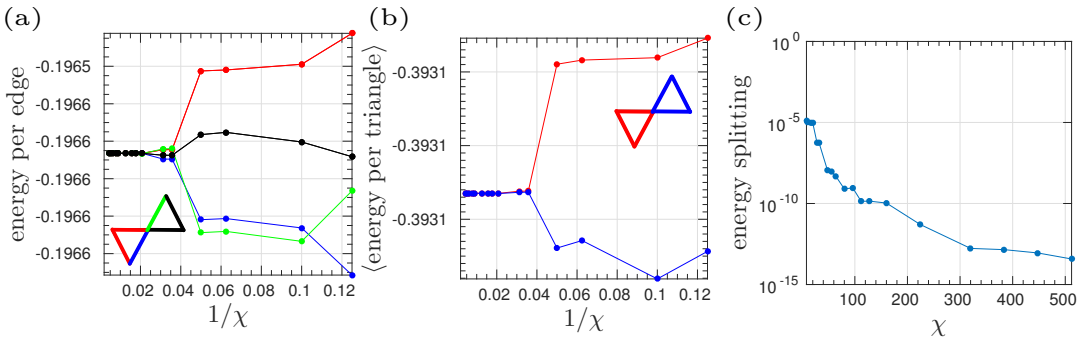

FIGURE 3.2: (a) The expectation value of the Heisenberg interaction $S_i.S_j$ for the RVB wavefunction on the 6-edges of the unit cell. The legend of the curves is defined by the edges of up/down pointing triangles of the kagome. The color of the edge associates it with a curve in the plot. (b) Mean energy per site for the left (red) and right (blue) pointing triangles. (c) Splitting in the expectation value of different interactions which have been quantified by the standard deviation of 6 energies in (a). At $\chi = 512$, the splitting is small enough to give a high precision estimate of energy per site, which is -0.3931232344861(1).

Two point correlation function

Now we describe an approach to compute two point correlation functions using a few modifications to the steps involved in the computation of local order parameters. Correlation functions provide a way to quantify correlations (i.e., the coupling or interdependence) in the properties of the observables acting on different parts of the system. Here, we have a two body operator acting on the sites separated by the distance r on an infinite system, and the goal is to find the expectation value. We assume that the operator acts either in the horizontal, vertical or diagonal direction. Furthermore, it is possible to compute two point correlation function in any direction using the approach of corner transfer matrices [41].

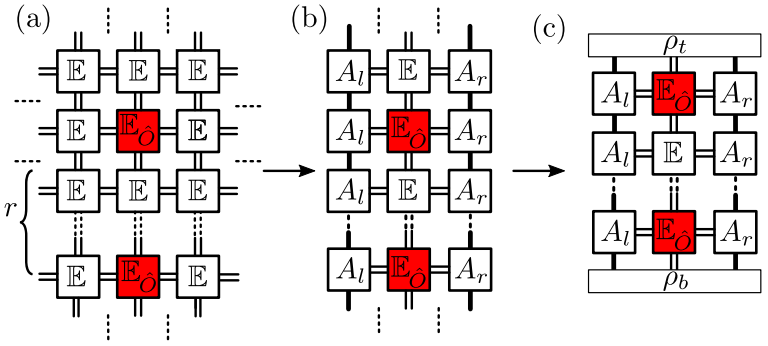

FIGURE 3.3: (a) Graphical representation of the expectation value of two point correlation function $\langle \hat{O}_i \hat{O}_{i+r} \rangle$ acting on the sites i and $i+r$. (b) Dimensional reduction from a 2D to a 1D infinite object. (c) The finite tensor network to compute two point correlations.

The graphical representation of the steps is given in Fig. 3.3. As described earlier in the case of computing the expectation value of local order parameters with appropriately chosen fixed points we get channel operators with better scaling properties.

$$\mathbb{F}\,|\rho_t) = \quad = \lambda_0 \quad \tag{3.34}$$

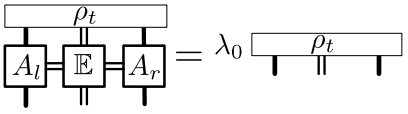

Given the largest eigenvectors of the channel operator, the expectation value can be computed as,

$$\langle \hat{O}_i \hat{O}_{i+r} \rangle = \frac{(\rho_b|\,\mathbb{F}_{\hat{O}_i} \hat{\mathbb{F}}^{(r-1)} \mathbb{F}_{\hat{O}_{i+r}}\,|\rho_t)}{\lambda_0^2 (\rho_b|\rho_t)}\ , \text{ where } \hat{\mathbb{F}} = \mathbb{F}/\lambda_0. \tag{3.35}$$

3.2.7 Correlation length

One of the most remarkable properties of the gapped quantum many-body systems is the exponential decay of correlations with distance, i.e., the expectation value of two

point correlation function acting on sites separated by distance r in a gapped quantum system decays as $K(r)e^{-r/\xi}$. Where the exact form of $K(r)$ depends on the operators for which we measure the correlations. Since ξ is a natural length scale to characterize the decay, it is usually termed as the correlation length.

Tensor network states enable an approach to express these correlations as a sum of constant and exponentially decaying contributions [52]. Let $\mathbb{F}^{(r-1)} = \sum_{k=0}^{\chi^2 D^2-1} \lambda_k^{(r-1)} |\rho_t^k)(\rho_b^k|$ be representation of $\mathbb{F}^{(r-1)}$ obtained by using the eigenvalue decomposition, where $\mathbb{F}$ is the channel operator (3.34). Then, by substituting it in (3.35), we get

$$\begin{aligned}\langle \hat{O}_i \hat{O}_{i+r} \rangle &= \frac{(\rho_b| \mathbb{F}_{O_i} |\rho_t)(\rho_b| \mathbb{F}_{O_{i+r}} |\rho_t)}{\lambda_0^2 (\rho_b|\rho_t)} + \sum_{k=1}^{\chi^2 D^2-1} \left(\frac{\lambda_k}{\lambda_0}\right)^{r-1} \frac{(\rho_b| \mathbb{F}_{O_i} |\rho_t^k)(\rho_b^k| \mathbb{F}_{O_{i+r}} |\rho_t)}{\lambda_0^2 (\rho_b|\rho_t)} \\ &\approx \langle \hat{O}_i \rangle \langle \hat{O}_{i+r} \rangle + \left(\frac{\lambda_1}{\lambda_0}\right)^{r-1} \frac{(\rho_b| \mathbb{F}_{O_i} |\rho_t^1)(\rho_b^1| \mathbb{F}_{O_{i+r}} |\rho_t)}{\lambda_0^2 (\rho_b|\rho_t)}.\end{aligned} \tag{3.36}$$

Now, the connected correlation function which quantifies correlations can be expressed as

$$\begin{aligned}\hat{C}(i, i+r) &= \langle \hat{O}_i \hat{O}_{i+r} \rangle - \langle \hat{O}_i \rangle \langle \hat{O}_{i+r} \rangle \\ &\approx \left(\frac{\lambda_1}{\lambda_0}\right)^r \frac{(\rho_b| \mathbb{F}_{O_i} |\rho_t^1)(\rho_b^1| \mathbb{F}_{O_{i+r}} |\rho_t)}{\lambda_0 \lambda_1 (\rho_b|\rho_t)} = K \left(\frac{\lambda_1}{\lambda_0}\right)^r,\end{aligned} \tag{3.37}$$

If the state has the translation symmetry, then the prefactor K does not depend on r. By equating the exponentially decaying term with $e^{-r/\xi}$, we get $\xi = -1/\ln(\lambda_1/\lambda_0)$.

3.2.8 Spectrum of the transfer operator

Eigenvalues of the transfer operator essentially contain all the information about the low energy properties of the system [44, 53]. Given a system on an infinite cylinder, the computation of the eigenvalues of the transfer operator can be done by exact diagonalization using an iterative eigenvalue solver routine. However, for the infinite systems, information about the excited states of the system can be extracted by using the 'excitation ansatz.' This approach was introduced in [54] for MPSs, and it was later extended to infinite systems by Haegeman et al. in [55]. An extensive review of these methods can be found in [50]. Here, we will briefly describe the method to later use it for computing the eigenvalues of the transfer matrix. We will assume that transfer operator is Hermitian which implies that the left and right fixed points are related by the conjugate.

Given a system with translation invariant transfer operator (e.g. a finite chain with periodic boundary conditions or an infinitely long system), the spectrum can be divided

into different sectors. Each of these sectors can be labeled by the irreducible representation (irrep) of translation symmetry $\mathbb{Z}_N$. Let $k \in \{0, 1, 2, ..N-1\}$ represents the irrep of $\mathbb{Z}_N$, then a projector onto the sector where the eigenvalues of transfer operator $\mathbb{T}$ have a label k is $P_k = \sum_{n=0}^{N-1} \left(e^{2\pi ik/N} T\right)^n$, T is the generator of $\mathbb{Z}_N$. The action of T on the system shifts lattice sites by a unit distance. As $N \to \infty$ in the thermodynamic limit, it is more convenient to write P_k as,

$$P_k = \sum_{n=-\infty}^{\infty} \left(e^{ik} T\right)^n, \tag{3.38}$$

with $k \in [-\pi, \pi)$.

Let A be an MPS tensor which characterizes the fixed point $|\psi(A)\rangle$ of transfer operator (Sec. 3.2.5). We also assume that the transfer operator has been rescaled such that its largest eigenvalue is equal to 1. It is intuitive to consider the states of the form

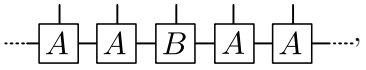

(3.39)

where the tensor B lies in the middle of infinity, and B is computed by a variational method in order to construct the excited states of the transfer operator. Furthermore, this approach can be extended to build an ansatz for the excited states of the transfer operator within each k sector,

$$|\phi_k(B; A)\rangle = P_k \left(\cdots \boxed{A}\boxed{B}\boxed{A} \cdots \right). \tag{3.40}$$

As it has been observed by Haegeman et al. in [50], there is an *additional* gauge freedom in the representation of the variational tensor B. Any two B's which are related to each other by

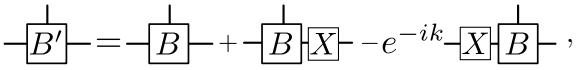

(3.41)

generate the same quantum state (3.40). Now for every k, we want to find B's such that,

$$\begin{aligned} \langle \phi_k(B; A) | \phi_{k'}(B'; A) \rangle = 0 \quad &\text{if} \;\; k \neq k' \;\text{or}\; B \overset{(3.41)}{\neq} B' \\ \langle \psi(A) | \phi_k(B; A) \rangle = 0 \quad &\forall \; k, \end{aligned} \tag{3.42}$$

i.e., B is not related to B' by (3.40) and every excited state should be orthogonal to the fixed point $|\psi(A)\rangle$ of the transfer operator.

A remarkable insight made in [50] is to exploit the freedom in the representation of B in order to construct a variational manifold where the constraints on B are implicitly

satisfied. Consider $D \times dD$ matrix L

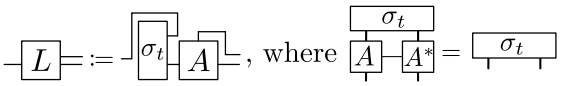

(3.43)

and let V_L be an orthogonal projector onto the null space of L i.e.

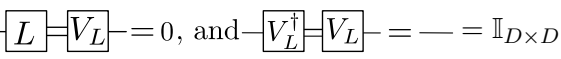

(3.44)

V_L is a $Dd \times (D-1)d$ matrix. Using these definitions, one can define a representation of B on a restricted manifold which satisfy the constraints on B in (3.42).

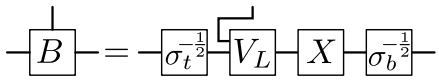

(3.45)

where X is an $(D-1)d \times D$ matrix which contains the variational parameters. Furthermore, for any X the state $|\phi_k(B;A)\rangle$ is orthogonal to $|\psi(A)\rangle$. Another nice feature of the representation in (3.42) is that the norm of $|\phi_k(B;A)\rangle$ is equal to 1 if X is normalized since $\langle\phi_k(B;A)|\phi_k(B;A)\rangle = \mathrm{tr}(X^\dagger X)$.

Given that we have a representation of B in terms X which also satisfy all the constraints, the problem can now be formalized as

$$\lambda(k) = \max_{X,\mathrm{tr}(X^\dagger X)=1} \langle\phi_k(X;A)|\mathbb{T}|\phi_k(X;A)\rangle \ , \tag{3.46}$$

which can be reduced to the problem of diagonalizing an effective transfer matrix $\mathbb{T}_{eff}$.

$$\mathbb{T}_{eff}(k)X_i(k) = \lambda_i(k)X_i(k) \ , \tag{3.47}$$

where each eigenvector of $\mathbb{T}_{eff}$ lives in $\mathbb{C}^{\chi^2 D^2}$. $\mathbb{T}_{eff}$ can be computed as a sum of three terms

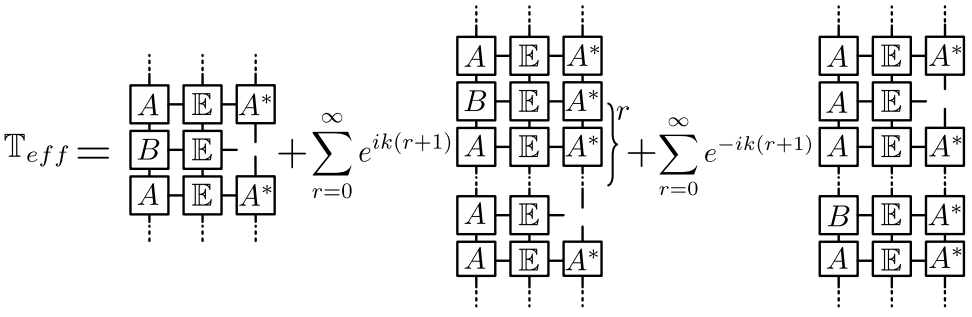

(3.48)

where the second and third term involve infinite geometric sums. Let

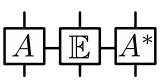

(3.49)

then for $k \neq 0$, the geometric sums can be expressed as

$$\sum_{r=0}^{\infty} \left(e^{ik}\mathbb{F}\right)^r = \left(\mathbb{I} - e^{ik}\left(\mathbb{F} - |\rho_t)(\rho_b|\right)\right)^{-1} + |\rho_t)(\rho_b| \ , \tag{3.50}$$

where the operator $\mathbb{F}$ is assumed to be rescaled such that its largest eigenvalue equal to 1. The substitution of last term $|\rho_t)(\rho_b|$ in the (3.48) gives zero because of the gauge which has been chosen to represent B. So the sum can be defined as

$$\mathbb{H}_k := \left(\mathbb{I} - e^{ik}\left(\mathbb{F} - |\rho_t)(\rho_b|\right)\right)^{-1} \tag{3.51}$$

In the case of $k = 0$, the infinite sum also contains divergent prefactor with $|\rho_t)(\rho_b|$ which again can be discarded due to the chosen gauge. So the definition in (3.51) holds for every k. Using these definitions the sum can be expressed as

$\mathbb{T}_{eff} =$ 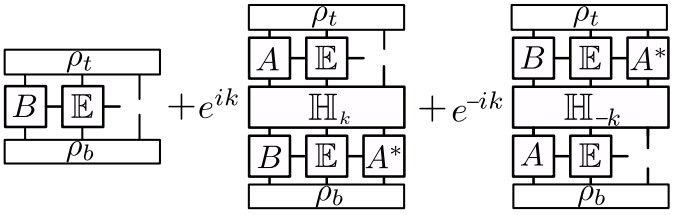

(3.52)

Although it is possible to compute the matrix $\mathbb{H}_k$ explicitly if the bond dimension is very small, for a problem with large bond dimensions, the computation of inverse or even the matrix $\left(\mathbb{I} - e^{ik}\left(\mathbb{F} - |\rho_t)(\rho_b|\right)\right)$ is not feasible. An efficient approach is to reduce the problem of finding a matrix to the problem of multiplying a vector with the matrix (which is easier). Furthermore, the problem of finding an inverse can be reduced to the problem of finding a solution for a linear system of equations and the system of linear equations can be solved very efficiently by an iterative solver, for example by GMRES method, or by a variant of Conjugate Gradient method.

Chapter 4

Anyon condensation and topological phase transitions

The remarkable properties of topologically ordered systems which include topologically degenerate ground states and existence of anyonic excitations remain intact against the local effects of the environment [56–60]. It has been suggested that the stability of these characteristics can be employed for building a reliable quantum computer [7]. The absence of the two related notions of *local order parameter* and *symmetry breaking* in topologically ordered systems while on the one hand makes the problem of studying topological phase transitions challenging, it also opens up the possibility of the phase diagrams with richer properties.

One approach to generalize the idea of order parameters for topologically ordered systems is by using the framework of *anyon condensation* and *anyon confinement* [12, 61, 62]. The idea is to use the mutual distinguishability between different species of anyon and their existence as a fundamental measure to characterize the topological order of the quantum phase. We can start with a *fundamental* model having an underlying structure (i.e., the virtual symmetry of local tensors in the tensor network framework), and the set of anyons which are allowed to exist characterizes the topological order of the *fundamental* model. By doing operations (which keep the topological structure intact) on the quantum states, it is possible to undergo phase transitions. Furthermore, each quantum phase resulting from the phase transition has a unique set of anyons which are allowed to exist in it. By studying the set of anyons and the condensation and confinement pattern of anyons in a given topological phase, we can map the phase diagram of the topological phases of quantum matter.

The framework of tensor networks provides a natural setting for analyzing the phenomena of anyon condensation and confinement. Although the topological order is associated

with the global properties of the system (e.g., topological degeneracy and long-range entanglement), what has been observed quite remarkably is that the emergence of these global properties is a manifestation of a certain structure in the local description [9–11]. The kind of topological order is dictated by the virtual symmetries of local tensors. Moreover, the condensation and confinement of anyons in a given topological phase is ultimately associated with the pattern of symmetry breaking in the fixed points of the *transfer operator*. As a result, it is possible to use anyon condensation, and confinement as order parameters for topologically ordered systems and this approach is capable enough to capture the universal features of quantum phase transitions between topologically trivial and non-trivial phases.

This chapter has been organized as follows. In Sec. 4.1 we give an introduction to the basic ideas and tools which will be crucial for the later studies. We also briefly review the conventional 'flux line' (or loop pattern) interpretation of $D(\mathbb{Z}_N)$ quantum doubles, the toric code, and the double semion model. In Sec. 4.2, we describe distinct topological phases in terms of $\mathbb{Z}_4$-invariant tensors. In Sec. 4.3, we describe phase transitions between topologically trivial and non-trivial phases of $\mathbb{Z}_4$-invariant tensors. In Sec. 4.4 we describe methods which are available from the framework of tensor networks for studying topological phase transitions. In Sec. 4.5, we study the phase diagram of $\mathbb{Z}_4$-invariant tensors. We summarize our results in Sec. 4.6.

4.1 Preliminary concepts

This section contains a primary introduction to the basic notions which will be important for the later discussions.

4.1.1 Objects from the tensor network toolbox

Here we present the graphical notation for different objects in the framework of tensor networks. These objects have already been discussed in the previous chapter, and the intention here is to keep the content of the current chapter self-contained. The fundamental object which encodes the entanglement structure of the many-body wavefunction $|\psi\rangle$ is the on-site tensor A (Fig. 4.1a). The virtual and physical indices of the on-site tensor A are denoted by v_i and p respectively. By tracing out the virtual indices of the local tensor, we get the many-body wavefunction $|\psi[A]\rangle$ (Fig. 4.1b) which is a global object. Another object of interest for our purposes is the *double* tensor $\mathbb{E}$ which results from contracting the physical indices of on-site tensor A with its conjugate. The double

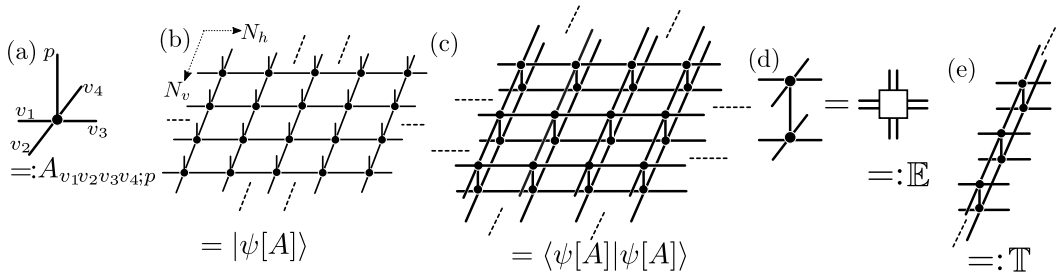

FIGURE 4.1: (a) The graphical notation of an on-site tensor A. (b) Tensor network representation of a many body wavefunction. (c) Tensor network representation of the wavefunction norm. (d) On-site transfer operator (or the double tensor) $\mathbb{E}$ is obtained by contracting the physical indices of A and its conjugate. (e) Transfer operator $\mathbb{T}$ obtained by blocking $\mathbb{E}$ tensors in one direction.

tensor can be viewed as a map between virtual spaces associated with ket and bra layer (Fig. 4.1d).

Now to compute the expectation value of local observables and the norm of quantum states, transfer operator $\mathbb{T}$ plays a central role. Transfer operator $\mathbb{T}$ can be obtained by gluing double tensors in the horizontal or vertical direction. Although the transfer operator can have a periodic structure, for our purposes in this chapter, we assume it to be an infinite object that describes the system in the thermodynamic limit unless mentioned otherwise.

4.1.2 Topological or virtual symmetries

The 'virtual symmetries' of local tensors dictate the kind of the topological order in the underlying quantum state [9–11]. An on-site tensor is matrix product operator (MPO)-invariant if one can pull through the action of the MPO on the virtual legs of tensor A.

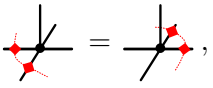

(4.1)

where the solid red squares denote local tensors of the MPO. In (4.1) we show one of the possible instances of the *pulling through* property for (MPO)-invariant local tensors. For our purposes in this chapter, we will focus on G-invariant tensors where the MPO is a product operator with the point group action. Furthermore, we will restrict ourselves to the cyclic groups of order N. The local action of the group element on a virtual index induces a permutation on the internal (entanglement) degrees of freedom of that index and for G-invariant tensors, the collective action of the group elements on the virtual indices leaves the tensor unchanged.

If we consider a $\mathbb{Z}_N$-invariant tensor A as a map from virtual to the physical space and if the map is injective on $\mathbb{Z}_N$ invariant subspace than A is called $\mathbb{Z}_N$-injective. Besides, the

$\mathbb{Z}_N$-injective tensor is called $\mathbb{Z}_N$-isometric if the associated map also acts as an isometry. The canonical approach to construct $\mathbb{Z}_N$-isometric tensor involves taking a symmetric sum over the elements of the $\mathbb{Z}_N$.

$$A_{D(\mathbb{Z}_N)} = \sum_{g=0}^{N-1} X^g \otimes X^g \otimes X^{g\dagger} \otimes X^{g\dagger} \ , \tag{4.2}$$

where the symmetrized sum enforces the constraint defined by (4.1), $X^g := \sum_{i=0}^{N-1} |i+g\rangle\langle i|$ and X is the generator of $\mathbb{Z}_N$ with regular representation. The construction works in any unitary representation, but for our purposes, we will assume X to be a regular representation of $\mathbb{Z}_N$ unless mentioned otherwise. The subscript $D(\mathbb{Z}_N)$ of the on-site tensor A on the LHS highlights the fact that $\mathbb{Z}_N$-isometric tensors provide a natural description for the ground states of the $D(\mathbb{Z}_N)$ quantum double.

It is possible because of the G-invariance property of local tensors to construct certain string operators such that the actions of these operators on the quantum state cannot be detected locally as these string operators can be pulled through each physical index. Furthermore, as we will see in the following subsection, these semi-infinite string operators can be used to create the anyonic excitations of the model in distinct topological sectors. And a nice property of the tensor network construction of an anyonic excitation is that the topological sector of the excitation remains well-defined even in the presence of a physical deformation. The stability of the G-invariant property against deformations on the physical legs of the local tensors is a crucial property for studying topological phase transitions as it will become clear later in the chapter.

4.1.3 Tensor network construction of anyonic excitations

The different anyonic particles of a topological model can be labeled by the conjugacy classes and the irreducible representations (irreps) of the symmetry group [7]. In the case of $\mathbb{Z}_N$, the conjugacy classes are just the group elements. Anyons labeled with a non-trivial conjugacy class but with a trivial irrep represent the presence of a flux line in the anyonic vacuum and two violations of Gauss law at the endpoints of flux line which corresponds to a pair of anyonic excitations. In the framework of tensor networks, flux lines can be created by acting with the string operator $X^g X^g ... X^g$, where g is an element of $\mathbb{Z}_N$, on the virtual indices of the tensor network [9]. If the tensor network description of on-site tensors is given in terms of $\mathbb{Z}_N$-invariant tensors, than (4.1) ensures that the presence of flux line in the quantum vacuum cannot be detected anywhere except at the endpoints. Anyons which are labeled with a trivial conjugacy class but with a non-trivial irrep represent charged anyons, and they can be created by acting with $Z_\alpha := \sum_{i=0}^{N-1} \alpha^i |i\rangle\langle i|$, where α denotes an irrep of $\mathbb{Z}_N$, on the virtual edge.

We can also create a bound state of flux and charged anyons by composing the string and irrep action.

Given a tensor network description of the quantum vacuum on an infinite plane, we can extend the ends of X^g string to be infinitely far apart and treat the open ends as individual anyons with the string attached. The anyonic excitation can be represented graphically as,

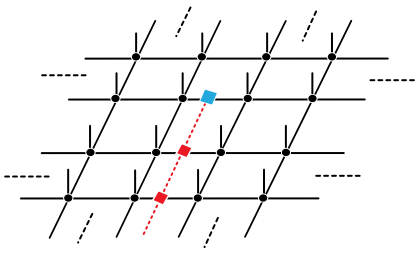

$$= |g, \alpha\rangle, \tag{4.3}$$

where the red squares on the red string denote, X^g and the blue square represents Z_α. We will write anyonic vacuum as $|0, 1\rangle$, where $g = 0$ represents the identity element of $\mathbb{Z}_N$ and $\alpha = 1$ denotes the trivial irrep.

4.1.4 Condensation and confinement of anyons

In the preceding subsection, we have described the tensor network construction of anyonic excitations in terms of string operators which act solely on the entanglement degrees of the tensor network. Now the deformations on local tensors which keep the virtual symmetries intact (i.e., the action on the physical indices of on-site tensors) can induce quantum phase transitions. Since the excitation operators act on virtual indices, their behavior remains well-defined irrespective of the action of deformation on the physical indices. The collective action of these excitation operators can be used to label not only the topological phase of $D(\mathbb{Z}_N)$ quantum double but also the topological phases which can be induced from it. Condensation and confinement of anyons provide an approach to summarize the behavior of anyonic excitations [12]. Here we give a review of the two notions, a detailed account of anyon condensation and confinement in the context of tensor networks is given in [63].

Condensation of anyons refers to the fact that in certain topological phases resulting from quantum phase transitions, it is not possible to distinguish the topological sectors of certain species of anyons and the quantum vacuum, i.e., the actions which lead to the creation of anyons act trivially on the vacuum state in the anyon condensed phase. As the system is tuned from one topological phase to another, operators corresponding to certain anyons act trivially on the vacuum (ground state). More precisely, we say an

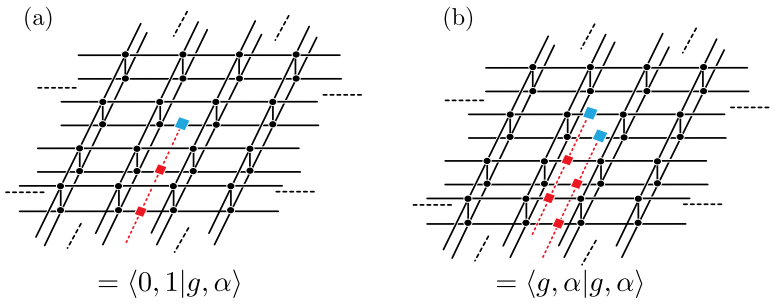

FIGURE 4.2: Graphical representation of wavefunctions overlaps in the thermodynamic limit. (a) Overlap quantify the condensation of anyon $|g,\alpha\rangle$ (bra layer) to the vacuum $\langle 0,1|$ (ket layer). (b) Overlap quantify the confinement fraction of anyon $|g,\alpha\rangle$.

anyon $|g,\alpha\rangle$ has been condensed to the vacuum $|0,1\rangle$ if

$$\langle 0,1|g,\alpha\rangle \neq 0. \tag{4.4}$$

On the other hand, anyon confinement refers to the existence of certain anyonic species in a given topological phase where it is not possible to separate some pair of anyons attached by the string and treat them individually, i.e., these anyons are confined. An anyon is confined if

$$\langle g,\alpha|g,\alpha\rangle = 0. \tag{4.5}$$

The graphical representations of the two overlaps $\langle 0,1|g,\alpha\rangle$ and $\langle g,\alpha|g,\alpha\rangle$ which are relevant for computing the condensation and confinement of anyon $|g,\alpha\rangle$ are given in Fig. 4.2.

One of the most crucial aspects of critical systems is that they exhibit universality. The qualitative behavior of the macroscopic quantities of different critical systems shares common features in the vicinity of phase transitions. This commonality in the behavior points to a more deep structure which is independent of microscopic details, and the condensation and confinement of anyons is a way to capture this structure for the phase transitions involving topological phases. Each topological phase (trivial/non-trivial) can be identified with a distinct pattern of anyon condensation and confinement, and we can use them as a probe to extract the universal features of topological phase transitions. Instead of treating the condensation and confinement as an absolute property (all or nothing) without being partial, we can quantify them by their corresponding fractions. Remarkably, the behavior of certain fractions along the phase transition is analogous to that of the 'local order parameter', and they can be used as a robust tool which is more capable of characterizing different phase transitions.

The main quantity of interest for our purposes is the overlap $\langle g',\alpha'|g,\alpha\rangle$ of two wavefunctions, where the condensation and confinement fractions can be given by overlaps of the form $\langle 0,1|g,\alpha\rangle$ and $\langle g,\alpha|g,\alpha\rangle$ respectively. In general, the overlap $\langle g',\alpha'|g,\alpha\rangle$

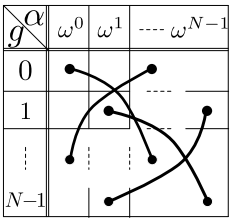

FIGURE 4.3: The anyon table of a topological phase. $\omega = e^{2\pi i/N}$ and the black dot in entry $(1, \omega^1)$ indicates that $\langle 1, \omega | 1, \omega \rangle = 1$. The absence of a black dot in entry $(1, \omega^0)$ shows confinement (e.g., $\langle 1, 1 | 1, 1 \rangle = 0$). The solid line between the entries $(0, \omega^0)$ and $(2, \omega^2)$ shows the condensation of anyon $|2, \omega^2\rangle$ to the vacuum $|0, 1\rangle$.

quantifies how much the quantum state with anyon $|g, \alpha\rangle$ is indistinguishable from the anyon $|g', \alpha'\rangle$ and the value of 1 characterizes complete indistinguishably (assuming that the wavefunctions are normalized).

As we have mentioned earlier that each anyonic excitation can be labeled by the conjugacy class g and the irrep α of the symmetry group. Furthermore, since the object of interest for our purposes is the overlap $\langle g', \alpha' | g, \alpha \rangle$, the idea is to use an *anyon table* to qualitatively express the condensation and confinement pattern of anyons in a given topological phase. The *anyon table* is a 2D grid which has an entry for each pair of the conjugacy class g and the irrep α (Fig. 4.3). We can show the confinement of an anyon (g, α) in the anyon table by keeping that entry empty. More precisely, the presence (absence) of the black dot ($\bullet$) in an entry indicates the deconfinement (confinement) of the anyon which is associated with that entry. Similarly, we can indicate the condensation of anyons by drawing solid lines between entries. The presence (absence) of a solid line between the entries (g, α) and (g', α') shows that overlap $\langle g', \alpha' | g, \alpha \rangle$ is nonzero (zero). Moreover, the number (#black dots + 2#dashed lines) is same for every anyon table in the framework irrespective of the topological phase.

4.1.5 Connection between the phases at the boundary and the bulk

The topological structure of on-site tensors is also carried by the transfer operator. If the on-site tensor A is $\mathbb{Z}_N$-invariant, then the transfer operator comprised of the chain of double tensors is invariant under the action of the group $\mathbb{Z}_N \times \mathbb{Z}_N$ and it satisfies the following commutation relations [44].

$$\left[\mathbb{T}, (X \otimes \mathbb{I})^{\otimes L}\right] = \left[\mathbb{T}, (\mathbb{I} \otimes X)^{\otimes L}\right] = 0. \tag{4.6}$$

Where $L \to \infty$ as $\mathbb{T}$ is an infinite object and X is the generator of $\mathbb{Z}_N$.

The behavior of transfer operators is of fundamental importance to understand the behavior of topological phases and phase transitions [13, 44]. The $\mathbb{Z}_N \times \mathbb{Z}_N$ symmetry

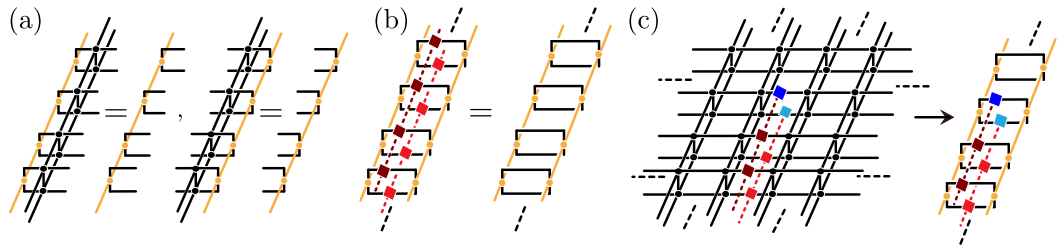

FIGURE 4.4: (a) Matrix product state (MPS) representation for the left and right fixed points of the transfer operator. The yellow lines indicate the virtual indices of local MPS tensors. (b) Symmetry action given by the Kronecker product of light and dark red string gets absorbed by the fixed points. (c) Mapping of an overlap of anyonic wavefunctions to the expectation value of string order parameter.

of transfer operator is preserved by the deformation on the physical indices of on-site tensors. Let $(l|$ and $|r)$ be the left and right fixed points of the transfer operator such that $\mathbb{T}\,|r) = \lambda_0\,|r)$ and $(l|\,\mathbb{T} = \lambda_0\,(l|$ (Fig. 4.4a). Then the fixed points of the transfer operator can break or reduce the symmetry of transfer operator (Fig. 4.4b) . It is important to note that in Fig. 4.4a, due to the gauge freedom, equality only holds for the fixed points and not for the local MPS tensors.

It has been observed in [63] that the different instances of symmetry breaking in the fixed points of the transfer operator are directly related to the condensation and confinement pattern of anyons in the topological bulk. The connection between the symmetry breaking in the fixed points of the transfer operator and the condensation and confinement patterns of anyons can be used to label different topological phases realized by $|\psi[A]\rangle$. The 1D boundary phase associated with the fixed points of the transfer operator is characterized by the symmetries of the fixed points. The condensation and confinement pattern of anyon is related to the expectation value of string order parameter in the boundary phase,

$$\langle g', \alpha'|g, \alpha\rangle = \frac{(l|[\![g', \alpha']\!] \otimes [\![g, \alpha]\!]|r)}{(l|r)}. \tag{4.7}$$

$[\![g, \alpha]\!] := (...X^g X^g Z_\alpha)$ and $[\![g', \alpha']\!] := \left(...X^{g'} X^{g'} Z_{\alpha'}\right)$ act on the bra and ket indices of fixed points respectively (Fig. 4.4b). We will assume that the endpoints of semi-infinite strings $(...X^g X^g Z_\alpha)$ and $(...X^{g'} X^{g'} Z_{\alpha'})$ in $\langle g', \alpha'|g, \alpha\rangle$ lie at the same location.

4.1.6 Topological phases

We briefly review distinct topological phases before studying them in the unified framework of $\mathbb{Z}_4$ invariant tensors.

$D(\mathbb{Z}_N)$ quantum double

$D(\mathbb{Z}_N)$ quantum doubles (QD) are higher-order generalizations of Kiteav's $D(\mathbb{Z}_2)$ toric code [7]. The model can be defined on the hexagonal lattice where the Hamiltonian has the form

$$H_{\mathbb{Z}_N} = -\sum_{\text{vertices}} \quad - \sum_{\text{plaquettes}} \tag{4.8}$$

We define —●— := X and —●— := Z. X and Z are the generators of the cyclic group $\mathbb{Z}_N$ and the two are related to each other by the Fourier transform (i.e., $X = HZH^\dagger$) and satisfy the following relation,

$$ZX - \exp(2\pi i/N)\, XZ = 0 \tag{4.9}$$

$H_{\mathbb{Z}_N}$ has a particular property that it is an example of frustration-free Hamiltonian (i.e., the ground state of the Hamiltonian is also the ground state of each local term in the Hamiltonian).

Every site on each edge of the honeycomb lives in the N dimensional Hilbert space with basis vectors $|0\rangle, |1\rangle, ..., |N-1\rangle$. The basis vectors can label different flux lines from $0..N-1$. The vertex terms in (4.8) enforce Gauss Law. In the ground state manifold, the net flux around each vertex is zero. The constraint imposed by the vertex terms in (4.8) on a unit cell of hexagonal lattice can be summarized as follows

$$i + j - l - m = 0 \pmod N \quad , \tag{4.10}$$

To summarize, the vertex terms in (4.8) put a restraint on the possible configurations in the ground state manifold, and the plaquette terms create the resonance between different configurations up to the charge (also called parity for $\mathbb{Z}_2$) of the sector. The resulting ground state is a superposition of all the configurations within the charge sector.

Toric code model

The ground state of the Kiteav's $D(\mathbb{Z}_2)$ QD is an equal weight superposition of closed loop configurations. A tensor network representation of the ground state was described in Sec. 2.4. The parity constraints of closed loop patterns ensure that the on-site tensors have $\mathbb{Z}_2$ symmetry. Here, we enlarge the bond dimension of local virtual spaces from two to four and give two tensor network descriptions of toric code in the form of $\mathbb{Z}_4$-invariant tensors.

The first construction of the toric code involves the embedding of loop patterns in two dimensional subspace while discarding the rest. The pictorial description of the on-site tensor is given in Fig. 4.5. The on-site tensor is invariant under $\mathbb{Z}_4$ action on the virtual indices.

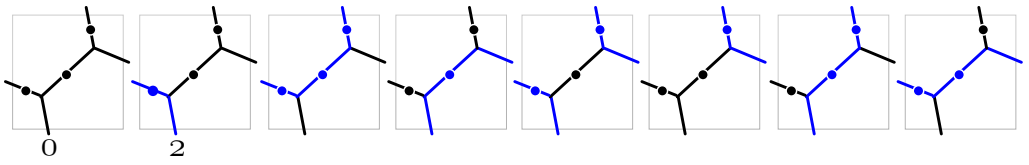

FIGURE 4.5: Solid circles represent the physical index. Blue (black) circles on the edges specify the presence (absence) of string. Virtual indices and the labels for sites with and without strings are indicated at the lower left corner. The on-site tensor A can be interpreted as the sum of all the configurations above.

There exists another way to embed the toric code wavefunction in the four dimensional space. The idea is to use two copies of closed loop patterns and fully exploit the four dimensional virtual space. The resulting description of the on-site tensors is given in Fig. 4.6.

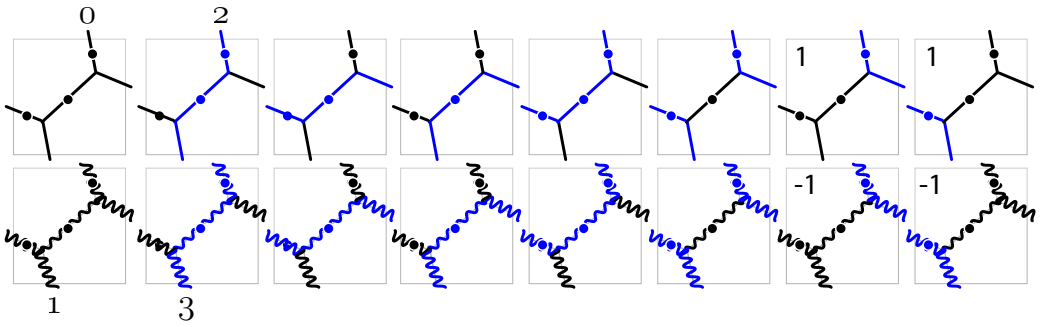

FIGURE 4.6: Solid circles represent the physical index. Blue(black) circles on the edges specify the presence(absence) of string. Virtual indices with labels for possible configurations are shown at the top and bottom of first two columns. Straight and wiggly lines represent two decoupled copies of toric code at the virtual level. Amplitudes in the last two columns have been adjusted from 1 to -1 to keep $\mathbb{Z}_4$ invariance.

Double semion model

Closely related to the toric code is the double semion model. The ground state of the double semion model is characterized by the superposition of possible loop patterns where in contrast to the toric code model, configurations with an odd number of closed loops are weighted by -1 [19, 64].

The tensor network of the double semion model on the honeycomb can be given by assigning an Ising (color) variable to each hexagon and by interpreting strings as the

difference of color on two sides. The weighting factors can be calculated by assigning appropriate amplitudes to configurations in local tensor (Fig. 4.7). The virtual symmetry of the resulting tensor is given by $X = \sigma_x \oplus i\sigma_x$, where σ_x is spin-1/2 Pauli matrix.

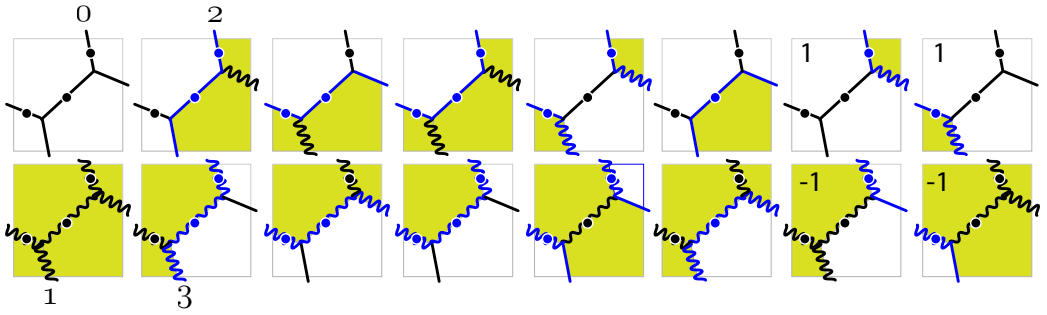

FIGURE 4.7: Sum of configurations in the two rows gives double semion model. Solid circles represent the physical index. Blue(black) circles on the edges specify the presence(absence) of string for the double semion model. Labels $\{0, 1, 2, 3\}$ at the top and bottom of the first two columns give the encoding of strings and vacuum at the virtual level for the double semion model. Group action on the virtual indices switches between the pair of matrix elements in each column.

4.2 Topological phases of $\mathbb{Z}_4$-invariant tensors

We now describe the tensor network constructions for the renormalization group (RG) fixed points of topological phases which can be realized by $\mathbb{Z}_4$-invariant tensors. It is important to note that the form of local tensor which we use for describing the RG fixed point of a topological phase is motivated by the symmetry properties of the transfer operator's fixed points, i.e., by using these local tensor constructions, we can explicitly derive the fixed points of the transfer operator. Furthermore, we discuss the condensation and confinement pattern of anyons in distinct topological phases.

The patterns of symmetry breaking and topologically trivial/non-trivial phases which can be realized in the case of $\mathbb{Z}_N$-invariant tensors have been studied in [63]. In the case of $\mathbb{Z}_4$-invariant tensors, the partition of different phases and the symmetry properties of their fixed points are given in Fig. 4.8, where the symmetry group of each node (topological phase) is $\mathbb{Z}_i \boxtimes \mathbb{Z}_j \cong \mathbb{Z}_i \times \mathbb{Z}_j$. The use of $\boxtimes$ instead of $\times$ is to emphasize the structure of group actions which define the symmetry. For example, $\mathbb{Z}_4$ in $\mathbb{Z}_4 \boxtimes \mathbb{Z}_2$ consists of diagonal elements of the form (X, X) and the generator of $\mathbb{Z}_2$ is $(\mathbb{I}, X^2)$. X^2 in the action $(\mathbb{I}, X^2)$ acts on the bra and $\mathbb{I}$ on the ket layer of fixed points.

Now, for a systematic application of ideas, we study a class of topological phases which could be realized in terms of tensors with a certain underlying symmetry namely the

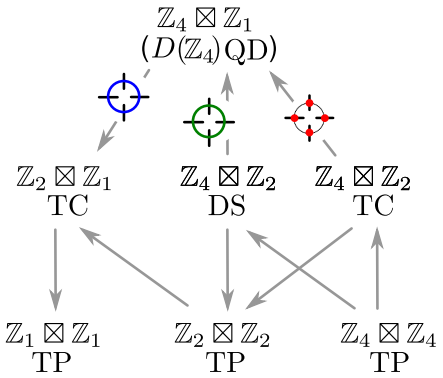

FIGURE 4.8: Patterns of symmetry breaking in the fixed points of the transfer operator. Each node corresponds to a topologically trivial/non-trivial phase of $\mathbb{Z}_4$-invariant tensors. Arrowheads point in the direction of reduced symmetry. The description of MPO projectors is given in the text.

$\mathbb{Z}_4$-invariant tensors [9]. Other than providing a description of quantum doubles which include $D(\mathbb{Z}_4)$, $D(\mathbb{Z}_2)$, and $D(\mathbb{Z}_1)$, the class of $\mathbb{Z}_4$-invariant tensors is rich enough to encode a twisted quantum double $D_t(\mathbb{Z}_2)$ which is also known as the double semion model. Both the $D(\mathbb{Z}_2)$ quantum double which we refer to as toric code and the double semion model can be obtained from $D(\mathbb{Z}_4)$ quantum double by applying continuous deformations. Furthermore, the application of the ideas of anyon condensation and confinement enables us not only to study the toric code and double semion model in a unified manner, but this approach also allows us to sketch the phase diagram of all phases which could be modeled by $\mathbb{Z}_4$-invariant tensors.

4.2.1 $D(\mathbb{Z}_4)$ quantum double

$D(\mathbb{Z}_4)$ quantum double (QD) is a topological model which can be realized on an oriented lattice where at each edge there exists a flux line labeled $\{0, 1, 2, 3\}$, and the conservation of flux is enforced on each vertex, i.e.,

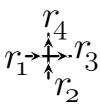

$$, \quad r_1 + r_2 - r_3 - r_4 = 0 \pmod 4. \tag{4.11}$$

The tensor network description of $D(\mathbb{Z}_4)$ QD can be given by $\mathbb{Z}_4$-isometric tensor as defined in (4.2). We begin by writing down the on-site tensor for the ground state of $D(\mathbb{Z}_4)$ QD as an MPO.

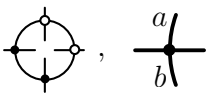

(4.12)

and $a, b \in \{0, 1, 2, 3\}$. The black ring in (4.12) is another graphical representation of local tensor given in Fig. 4.1a. Open ends on the inside (outside) of ring denote the

physical r_i (virtual v_i) indices of on-site tensor. X is the generator of $\mathbb{Z}_4$ and the white color of solid circles indicates Hermitian conjugate.

The construction in (4.12) can be motivated from a physical point of view by considering X as a generator of $\mathbb{Z}_4$ with diagonal representation. Then the constraints on flux at each vertex can be modeled very naturally in terms of local tensors. Each entry of on-site tensor is non-zero if (4.11) is satisfied, i.e.,


$$= \begin{cases} 1 & v_1 + v_2 - v_3 - v_4 = 0 \pmod 4, r_i = v_i \\ 0 & \text{otherwise} \end{cases}, \tag{4.13}$$

where indices $r_i, v_i \in \{0, 1, 2, 3\}$. Blocking of on-site tensors while contracting the virtual indices leads to the superposition of all the configurations having zero net flux through every vertex.

Now, we construct the fixed points of the transfer operator at the RG fixed point of $D(\mathbb{Z}_4)$ QD. Before proceeding further, we note that with the properly chosen normalization factor, the MPO in (4.12) squares to itself. Furthermore, the MPO is also Hermitian, so it leads to the on-site transfer operator (Fig. 4.1d) with same representation as (4.12). The fixed points of the transfer operator and their symmetry properties can be deduced by using the following property of MPO tensors.

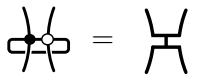
$$\tag{4.14}$$

The RHS acts like a δ-tensor, and it is equal to zero except for the diagonal entries. Using (4.14), we can write the transfer operator for the ground state of $D(\mathbb{Z}_4)$ QD as

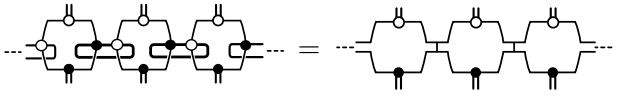
$$\tag{4.15}$$

δ-tensors between sites sync-up the entries and the transfer operator can be written as a sum of four product operators.

$$\mathbb{T} = \sum_{g=0}^{3} \left(X^g \otimes X^{g\dagger} \right)^{\otimes N_v}, \tag{4.16}$$

where $N_v \to \infty$ in the thermodynamic limit. By rewriting the entries in the sum, we can show that the following four product states are the fixed points of the transfer operator.

$$(X^g)^{\otimes N_v}, \text{ where } g \in \{0, 1, 2, 3\}. \tag{4.17}$$

We will write the fixed points (which are pure states) of the transfer operator for convenience as a density matrix by flipping the ket index of fixed points. Each of the fixed point of the transfer operator in (4.17) breaks $\mathbb{Z}_4 \boxtimes \mathbb{Z}_4$ symmetry of the transfer operator down to $\mathbb{Z}_4 \boxtimes \mathbb{Z}_1$. They are invariant under the diagonal action (X, X) on the bra and ket layer. It is also important to note a correspondence between the symmetry broken fixed points of the transfer operator and the different blocks in the local tensor network description of the RG fixed point. The MPO tensor in (4.12) contains four independent blocks, and each block can be identified with one of the fixed points of the transfer operator in (4.17).

The behavior of operators which act trivially (up to a phase factor) on the fixed points of the transfer operator can be explained by their action on local tensors.

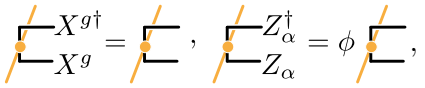

(4.18)

where ϕ is an additional phase factor whose exact value depend on the fixed point and the charge label α. The yellow tensor denotes a fixed point of the transfer operator (Fig. 4.4a). Using (4.18) we can deduce that none of the possible anyons are confined in $D(\mathbb{Z}_4)$ QD phase. Moreover, actions of the form (X^{g_1}, X^{g_2}) or $(Z_{\alpha_1}, Z_{\alpha_2})$, where $g_1 \neq g_2$ and $\alpha_1 \neq \alpha_2$, on the local tensors of fixed points generate blocks which lead to orthogonal states, so none of the flux or charge anyon are condensed in $D(\mathbb{Z}_4)$ QD phase. Condensation and confinement pattern of anyons at the RG fixed point of $D(\mathbb{Z}_4)$ QD phase can be summarized as

$$\langle g', \alpha' | g, \alpha \rangle = \begin{cases} 1 & g' = g,\ \alpha' = \alpha \\ 0 & \text{otherwise.} \end{cases}$$

The overlap is non-zero only if it is associated with a confinement fraction.

4.2.2 Toric code model

We described in Sec. 4.1.6 two different embeddings of the toric code (TC) model (i.e., the ground state of $D(\mathbb{Z}_2)$ QD) by using $\mathbb{Z}_4$-invariant tensors. The two realizations of the toric code model enforce different patterns of symmetry breaking for the fixed points of the transfer operator. In one case, the fixed points of the transfer operator have $\mathbb{Z}_4 \boxtimes \mathbb{Z}_2$ symmetry whereas in the other the fixed points of the transfer operator break $\mathbb{Z}_4 \boxtimes \mathbb{Z}_4$ symmetry to $\mathbb{Z}_2 \boxtimes \mathbb{Z}_1$.

In the following, we first give the tensor network constructions of the two toric codes by using MPO projectors and the action of two different MPO projectors on the physical indices of $D(\mathbb{Z}_4)$ QD gives the two toric codes.

$\mathbb{Z}_4 \boxtimes \mathbb{Z}_2$ Toric code

An action which is given by projector, $(\mathbb{I} + X^2)^{\otimes 4}$, on the local tensors of $D(\mathbb{Z}_4)$ QD yields a tensor for the RG fixed point of the TC phase where the fixed points of the transfer operator have $\mathbb{Z}_4 \boxtimes \mathbb{Z}_2$ symmetry.

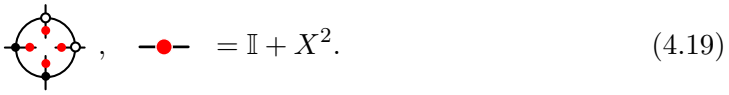

(4.19)

The action of red bubbles on the black ring gives two independent blocks, and the resulting tensor can be written as an MPO with bond dimension two.

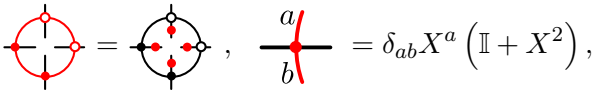

(4.20)

and $a, b \in \{0, 1\}$. The intuition behind (4.20) as the tensor network description for the RG fixed point of TC phase can be understood from the following equivalence

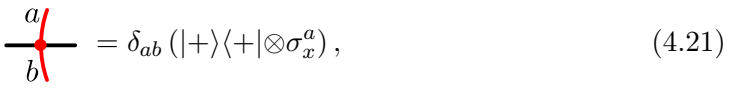

(4.21)

where $a, b \in \{0, 1\}$ and σ_x is the generator of $\mathbb{Z}_2$. $\mathbb{Z}_4 \boxtimes \mathbb{Z}_2$ TC can be viewed as an extension of $D(\mathbb{Z}_2)$ QD with an ancilla qubit.

The on-site transfer operator of $\mathbb{Z}_4 \boxtimes \mathbb{Z}_2$ TC also satisfies the 'delta' relation as given in (4.14) and each of the two blocks in (4.20) can be identified with a symmetry broken fixed point of the transfer operator. Fixed points of the transfer operator can be written as product states of the form

$$\left(\mathbb{I} + X^2\right)^{\otimes N_v}, \ \left(X + X^3\right)^{\otimes N_v} \ \text{as} \ \ N_v \to \infty, \tag{4.22}$$

Each of the fixed points is invariant under the (X, X) action on the bra and ket indices. An Action of the form $(\mathbb{I}, X^2)$ also leaves the fixed points invariant. Both (X, X) and $(\mathbb{I}, X^2)$ generate $\mathbb{Z}_4 \boxtimes \mathbb{Z}_2$. The action of the elements of $\mathbb{Z}_4 \boxtimes \mathbb{Z}_2$ on the local tensors of the fixed points can be summarized as follows

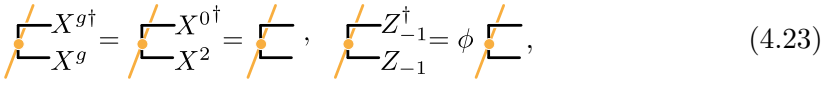

(4.23)

where ϕ is a phase factor with a value which depends on the fixed point. Using (4.23), we can derive the condensation and confinement pattern of anyons at the RG fixed point of $\mathbb{Z}_4 \boxtimes \mathbb{Z}_2$ TC phase.

$$\langle g', \alpha' | g, \alpha \rangle = \begin{cases} 1 & g' = g \pmod 2,\ \alpha' = \alpha = 1 \text{ or } -1 \\ 0 & \text{otherwise,} \end{cases}$$

where g, g' represent the conjugacy classes (group elements) of $\mathbb{Z}_4$ while α, α' are the irreps.

$\mathbb{Z}_2 \boxtimes \mathbb{Z}_1$ Toric code

The tensor network description of the other toric code in the framework of $\mathbb{Z}_4$-invariant tensors can be obtained by applying projection on the dual basis. In contrast to $\mathbb{Z}_4 \boxtimes \mathbb{Z}_2$ TC, the projection in the dual basis reduces the symmetry of fixed points of the transfer operator to $\mathbb{Z}_2 \boxtimes \mathbb{Z}_1$, and the largest eigenvector subspace of the transfer operator is spanned by eight symmetry broken fixed points. An action of the form $\left(\mathbb{I} + Z^2\right)^{\otimes 4} + \left(\mathbb{I} - Z^2\right)^{\otimes 4}$ on the local tensor of $D\left(\mathbb{Z}_4\right)$ QD generates an MPO with eight blocks.

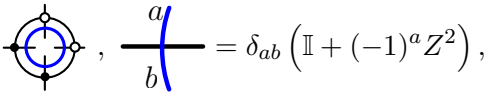

$$= \delta_{ab} \left(\mathbb{I} + (-1)^a Z^2\right), \tag{4.24}$$

$a, b \in \{0, 1\}$, and $Z := Z_1$.

The on-site transfer operator of $\mathbb{Z}_2 \boxtimes \mathbb{Z}_1$ TC also satisfy the 'delta' relation similar to (4.14) and each block can be identified with one of the symmetry broken fixed points of the transfer operator. The fixed points of the transfer operator are

$$\left(X^a \left(\mathbb{I} + (-1)^b Z^2\right)\right)^{\otimes N_v}, \tag{4.25}$$

where $a \in \{0, 1, 2, 3\}$ and $b \in \{0, 1\}$. The fixed points of $\mathbb{Z}_2 \boxtimes \mathbb{Z}_1$ TC remain invariant under actions of the form

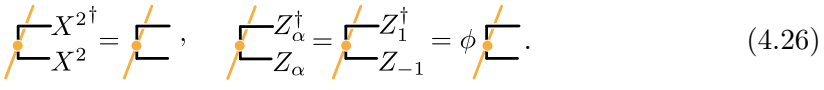

(4.26)

Overlap of anyonic wavefunctions which summarize the condensation and confinement pattern of anyon at the RG fixed point of $\mathbb{Z}_2 \boxtimes \mathbb{Z}_1$ TC phase are

$$\langle g', \alpha' | g, \alpha \rangle = \begin{cases} 1 & g' = g = 0 \text{ or } 2,\ \alpha' = (-1)^a \alpha \\ 0 & \text{otherwise,} \end{cases}$$

where $a \in \{0, 1\}$.

4.2.3 Double semion model

Double semion (DS) model as discussed earlier in Sec. 4.1.6 describes a twisted $D_t(\mathbb{Z}_2)$ QD and while being simple, it has no tensor network description in terms of $\mathbb{Z}_2$-invariant tensors and the simplest un-twisted description requires $\mathbb{Z}_4$-invariance [65]. Fixed points of the transfer operator in the case of the DS model have been determined to have $\mathbb{Z}_4 \boxtimes \mathbb{Z}_2$ symmetry [63]. Although the fixed points have the same symmetry as in the case of $\mathbb{Z}_4 \boxtimes \mathbb{Z}_2$ TC, a defining feature of the DS model is the boundary phase with non-local string order parameter. The local tensor of the DS model can be constructed by applying an MPO projector on $D(\mathbb{Z}_4)$ QD.

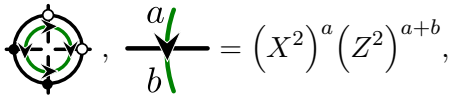

$$= \left(X^2\right)^a \left(Z^2\right)^{a+b}, \tag{4.27}$$

and $a \in \{0, 1\}$. Arrowheads in the ring point in the direction of index b. The form of DS MPO projector (green tensor) is motivated by the fact that this construction enables us to retrieve the fixed points of the transfer operator directly from the local tensor description, in keeping with the spirit of previous constructions. The composition of $D(\mathbb{Z}_4)$ QD (black ring) and $\mathbb{Z}_4 \boxtimes \mathbb{Z}_2$ DS (green ring) projector gives an MPO with two independent blocks and each block has a dimension of two. It should be emphasized here that the construction which is given in (4.27) can be mapped to the 'canonical' description of the double semion model in terms of loop patterns by transforming on-site tensors by local unitaries (see Sec. 4.1.6). Furthermore, the tensor network description of the double semion model breaks the lattice symmetries. This can be seen from the following decomposition of the DS projector.

$$= \left(\mathbb{IIII} + \mathbb{II}Z^2Z^2\right)\left(\mathbb{IIII} + \left(X^2Z^2\right)\left(X^2Z^2\right)\mathbb{II}\right)\left(\mathbb{IIII} + \mathbb{I}Z^2\left(X^2Z^2\right)\mathbb{I}\right) \tag{4.28}$$

Blocking of the on-site transfer operators of $\mathbb{Z}_4 \boxtimes \mathbb{Z}_2$ DS model results in a δ-tensor, similar to the case of $D(\mathbb{Z}_4)$ QD in (4.14) but with an additional structure. Fixed points of DS model which breaks the $\mathbb{Z}_4 \boxtimes \mathbb{Z}_4$ symmetry of the transfer operator down to $\mathbb{Z}_4 \boxtimes \mathbb{Z}_2$ can be identified with independent blocks in (4.27), we can write the MPS tensors for the fixed points of the transfer operator as

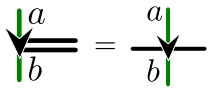

$$= X^i\left(X^2\right)^a\left(Z^2\right)^{a+b}, \tag{4.29}$$

where $i \in \{0, 1\}$ and the green line has bond dimension 2. Fixed points in the case of the DS model cannot be written as the product states. Symmetry actions of the form (X^g, X^g) and (X^0, X^2) on the physical indices can be absorbed only by non-trivial action on the 'virtual' indices of fixed points, which leads to the fact that the boundary phase of the DS model can only be characterized by string order parameter $(...\mathbb{III}, ...X^2X^2Z^2)$ in contrast to the local order parameter in boundary phase of $\mathbb{Z}_4 \boxtimes \mathbb{Z}_2$ TC. The boundary phase of the DS model has symmetry protected topological (SPT) order. The existence of a string order parameter can be explained by the following properties of fixed point local tensors.

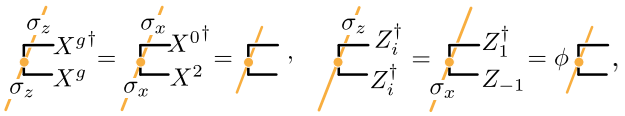

(4.30)

where σ_x and σ_z are the Pauli matrices and ϕ is an additional phase factor. Using (4.30), we can derive the condensation and confinement properties at the RG fixed point of DS phase. Let $a \in \{0, 1\}$ then the overlap of anyonic wavefunctions can be written as

$$\langle g', \alpha' | g, \alpha \rangle = \begin{cases} 1 & g' = g = a \pmod 2, \\ & \alpha \in \{i^a, -i^a\}, \alpha' = i^{(g-g')}\alpha \\ 0 & \text{otherwise,} \end{cases}$$

4.2.4 Topologically trivial phases

Although topologically trivial phases (TP) do not support the existence of non-trivial anyons, it is possible to realize trivial phases with boundary phases having distinct symmetries. Each trivial phase is characterized by a unique set of anyons which are condensed.

$\mathbb{Z}_4 \boxtimes \mathbb{Z}_4$ Trivial phase

$\mathbb{Z}_4 \boxtimes \mathbb{Z}_4$ TP can be obtained by applying a projector $(\mathbb{I} + X + X^2 + X^3)^{\otimes 4}$ on the physical indices of $D(\mathbb{Z}_4)$ QD. The action leads to the collapsing of four blocks in the MPO tensor of $D(\mathbb{Z}_4)$ QD into a single block. Since the fixed point is unique, it inherits all the symmetries of the transfer operator and it is invariant under $\mathbb{Z}_4 \boxtimes \mathbb{Z}_4$. A manifestation of $\mathbb{Z}_4 \boxtimes \mathbb{Z}_4$ symmetry is the condensation of all the flux anyons. Condensation and confinement properties of anyons in the $\mathbb{Z}_4 \boxtimes \mathbb{Z}_4$ TP can be summarized as

$$\langle g', \alpha' | g, \alpha \rangle = \begin{cases} 1 & \alpha' = \alpha = 1 \\ 0 & \text{otherwise.} \end{cases}$$

$\mathbb{Z}_2 \boxtimes \mathbb{Z}_2$ Trivial phase

There exists a topologically trivial phase where the fixed points of the transfer operator break all but the $\mathbb{Z}_2 \boxtimes \mathbb{Z}_2$ symmetry. The $\mathbb{Z}_2 \boxtimes \mathbb{Z}_2$ symmetry action on the bra and ket indices is given by the generators (X^2, X^2) and $(\mathbb{I}, X^2)$. The RG fixed point of $\mathbb{Z}_2 \boxtimes \mathbb{Z}_2$ TP can be written as

$$= \delta_{ab} \left(\mathbb{I} + X^2\right) \left(\mathbb{I} + (-1)^a Z^2\right), \tag{4.31}$$

where $a = \in \{0, 1\}$. MPO projector (brown ring) acts on the local tensor of $D(\mathbb{Z}_4)$ QD (black ring) . Four fixed points of the transfer operator in $\mathbb{Z}_2 \boxtimes \mathbb{Z}_2$ TP are as follows

$$\begin{aligned} &\left(\left(\mathbb{I} + X^2\right)\left(\mathbb{I} + Z^2\right)\right)^{\otimes N_v}, \ \left(\left(X + X^3\right)\left(\mathbb{I} + Z^2\right)\right)^{\otimes N_v}, \\ &\left(\left(\mathbb{I} + X^2\right)\left(\mathbb{I} - Z^2\right)\right)^{\otimes N_v}, \ \left(\left(X + X^3\right)\left(\mathbb{I} - Z^2\right)\right)^{\otimes N_v}. \end{aligned} \tag{4.32}$$

Furthermore, the condensation and confinement pattern of anyons in $\mathbb{Z}_2 \boxtimes \mathbb{Z}_2$ TP can be given by

$$\langle g', \alpha' | g, \alpha \rangle = \begin{cases} 1 & g, g' \in \{0, 2\}, \ \alpha', \alpha \in \{1, -1\} \\ 0 & \text{otherwise.} \end{cases}$$

$\mathbb{Z}_1 \boxtimes \mathbb{Z}_1$ Trivial phase

A completely symmetry broken trivial phase is obtained by acting with an MPO projector with bond dimension 4.

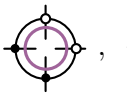

$$= \delta_{ab} \sum_{j=0}^{3} (i^a Z)^j, \tag{4.33}$$

where $a, b \in \{0, 1, 2, 3\}$. The effective MPO which is obtained by composing black and violet rings has bond dimension 16 and the local tensors of it contain 16 blocks each leading to one of the symmetry broken fixed point.

$\mathbb{Z}_1 \boxtimes \mathbb{Z}_1$ TP only supports the existence of charge excitations which are condensed.

$$\langle g', \alpha' | g, \alpha \rangle = \begin{cases} 1 & g = g' = 0 \\ 0 & \text{otherwise.} \end{cases}$$

4.3 Modeling of phase transitions between the phases of $\mathbb{Z}_4$-invariant tensors

Phases with distinct topological orders defined earlier in the context of $\mathbb{Z}_4$-invariant tensors set a playing field where these phases can be deformed and allow for different excursions in the phase diagram. In this section, we develop an intuitive picture for different manipulations on local tensors. These continuous actions enable us to explore the behavior of many-body systems at the interface of different topological (trivial/non-trivial) phases, where their boundaries meet.

On an abstract level, we can label the mechanisms of different phase transitions which we study here as *local filtering* and *effective linear interpolations*. In the following, we will give a detailed account of the two. Results regarding the universal features of the phase transitions which we describe here are presented in Sec. 4.4 and 4.5.

4.3.1 Local filtering operations

The idea of local filtering operations was introduced in [66] and it was later adopted in [67] for their applications in tensor networks. Their action on local tensors (which corresponds to an additional field in parent Hamiltonian) effectively emulates a filtering of different strings. When applied to the ground state of $D(\mathbb{Z}_2)$ QD, it penalizes strings which form closed loops and drives the system into a topologically trivial phase [66]. The goal here is to construct filtering operations which could be applied in a more general setting, and these operations should enable the realization of different projections in the limiting case as a function of some parameter. It is important to be emphasized that the *form* of different deformations which we construct here is partially motivated by the analytic rigor or closed form solutions one could obtain from them without affecting the universal features of the underlying phase transition.

The order of discussion is in the same spirit as Fig. 4.8. We begin by discussing string tensions which connect $D(\mathbb{Z}_4)$ QD to TCs and DS model. Next, we describe filtering operations which govern the phase transitions from TCs and DS model to trivial phases.

$D(\mathbb{Z}_4)$ QD and $\mathbb{Z}_4 \boxtimes \mathbb{Z}_2$ TC

A defining feature of $D(\mathbb{Z}_4)$ QD is the possibility of four different flux lines at each site in contrast to the TC and DS model which have only two. It is obvious to consider a local filtering which amplifies (or restricts) the amplitude of certain flux lines. And indeed, the approach does give a direct phase transition between $D(\mathbb{Z}_4)$ QD and $\mathbb{Z}_4 \boxtimes \mathbb{Z}_2$ TC.

To understand the action, it is more lucid to consider X with diagonal representation. An action of the form $\exp\left(\theta_{\mathrm{TC}} X^2\right) = diag\left(e^{\theta_{\mathrm{TC}}}, e^{-\theta_{\mathrm{TC}}}, e^{\theta_{\mathrm{TC}}}, e^{-\theta_{\mathrm{TC}}}\right)$ on the physical legs of $D\left(\mathbb{Z}_4\right)$ QD will amplify flux lines 0 and 2, while suppressing lines 1 and 3. Since $\exp\left(\theta_{\mathrm{TC}} X^2\right) = \cosh\theta_{\mathrm{TC}}\ \mathbb{I} + \sinh\theta_{\mathrm{TC}}\ X^2$, for large values of θ_{TC} the deformation acts effectively as a projector of the form $\left(\mathbb{I} + X^2\right)$. Furthermore, the behavior is independent of how one chooses to represent X.


, where  $= \exp(\theta_{\mathrm{TC}} X^2)$. (4.34)

At $\theta_{\mathrm{TC}} = 0$, the deformation acts trivially, whereas at $\theta_{\mathrm{TC}} = \infty$, the system is in $\mathbb{Z}_4 \boxtimes \mathbb{Z}_2$ TC phase. The phase transition can be understood in terms of spontaneous symmetry breaking from a symmetry broken phase (the fixed points of the transfer operator in $D\left(\mathbb{Z}_4\right)$ QD are not invariant under $\left(\mathbb{I}, X^2\right)$ action) to a 'disordered' phase (the fixed points in $\mathbb{Z}_4 \boxtimes \mathbb{Z}_2$ TC phase are invariant under $\left(\mathbb{I}, X^2\right)$ action) where a symmetry has been restored. Moreover, it is possible to modify local tensors such that the transfer operator is no longer invariant under the action $\left(\mathbb{I}, X^2\right)$ on its virtual legs. This corresponds to adding an external field which explicitly breaks the symmetry and it can be implemented by adding an action $:= diag(1+h, 1-h, 1-h, 1+h)$ on the virtual legs of $D\left(\mathbb{Z}_4\right)$ QD tensor.

 (4.35)

Later in Sec. 4.5.1, we will study the response of order parameters (condensation and confinement fractions) to an external field and the further insights which it reveals about the nature of the phase transition.

$D\left(\mathbb{Z}_4\right)$ QD and $\mathbb{Z}_2 \boxtimes \mathbb{Z}_1$ TC

Now, to get $D\left(\mathbb{Z}_4\right)$ QD $\leftrightarrow$ $\mathbb{Z}_2 \boxtimes \mathbb{Z}_1$ TC phase transition, it is natural to apply string tension on the dual basis.

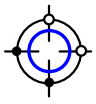
, where 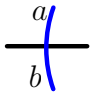 $= \delta_{ab} \exp\left((-1)^a \theta_{\mathrm{TC},Z_2} Z^2\right)$ (4.36)

and $a, b \in \{0, 1\}$. For $\theta_{\mathrm{TC},Z_2} = \infty$, blue ring acts as a projector $\left(\mathbb{I} + Z^2\right)^{\otimes 4} + \left(\mathbb{I} - Z^2\right)^{\otimes 4}$, whose action on $D\left(\mathbb{Z}_4\right)$ QD (black ring) gives eight blocks, and each block can be identified with one of the symmetry broken fixed point of the transfer operator. The phase transition can be understood as a spontaneous reduction in the symmetry of the

fixed points from $\mathbb{Z}_4 \boxtimes \mathbb{Z}_1$ down to $\mathbb{Z}_2 \boxtimes \mathbb{Z}_1$, while the transfer operator remains $\mathbb{Z}_4 \boxtimes \mathbb{Z}_4$ invariant.

$D(\mathbb{Z}_4)$ QD and $\mathbb{Z}_4 \boxtimes \mathbb{Z}_2$ DS

The action of deformations (4.34) and (4.36), on $D(\mathbb{Z}_4)$ QD in the limiting case give $\mathbb{Z}_4 \boxtimes \mathbb{Z}_2$ TC and $\mathbb{Z}_2 \boxtimes \mathbb{Z}_1$ TC respectively. Using the same insight, it is possible to derive $D(\mathbb{Z}_4)$ QD $\leftrightarrow$ $\mathbb{Z}_4 \boxtimes \mathbb{Z}_2$ DS phase transition by acting with string tension on the virtual indices of DS MPO projector as defined in (4.27).

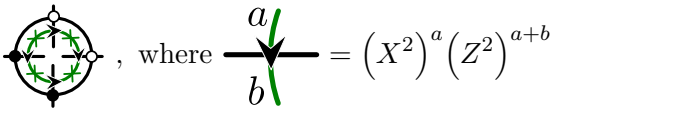

$$, \text{ where } = \left(X^2\right)^a \left(Z^2\right)^{a+b} \tag{4.37}$$

and 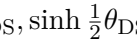 $= diag(\cosh \frac{1}{2}\theta_{\text{DS}}, \sinh \frac{1}{2}\theta_{\text{DS}})$. At $\theta_{\text{DS}} = 0$,  $= |0\rangle\langle 0|$, and whole ring acts trivially, whereas for $\theta_{\text{DS}} \gg 0$,  $= \mathbb{I}_2$ and the green ring acts to give DS phase.

$D(\mathbb{Z}_4)$ QD and topological phase transitions

We have described how one can deform $D(\mathbb{Z}_4)$ QD down to TCs in (4.34) and (4.36), and down to the DS model in (4.37). The red, blue, and green deformations all commute with each other. Moreover, they also commute with $D(\mathbb{Z}_4)$ QD tensor (black ring). So, it is possible to compose them in a way which allows for more exotic phase transitions.

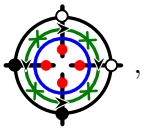

$$, \tag{4.38}$$

where red, blue and green tensors have the same definitions as given in (4.34), (4.36), and (4.37) respectively. The deformation given by the total action of red, blue and green tensors is parametrized by $\boldsymbol{\theta} := (\theta_{\text{TC}}, \theta_{\text{TC},Z_2}, \theta_{\text{DS}})$. The qualitative behavior of the composite deformation can be understood from its extremal properties.

At $\boldsymbol{\theta} = (0,0,0)$, each of the three deformations act trivially and the local tensor describe the RG fixed point of $D(\mathbb{Z}_4)$ QD. At the axes endpoints

- $\boldsymbol{\theta} = (\infty, 0, 0)$, deformations corresponding to $\mathbb{Z}_2 \boxtimes \mathbb{Z}_1$ TC (blue ring) and $\mathbb{Z}_4 \boxtimes \mathbb{Z}_2$ DS (green ring) act trivially. Red bubbles act as a projector $\left(\mathbb{I} + X^2\right)^{\otimes 4}$ and the whole deformation acts to give the RG fixed point of $\mathbb{Z}_4 \boxtimes \mathbb{Z}_2$ TC.

- $\boldsymbol{\theta} = (0, \infty, 0)$, only the deformation corresponding to $\mathbb{Z}_2 \boxtimes \mathbb{Z}_1$ TC acts non-trivially on $D(\mathbb{Z}_4)$ QD to realize the RG fixed point of $\mathbb{Z}_2 \boxtimes \mathbb{Z}_1$ TC.
- $\boldsymbol{\theta} = (0, 0, \infty)$, the deformation acts to realize the RG fixed of $\mathbb{Z}_4 \boxtimes \mathbb{Z}_2$ DS model.

Compositions of any of the two or all the three projectors corresponding to $\mathbb{Z}_4 \boxtimes \mathbb{Z}_2$ TC, $\mathbb{Z}_2 \boxtimes \mathbb{Z}_1$ TC, and $\mathbb{Z}_4 \boxtimes \mathbb{Z}_2$ DS model give the RG fixed point of $\mathbb{Z}_2 \boxtimes \mathbb{Z}_2$ TP.

$\mathbb{Z}_4 \boxtimes \mathbb{Z}_2$ TC and topologically trivial phases

$\mathbb{Z}_4 \boxtimes \mathbb{Z}_2$ TC can be further deformed into $\mathbb{Z}_4 \boxtimes \mathbb{Z}_4$ or $\mathbb{Z}_2 \boxtimes \mathbb{Z}_2$ TP by enhancing or reducing the symmetry of the transfer operator fixed points. The phase diagram of $\mathbb{Z}_4 \boxtimes \mathbb{Z}_2$ TC can be characterized by a deformation parametrized by two parameters.

$$, \text{ where } = \delta_{ab} \frac{1}{2} \left[\cosh\theta_1 \left(\mathbb{I} + X^2 \right) + \sinh\theta_1 \left(X + X^3 \right) \right] \exp\left((-1)^a \theta_2 Z^2 \right), \tag{4.39}$$

$a, b \in \{0, 1\}$ and the black ring represents the local tensor of $D(\mathbb{Z}_4)$ QD. The extremal properties of the deformation are as follows:

- At $(\theta_1, \theta_2) = (0, 0)$, the orange ring acts as a projector on the local tensor of $D(\mathbb{Z}_4)$ QD and gives the RG fixed point of $\mathbb{Z}_4 \boxtimes \mathbb{Z}_2$ TC.
- At $(\theta_1, \theta_2) = (\infty, 0)$, $\cosh\theta_1 = \sinh\theta_1$ and we get $\mathbb{Z}_4 \boxtimes \mathbb{Z}_4$ TP, where the fixed point of the transfer operator is unique.
- At $(\theta_1, \theta_2) = (0, \infty)$, the deformation acts as a projector to give a tensor network representation for the RG fixed point of $\mathbb{Z}_2 \boxtimes \mathbb{Z}_2$ TP.

$\mathbb{Z}_2 \boxtimes \mathbb{Z}_1$ TC and topologically trivial phases

In the case of $\mathbb{Z}_2 \boxtimes \mathbb{Z}_1$ TC by enhancing the symmetry one gets into $\mathbb{Z}_2 \boxtimes \mathbb{Z}_2$ TP, whereas a further reduction in the symmetry of the transfer operator fixed points leads to $\mathbb{Z}_1 \boxtimes \mathbb{Z}_1$ TP where the fixed points break all the symmetries. Phase transitions can be modeled by a deformation which can be tuned by two parameters.

$$, \quad = \delta_{ab} \frac{1}{2} \left[\cosh\theta_1 \left(\mathbb{I} + (-1)^a Z^2 \right) + i^a \sinh\theta_1 \left(Z + (-1)^a Z^3 \right) \right] \exp\left(\theta_2 X^2 / 4 \right) \tag{4.40}$$

and $a, b \in \{0, 1, 2, 3\}$. The behavior of deformation in the limiting cases is as follows:

- At $(\theta_1, \theta_2) = (0, 0)$, the action of light blue ring on $D(\mathbb{Z}_4)$ QD gives an on-site tensor for $\mathbb{Z}_2 \boxtimes \mathbb{Z}_1$ TC.
- At $(\theta_1, \theta_2) = (\infty, 0)$, the deformation acts as a projector for $\mathbb{Z}_1 \boxtimes \mathbb{Z}_1$ TP.
- At $(\theta_1, \theta_2) = (0, \infty)$, the projector restores a broken symmetry and gives $\mathbb{Z}_2 \boxtimes \mathbb{Z}_2$ TP.

$\mathbb{Z}_4 \boxtimes \mathbb{Z}_2$ DS and topologically trivial phases

Here we describe a deformation which allows for the possibility of direct phase transition between $\mathbb{Z}_4 \boxtimes \mathbb{Z}_2$ DS and trivial phases which include $\mathbb{Z}_2 \boxtimes \mathbb{Z}_2$ TP and $\mathbb{Z}_4 \boxtimes \mathbb{Z}_4$ TP.

$$, \text{ where } = \left(X^2\right)^a \left(Z^2\right)^{a+b} \exp(\theta_2 X), \tag{4.41}$$

$= \exp(\theta_1 \sigma_z)$, and σ_z is a Pauli matrix. The deformation given in (4.41) can be justified from its extremal properties.

- At $(\theta_1, \theta_2) = (0, 0)$, $\exp(\theta_1 \sigma_z) = \mathbb{I}_2$ and $\exp(\theta_2 X) = \mathbb{I}_4$, and the light green ring acts as a projector for $\mathbb{Z}_4 \boxtimes \mathbb{Z}_2$ DS model.
- At $(\theta_1, \theta_2) = (\infty, 0)$, $\exp(\theta_1 \sigma_z) = |0\rangle\langle 0|$ and $\exp(\theta_2 X) = \mathbb{I}_4$, the whole deformation acts as an identity and the system in $D(\mathbb{Z}_4)$ QD phase.
- At $(\theta_1, \theta_2) = (0, \infty)$, $\exp(\theta_1 \sigma_z) = \mathbb{I}_2$, on the other hand $\exp(\theta_2 X)$ acts as a projector of the form $\mathbb{I} + X + X^2 + X^3$. The collective action realizes $\mathbb{Z}_2 \boxtimes \mathbb{Z}_2$ TP.
- At $(\theta_1, \theta_2) = (\infty, \infty)$, the deformation acts to give a projector for $\mathbb{Z}_4 \boxtimes \mathbb{Z}_4$ TP. There exists a direct path between $\mathbb{Z}_4 \boxtimes \mathbb{Z}_2$ DS and $\mathbb{Z}_4 \boxtimes \mathbb{Z}_4$ TP via a multi-critical regime (see Sec. 4.5.5).

4.3.2 Effective linear interpolations

Now, we describe another approach to the study of phase transitions. In principle, one can also consider *effective linear interpolations* as a special case of local filtering operations, but the emphasis here is on the interpolation of the on-site transfer operators since this approach is more robust to retrieve direct phase transitions.

We start by defining two on-site tensors A_1 and A_2 which define the RG fixed point of two distinct phases. We assume that A_1 and A_2 can be obtained by applying projectors on the local tensor of $D(\mathbb{Z}_4)$ QD, i.e., $A_1 = \boldsymbol{P}_1 A_{D(\mathbb{Z}_4)}$ and $A_2 = \boldsymbol{P}_2 A_{D(\mathbb{Z}_4)}$, where $A_{D(\mathbb{Z}_4)}$ denotes the on-site tensor of $D(\mathbb{Z}_4)$ QD. Furthermore, $\boldsymbol{P}_1$ and $\boldsymbol{P}_2$ are Hermitian and $[\boldsymbol{P}_1, \boldsymbol{P}_2] = 0$.

It is instructive to first consider a linear interpolation of on-site tensors.

$$A(\theta) = \theta A_1 + (1-\theta) A_2 \tag{4.42}$$

Since the projectors $\boldsymbol{P}_1$ and $\boldsymbol{P}_2$ act on the physical indices, the virtual symmetries remain preserved along the path defined by (4.42). However, linear interpolation of on-site tensors does not always give a direct phase transition between phases which are associated with A_1 and A_2.

The behavior of direct phase transitions can be retrieved more elegantly by considering paths which can be traced by linear interpolation of the on-site transfer operators.

$$\mathbb{E}(\theta) = \theta \mathbb{E}_1 + (1-\theta)\mathbb{E}_2, \tag{4.43}$$

where $\mathbb{E}_m = A_m^\dagger A_m$. The linear interpolation of the on-site transfer operators in (4.43) is achieved by an application of following action on on-site tensors.

$$A(\theta) = \left[\boldsymbol{P}_{12} + \sqrt{\theta}(\boldsymbol{P}_1 - \boldsymbol{P}_{12}) + \sqrt{1-\theta}(\boldsymbol{P}_2 - \boldsymbol{P}_{12})\right] A_{D(\mathbb{Z}_4)}, \tag{4.44}$$

where $\boldsymbol{P}_{12} := \boldsymbol{P}_1 \boldsymbol{P}_2$. Since $(\boldsymbol{P}_{12} - \boldsymbol{P}_m) \perp \boldsymbol{P}_m$, contraction of $A(\theta)$ with its conjugate on physical indices give (4.43).

4.4 Probes for studying topological phase transitions

Here we describe different numerical methods which we later utilize to rigorously study phase transitions in the context of tensor network states. The distinct features of the phase transitions illustrated by these numerical probes are used to characterize the order of phase transitions. Along with the description of different numerical methods, we also study the phase transitions between $\mathbb{Z}_4 \boxtimes \mathbb{Z}_2$ DS $\leftrightarrow$ $\mathbb{Z}_4 \boxtimes \mathbb{Z}_2$ TC and $D(\mathbb{Z}_4)$ QD $\leftrightarrow$ $\mathbb{Z}_4 \boxtimes \mathbb{Z}_2$ TC. Both of these phase transitions are governed by linear interpolation of the on-site transfer operators as explained in Sec. 4.3.2. From different numerical insights, we identify the order of the phase transitions between DS and TC, and between $D(\mathbb{Z}_4)$ QD and TC to be first- and second-order respectively.

4.4.1 Order parameters

Order parameters are some of the fundamental objects that characterize the behavior of phase transitions. It is not clear how to generalize the idea of order parameters in the case of topologically non-trivial systems. It turns out that different condensation/de-condensation and confinement/deconfinement fractions have a natural interpretation of order parameters in the case of topological (trivial/non-trivial) phases. In analogy with conventional order parameters, they enable us not only to distinguish different topological (trivial/non-trivial) phases, the critical behavior of these fractions can be used to extract the universal properties of topological phase transitions. In the following, we will show a method for the computation of these fractions and determine their behavior for the two phase transitions mentioned above.

Computation of order parameter

As explained in Sec. 4.1.4, every possible fraction can be summarized by the wavefunctions overlap $\langle g, \alpha | g', \alpha' \rangle$. Fig. 4.9a graphically shows an overlap of 2D wavefunctions on an infinite plane and the endpoints of string actions which act on the virtual indices are located at the same position. The overlap can be written as,

$$\langle g', \alpha' | g, \alpha \rangle = \frac{\langle \psi[A] | [\![g', \alpha']\!] \otimes [\![g, \alpha]\!] | \psi[A] \rangle}{\langle \psi[A] | \psi[A] \rangle}. \tag{4.45}$$

where as defined earlier $[\![g, \alpha]\!] := (...X_g X_g Z_\alpha)$ and $[\![g', \alpha']\!] := (...X_{g'} X_{g'} Z_{\alpha'})$ are the semi-infinite string operators and they create excitations in the ket and bra layer of the tensor network.

To compute the overlap, we proceed by first reducing a 2D overlap into a 1D object by approximating the left and right fixed points of the transfer operator as illustrated in Fig. 4.9(a,b). This step also highlights a relation between overlaps of anyonic excitations in 2D and the expectation value of string-order parameters in the boundary phase as explained earlier (see Sec. 4.1.5). The dimensional reduction from a 2D to a 1D object is possible due to an underlying assumption that the fixed points of the transfer operator can be approximated by an MPS with finite bond dimension χ. The computation of the fixed points of the transfer operator in the thermodynamic limit ($N_h, N_v \to \infty$) is enabled by an infinite matrix product state (iMPS) algorithm (see Sec. 3.2.5). Let $(l|$ and $|r)$ be the left and the right fixed points of the transfer operator $\mathbb{T}$ then the overlap can be approximated as,

$$\langle g', \alpha' | g, \alpha \rangle \approx \frac{(l | [\![g', \alpha']\!] \otimes [\![g, \alpha]\!] | r)}{(l|r)}, \tag{4.46}$$

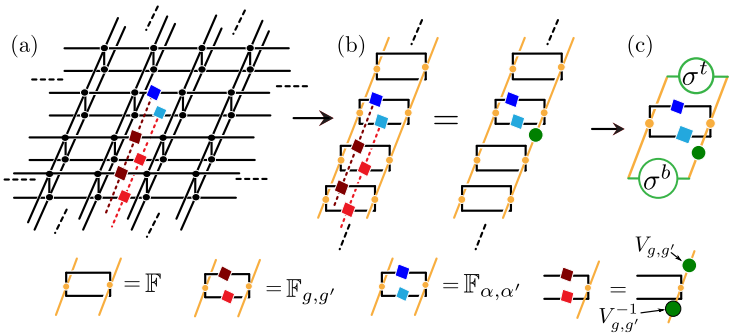

FIGURE 4.9: Arrows show the steps followed for the computation of a fraction $\langle g', \alpha' | g, \alpha \rangle$. (a) Light(dark) red string with light(dark) blue ends acting on the virtual indices in the bra(ket) layer creates an excitation. (b) Yellow lines indicate the left $(l|$ and right $|r)$ fixed point of the transfer operator. Last equation in the row at the bottom shows the translation of symmetry action from the physical to the virtual indices of local tensors. (c) σ^t and σ^b represent the fixed points of channel operator from the top and bottom respectively.

where $(l|$ and $|r)$ are the left and right fixed points of the transfer operator $\mathbb{T}$.

After computing the right and left fixed points of the transfer operator, the computation of string-order parameter (corresponding to given 2D wavefunction overlap) is completed by another dimension reduction. The object formed by contracting the right $|r)$ and left $(l|$ fixed points of the transfer operator with semi-infinite string action (which acts both on the bra and ket indices) between the two fixed points can be decomposed in terms of the *boundary transfer operators* (also called the *channel operators*), as indicated in Fig. 4.9b. $\mathbb{F}$ is obtained by contracting the 'physical' indices of $(l|$ and $|r)$ local tensors. $\mathbb{F}_{g,g'}$ denotes the dressed channel operator with an additional string action. If (g, g') is the symmetry of the fixed points (i.e., the fixed points remain invariant under the action of the form $(..X_g X_g..) \otimes (..X_{g'} X_{g'}..)$ on their physical indices) then symmetry action (g, g') on the local tensors of the fixed points can be moved to the virtual indices (Fig. 4.9).

Now, we compute the largest eigenvectors σ^b and σ^t of the channel operator $\mathbb{F}$ from the bottom and top respectively. The eigenvectors can be computed by exact diagonalization even for very large χ. Finally, the expectation value is computed by acting on $\mathbb{F}_{\alpha,\alpha'}$ with σ^t and σ^b with virtual symmetry action $V_{g,g'}$ as shown in Fig. 4.9c.

$$\langle g', \alpha' | g, \alpha \rangle \approx \frac{\left(\sigma^t \middle| \mathbb{F}^{(\alpha,\alpha')} (\mathbb{I} \otimes V_{g,g'}) \middle| \sigma^b\right)}{(\sigma^t | \mathbb{F} | \sigma^b)}. \tag{4.47}$$

The procedure we have described here for computing wavefunctions overlap works directly in the thermodynamic limit, and the most expensive step of the computation lies in finding the fixed points of the transfer operator.

Here we point out an observation which is important for the numerical computation of fractions, specially in the context of DS model. It turns out that the tensor $\mathbb{F}_{\alpha,\alpha'}$ with

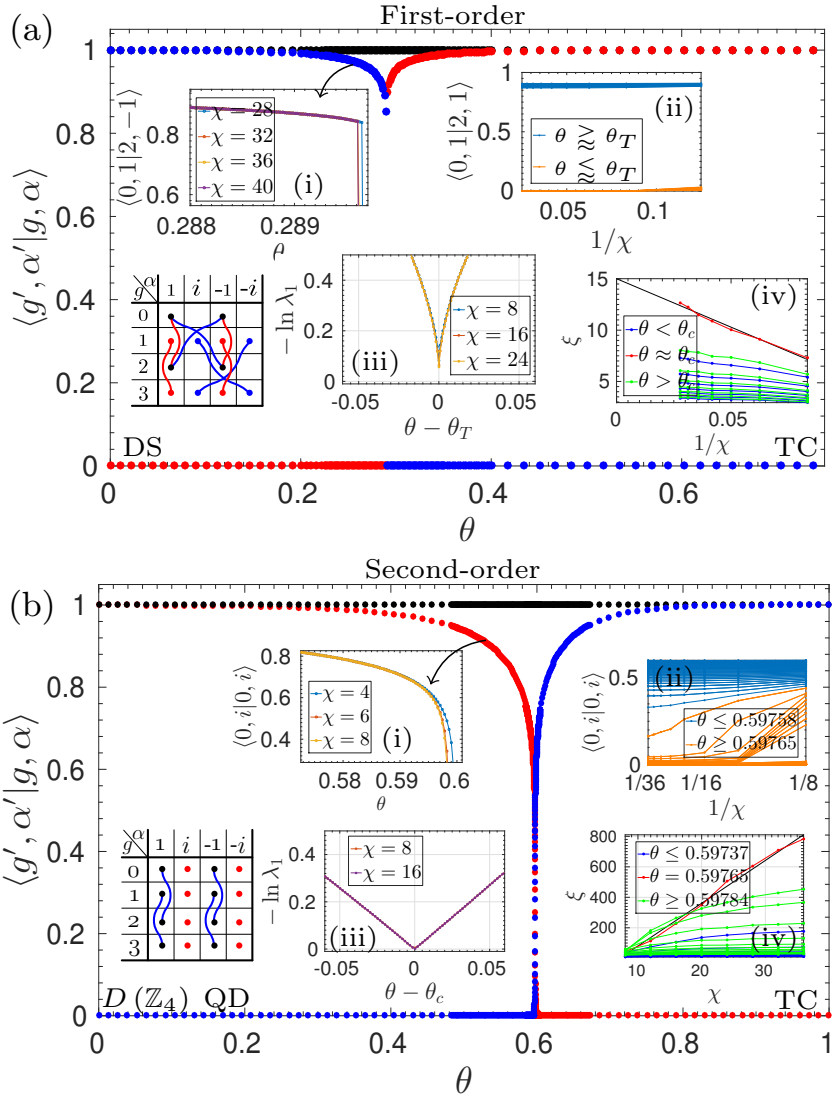

FIGURE 4.10: Phase transitions between (a) $\mathbb{Z}_4 \boxtimes \mathbb{Z}_2$ DS and $\mathbb{Z}_4 \boxtimes \mathbb{Z}_2$ TC, and between (b) $D(\mathbb{Z}_4)$ QD and $\mathbb{Z}_4 \boxtimes \mathbb{Z}_2$ TC. See text for the description of color legends defined by anyon tables. Inset (i) in (a) and (b) shows the magnified view of overlap in the vicinity of phase transitions and its scaling with increasing χ. The inset (ii) in (a) and (b) shows the scaling of order parameter (i.e., $\langle 0,1|2,1\rangle$ in (a) and $\langle 0,i|0,i\rangle$ in (b)) in the critical regime. The inset (iii) in (a) and (b) shows the first excited state of the transfer operator or inverse of correlation length computed by using the excitation ansatz. (a,b)iv shows the scaling of correlation length with different χ computed by using the channel operator.

non-trivial (α, α') is not always symmetric (i.e. $\mathbb{F}_{\alpha,\alpha'} \neq \mathbb{F}^T_{\alpha,\alpha'}$) at least in the case of $\mathbb{Z}_4 \boxtimes \mathbb{Z}_2$ DS model. It is consequential whether one puts the string $\left(...X^g X^g, ...X^{g'} X^{g'}\right)$ on the left or right of $\mathbb{F}_{\alpha,\alpha'}$ for the computation of a fraction. One approach to compensate for this effect is to compute the fraction by inserting the string on both sides of $\mathbb{F}_{\alpha,\alpha'}$.

A comparative study of order parameter

After having described the numerical method for the computation of fractions, in the following we use these methods to study the behavior of fractions for $\mathbb{Z}_4 \boxtimes \mathbb{Z}_2$ DS $\leftrightarrow$ $\mathbb{Z}_4 \boxtimes \mathbb{Z}_2$ TC and $D(\mathbb{Z}_4)$ QD $\leftrightarrow$ $\mathbb{Z}_4 \boxtimes \mathbb{Z}_2$ TC phase transitions. Since g and α can each take four possible values, $\binom{16+2-1}{2} = 136$ combinations are sufficient to describe every overlap and are shown in Fig. 4.10(a,b) for the two phase transitions. Legend of the overlaps in (a) and (b) is defined by the anyon tables at the lower left corners. The color of the solid dot in an entry of the anyon table represents the norm $\langle g, \alpha | g, \alpha \rangle$. The color of an edge between two entries represents overlaps of the form $\langle g, \alpha | g', \alpha' \rangle$, where $g \neq g'$ and $\alpha \neq \alpha'$. The absence of a dot in an entry or an edge between two entries denotes overlaps which remain zero along the whole interpolation.

Different fractions in the vicinity of phase transition show a characteristically different behavior for the two phase transitions. We use this qualitative difference to infer the order of phase transitions. In the case of the phase transition between $\mathbb{Z}_4 \boxtimes \mathbb{Z}_2$ DS and $\mathbb{Z}_4 \boxtimes \mathbb{Z}_2$ TC, we observe a discontinuity, whereas in the case of the phase transition between $D(\mathbb{Z}_4)$ QD and $\mathbb{Z}_4 \boxtimes \mathbb{Z}_2$ TC different fractions smoothly decay to zero. Fig. 4.10a(i) shows the magnified view of $\langle 0, 1 | 2, -1 \rangle$ with different bond dimensions. It instantaneously drops to zero at the transition point, and the behavior is independent of the resolution of data points. The behavior of $\langle 0, 1 | 2, -1 \rangle$ at the transition point suggests a first-order phase transition. Fig. 4.10b(i) shows a qualitatively different behavior of a confinement fraction $\langle 0, i | 0, i \rangle$ where it smoothly decays to zero, which indicates a second-order phase transition.

Discontinuity is also manifested in the error scaling of order parameter for the first-order phase transition. There is a gap in the value of condensate fraction $\langle 0, 1 | 2, 1 \rangle$ as shown in Fig. 4.10a(ii). The gap does not get narrower with increasing bond dimension even with a high density of data points. The jump in Fig. 4.10a(i,ii) can be used to get an estimated value of transition point which is $\theta_T = 0.2896(5)$. Unlike first-order, for the case of second-order phase transition in Fig. 4.10b(ii), we observe that the error in the value order parameter decays exponentially with increasing χ away from the critical point. On the other hand, as one approach close enough to the critical point, the scaling of the error is polynomial. The numerical value of the critical point can be obtained by distinguishing the two behaviors, and it is $\theta_c = 0.5976(2)$.

Furthermore, if the phase transition is second-order, we can compute the critical exponents β and γ by studying the scaling of fractions and the susceptibilities of the fractions in the critical regime.

4.4.2 Correlation lengths

Correlation length ξ is another important quantity which can be used to extract the universal features of phase transition.

Computation of correlation length

Now, to compute the correlation length, we can use the transfer operator of 2D tensor network state (Fig. 4.1e). However, the calculation of gap above the ground state subspace of the transfer operator is a computationally intensive problem, but there are three methods.

1. We can use the channel operator which acts as the transfer matrix of boundary phase (Fig. 4.9b) for the computation of correlation length (i.e., $\xi = -1/\ln|\lambda_1/\lambda_0|$, where λ_0 and λ_1 are the first and second largest eigenvalues of the channel operator). Channel operator is constructed from the fixed points of the 2D transfer matrix and is a finite object; the gap can be computed efficiently. However, this approach is restricted as it does not take into account all the two point correlations.

2. The second possibility is to compute the gap of the transfer operator using the excitation ansatz as proposed in [50, 55, 68]. Using excitation ansatz, we can construct topological (trivial/non-trivial) excitations, and it is possible to work directly in the thermodynamic limit.

3. The third possibility is to proceed by exact diagonalization on an infinite cylinder ($N_h \to \infty$) with finite perimeter N_v to compute the gap and then by extrapolation in N_v we can get a reliable estimate of ξ. It is important to point out here that the exact diagonalization should be performed on the 'complete' transfer matrix (i.e., the one which include all topological sectors and obtained by inserting every possible flux in the bra and ket layer) [44]. Given a spectrum of the transfer matrix, correlation length ξ can be computed from the gap below the largest eigenvalue sectors, e.g., in the case of $\mathbb{Z}_4$-invariant tensors the dimension of the largest eigenvector (ground state) manifold is 4×4, so $\xi = -1/\ln|\lambda_{16}/\lambda_0|$.

The behavior of the correlation length computed by the above three methods for the phase transition between $D(\mathbb{Z}_4)$ QD and $\mathbb{Z}_4 \boxtimes \mathbb{Z}_2$ TC is shown in Fig. 4.11. Away from the critical point the resulting correlation length ξ computed by different methods conform with each other (Fig. 4.11a). Fig. 4.11b) shows the divergence of ξ with increasing bond dimension computed by using the iMPS algorithm. The scaling of

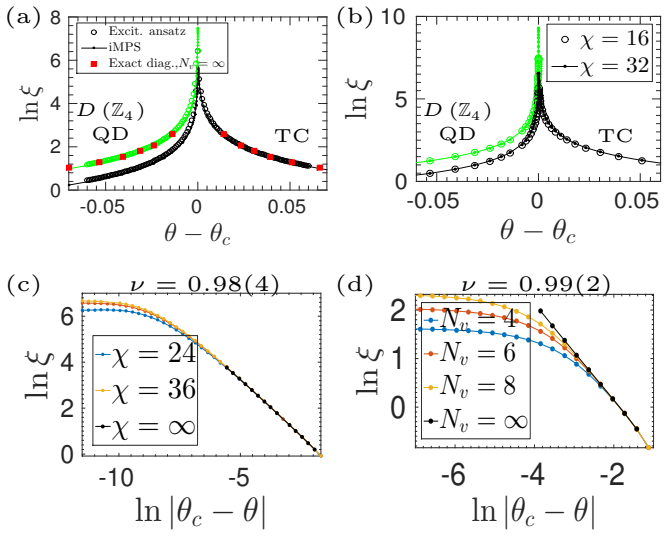

FIGURE 4.11: (a) Correlation length computed by using three numerical methods. (b) The behavior of correlation length computed by using iMPS algorithm for different bond dimensions χ. Green data points in (a,b) indicate correlation length corresponding to the broken symmetry domain wall excitations. (c,d) shows the critical exponent ν of the correlation length ξ which has been obtained by extrapolation in the bond dimension χ by $a\exp(-b\chi)+\xi_\infty$, and by extrapolation in the perimeter N_v by $a\exp(-bN_v)+\xi_\infty$.

correlation length in the critical regime can be used to extract the critical exponent ν (Fig. 4.11(c,d))).

A comparative study of correlation lengths

Now we analyze distinct features of the correlation length for the 1st (i.e., between DS and TC) and 2nd (i.e., between $D(\mathbb{Z}_4)$ QD and TC) order phase transitions. Fig. 4.10a(iii) shows the correlation length which have been computed by using the excitation ansatz for the transfer operators for $\chi = (8, 16, 24)$. By rescaling the transfer operator (i.e., the largest eigenvalue $\lambda_0 = 1$), we can write the inverse of correlation length as $\xi^{-1} = \ln\lambda_1$. As the system approaches the transition point, the correlation length increases but it remain finite, and there exists a finite gap which indicates first-order phase transition. Furthermore, the correlation length computed by using channel operators also have a finite value in the case of first-order phase transition as indicated by the linear fit in $1/\chi$ (black line) in Fig. 4.10a(iv).

In contrast to the finite gap at the transition point in the case of $\mathbb{Z}_4 \boxtimes \mathbb{Z}_2$ DS $\leftrightarrow$ $\mathbb{Z}_4 \boxtimes \mathbb{Z}_2$ phase transition, the gap closes and correlation length diverges at the critical point for $D(\mathbb{Z}_4)$ QD $\leftrightarrow$ $\mathbb{Z}_4 \boxtimes \mathbb{Z}_2$ TC case which is a further evidence for second-order phase transition (Fig. 4.10b(iii)). Fig. 4.10b(iv) shows diverging correlation length at the critical point with increasing χ.

4.4.3 Fidelity per site and fidelity susceptibility

The notion of fidelity per site has been studied in the context of tensor network states in [69]. It gives a measure of distinguishably between quantum states, and it is defined as the normalized overlap of two wavefunctions per site. The method for the computation of fidelity per site is described in the previous chapter. Furthermore, *fidelity susceptibility* χ_F which quantifies the fidelity response against an infinitesimal change in tuning variable also exhibits universal features which can be used to characterize phase transitions [49].

Fidelity per site can be used to characterize the behavior of phase transitions. Fig. 4.12(a,b) show a comparison of fidelity per site for (a) first- and (b) second-order phase transition. Fig. 4.12(c,d) shows the behavior of fidelity per site across different slices marked in the surface plot Fig. 4.12(a,b). Although $f(\theta_1, \theta_2)$ changes smoothly in the first-order case, we observe a cusp-like behavior in the transition regime which is qualitatively different in comparison to the second order phase transition between the $D(\mathbb{Z}_4)$ QD and $\mathbb{Z}_4 \boxtimes \mathbb{Z}_2$ TC.

Fidelity susceptibility χ_F also exhibits distinct features in the case of first- and second-order phase transition. In the case of phase transition between $\mathbb{Z}_4 \boxtimes \mathbb{Z}_2$ DS and $\mathbb{Z}_4 \boxtimes \mathbb{Z}_2$ TC, χ_F diverges to the delta function as the system approaches transition point. Delta divergence of χ_F can be shown by the collapse of rescaled susceptibility curves (i.e., $\delta.\chi_F$) when viewed as a function of $(\theta - \theta_c)/\delta$ (Fig. 4.12e). Moreover, the scaling of χ_F in the vicinity of phase transition cannot be explained by the power law as the critical exponent is undefined and this behavior is characteristic of a first-order phase transition. Fig. 4.12f shows the behavior of χ_F in the thermodynamic limit with different step sizes δ for the phase transition between $D(\mathbb{Z}_4)$ QD and $\mathbb{Z}_4 \boxtimes \mathbb{Z}_2$ TC. χ_F diverges at the critical point as δ approaches 0. The scaling of χ_F in the critical regime observes a power law behavior which suggests a second-order phase transition.

Another distinct feature is the scaling of χ_F with $1/\delta^m$ in the vicinity of phase transition for the first-order case. In contrast, for the second-order case we observe the scaling of χ_F with $\ln(1/\delta^m)$ (see insets of Fig. 4.12(e,f)).

4.5 Phase diagram of $\mathbb{Z}_4$-invariant tensors

In the previous section, we described different numerical methods and presented our findings regarding the two phase transitions. Here we will systematically explore the whole phase diagram of $\mathbb{Z}_4$-invariant tensor network states using those numerical tools.

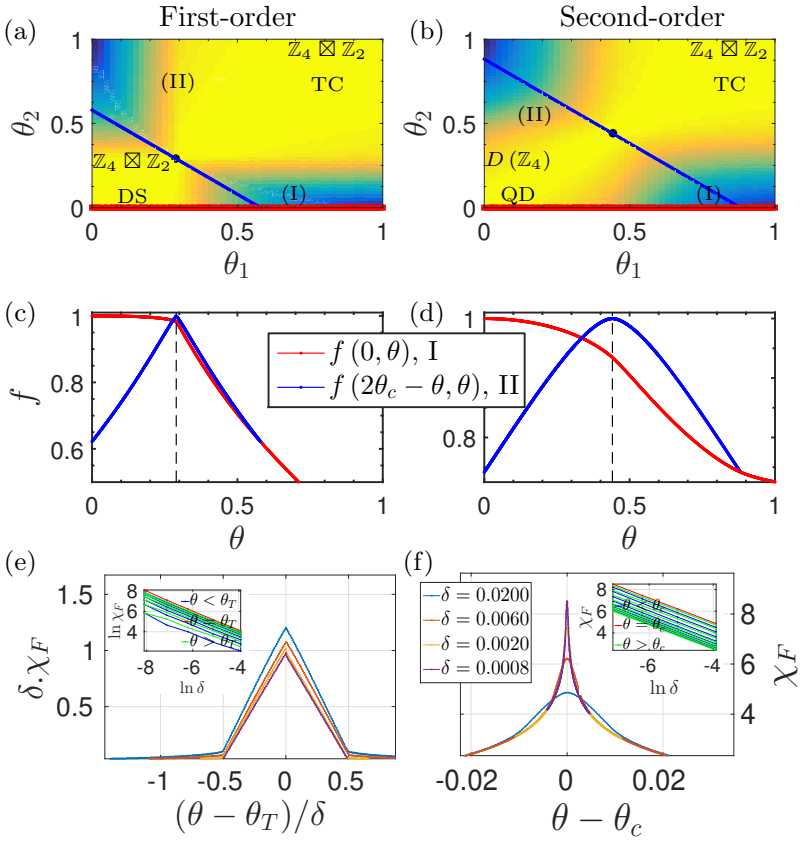

FIGURE 4.12: Comparison of fidelity per site for the first order phase transition between $\mathbb{Z}_4 \boxtimes \mathbb{Z}_2$ DS and $\mathbb{Z}_4 \boxtimes \mathbb{Z}_2$ TC (a,c) and the second order phase transition by $D(\mathbb{Z}_4)$ QD and $\mathbb{Z}_4 \boxtimes \mathbb{Z}_2$ TC (b,d). Fidelity susceptibility for the (e) first- and (f) second-order phase transition computed using iMPS algorithm with $\chi = 32$. (e) and (f) share the same legend. Inset of (e) shows χ_F as a function of δ on a log-log plot, the value of slope $m \sim 1.57$. Inset of (f) shows the linear scaling of χ_F for $\ln \delta$. The value of slope $m \sim 1.14$.

We defined different deformations in the Sec. 4.3 which when applied on $D(\mathbb{Z}_4)$ QD can realize different topologically trivial and non-trivial phases. We can also compose these deformations in order get a richer variety of phase transitions. Here we map out the phase diagram of $\mathbb{Z}_4$-invariant tensors using the deformation constructed in (4.38). Later, in the following subsections, we will dissect the whole phase diagram and discuss in greater detail the distinct features of particular phase transitions.

The deformation described in (4.38) is parametrized by $\boldsymbol{\theta} = (\theta_{\text{TC}}, \theta_{\text{TC},Z_2}, \theta_{\text{DS}})$. The state corresponding to each $\boldsymbol{\theta}$ can be assigned a phase (topologically trivial/non-trivial) by probing different fractions. The essential features of the whole phase diagram can be captured by computing the distribution of different phases on the three hyperplanes (Fig. 4.13). We use the iMPS algorithm for the computation of various fractions. The deformation induces two toric codes ($\mathbb{Z}_4 \boxtimes \mathbb{Z}_2$ TC and $\mathbb{Z}_2 \boxtimes \mathbb{Z}_1$ TC), a DS model with $\mathbb{Z}_4 \boxtimes \mathbb{Z}_2$ symmetry and $\mathbb{Z}_2 \boxtimes \mathbb{Z}_2$ TP when applied on $D(\mathbb{Z}_4)$ QD.

Although the set is not unique, for illustrative purposes, we choose three fractions $\mathcal{C} = \{\langle 2,1|0,-1\rangle,\ \langle 1,i|1,i\rangle, \langle 0,i|0,-i\rangle\}$, whose values are sufficient to visualize every phase which can be realized by deformation. In the following, we will explain the appearance of different phases in Fig. 4.13.

1. In $D(\mathbb{Z}_4)$ QD, none of the possible anyons are condensed or confined, which means that the only fraction from $\mathcal{C}$ with a non-zero value is $\langle 1,i|1,i\rangle$. So the green region in the phase diagram is identified with $D(\mathbb{Z}_4)$ QD.

2. In the case of $\mathbb{Z}_4 \boxtimes \mathbb{Z}_2$ TC, all the anyons of form $|*,\pm i\rangle$ are confined, which implies that the overlaps $\langle 1,i|1,i\rangle$ and $\langle 0,i|0,-i\rangle$ are equal to zero. Furthermore, the anyon $|2,1\rangle$ is condensed to the vacuum but it can be distinguished from the anyon $|0,-1\rangle$. Since every fraction in $\mathcal{C}$ is zero for $\mathbb{Z}_4 \boxtimes \mathbb{Z}_2$ TC phase, every point in the black region corresponds to $\mathbb{Z}_4 \boxtimes \mathbb{Z}_2$ TC.

3. In $\mathbb{Z}_2 \boxtimes \mathbb{Z}_1$ TC phase, anyons of the form $|1,*\rangle$ and $|3,*\rangle$ are confined. Anyons $|2,1\rangle$ and $|0,-1\rangle$ are not confined but they can be distinguished from each other. The only fraction in $\mathcal{C}$ with a non-zero value is $\langle 0,i|0,-i\rangle$ which explains the blue color for $\mathbb{Z}_2 \boxtimes \mathbb{Z}_1$ TC.

4. Anyons $|0,\pm i\rangle$ are confined in $\mathbb{Z}_4 \boxtimes \mathbb{Z}_2$ DS phase which implies that the overlap $\langle 0,i|0,-i\rangle$ is zero. On the other hand, the anyon $|1,i\rangle$ is deconfined and the anyons $|2,1\rangle$ and $|0,-1\rangle$ are mutually indistinguishable (i.e. $\langle 2,1|0,-1\rangle = 1$). The fractions in $\mathcal{C}$ with non-zero value are $\langle 0,i|0,i\rangle$ (green) and $\langle 2,1|0,-1\rangle$ (red). Sum of red and green produces yellow, so the $\mathbb{Z}_4 \boxtimes \mathbb{Z}_2$ DS phase is identified with yellow region.

5. In the case of $\mathbb{Z}_2 \boxtimes \mathbb{Z}_2$ TP the only non-zero fraction from $\mathcal{C}$ with a non-zero value is $\langle 2,1|0,-1\rangle$ which determines the color of $\mathbb{Z}_2 \boxtimes \mathbb{Z}_2$ TP phase to be red.

4.5.1 Phase transitions from $D(\mathbb{Z}_4)$ quantum double to topological phases

First, we study the phase transitions between $D(\mathbb{Z}_4)$ QD and topologically non-trivial phases which include the two toric codes and a double semion model.

$D(\mathbb{Z}_4)$ QD and $\mathbb{Z}_4 \boxtimes \mathbb{Z}_2$ TC

Phase transitions between $D(\mathbb{Z}_4)$ QD and $\mathbb{Z}_4 \boxtimes \mathbb{Z}_2$ TC can be governed either by local filtering or by linear interpolation as described in (4.34) and (4.44) respectively. Results

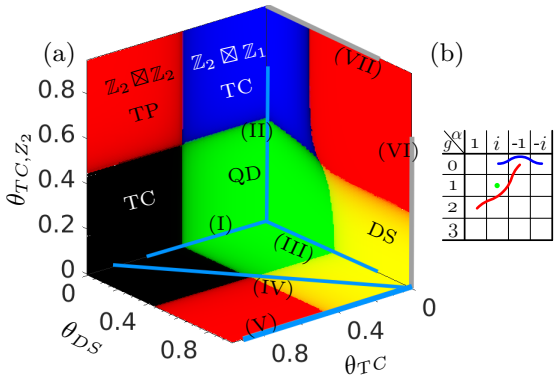

FIGURE 4.13: (a) Phase diagram of $\mathbb{Z}_4$-invariant tensor network states. The RGB (red, green, and blue) components of color at each point on the three hyperplanes is identified with the fractions indicated in the anyon table in (b). $\chi = 16$ has been used for the approximation of fixed points in the iMPS calculations.

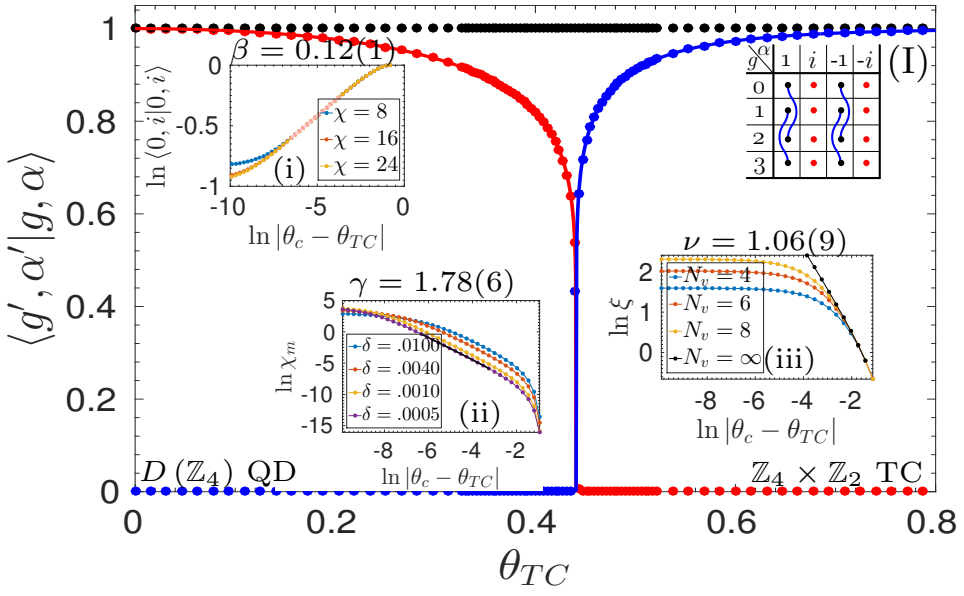

FIGURE 4.14: Phase transition between $D(\mathbb{Z}_4)$ QD and $\mathbb{Z}_4 \boxtimes \mathbb{Z}_2$ TC driven by local filtering with the bond dimension $\chi = 24$. Anyon table at the top right corner defines the color of fractions as explained earlier in Fig. 4.10. (i) The behavior of a confinement fraction in the critical regime. (ii) Critical exponent γ is obtained from the scaling of confinement susceptibility in the critical regime. δ denotes the different step-sizes used for the computation of derivative. (iii) Correlation length ξ and the critical exponent ν which is obtained by an extrapolation of ξ in N_v by $a \exp(-bN_v) + C_\infty$.

regarding the phase transition between $D(\mathbb{Z}_4)$ QD and $\mathbb{Z}_4 \boxtimes \mathbb{Z}_4$ TC via linear interpolation have already been presented earlier (Fig. 4.10b). Here we discuss the phase transition which is governed by local filtering along the path labeled by (I) in Fig. 4.13a.

We look at different fractions as a function of tuning variable θ_{TC} between the two phases. As one moves from $D(\mathbb{Z}_4)$ QD towards the transition point one sees the confinement of anyons $|*, \pm i\rangle$, i.e. for $\theta_{\text{TC}} \geq \theta_c = \frac{1}{2}\ln\left(1+\sqrt{2}\right)$, the vacuum does not support the

existence of these anyons. After the transition point, the fixed points of the transfer operator acquire $\mathbb{Z}_4 \boxtimes \mathbb{Z}_2$ symmetry which leads to the condensation of anyon $|2,1\rangle$ to the anyonic vacuum $|0,1\rangle$.

Fig. 4.14 shows overlaps for the phase transition obtained via local filtering. Red (blue) curves represent the confinement (condensation) fractions. Solid dots denote the numerical values whereas the solid lines represent the analytic results. It turns out that the confinement (red) and condensation (blue) fractions are related, as they correspond to the order parameters of self-dual models, one at low- and the other corresponding to high-θ. We use this duality to derive the closed form of these fractions (see Sec. 4.5.2).

The nature of phase transition can be determined from the scaling of 'order parameter' (which in this case can be $\langle 0,i|0,i\rangle$ or $\langle 0,1|0,2\rangle$). Critical exponent $\beta \sim 1/8$ as shown in Fig. 4.14(i), is obtained from the slope of an order parameter on log-log plot. We introduced an external field as a function of tuning variable h in Sec. 4.3.1. The susceptibility of order parameter (e.g. $\langle 0,i|0,i\rangle$) against the external field can be defined as

$$\chi_m(\theta) := \left.\frac{\partial\langle 0,i|0,i\rangle}{\partial h}\right|_{h=0} \tag{4.48}$$

where $|0,i\rangle$ is a function of θ and h. We examine the behavior of χ_m by calculating the derivative of $\langle 0,i|0,i\rangle$ with respect to h using finite difference method for different step sizes δ. The scaling of χ_m with respect to θ in the critical regime gives the critical exponent $\gamma \sim 7/4$ (Fig. 4.14(ii)). We also observe similar scaling behavior for the susceptibility of $\langle 0,1|2,1\rangle$. We calculate correlation length ξ on an infinite cylinder with finite perimeter using the method described in Sec. 4.4.2. The critical exponent ν has been calculated from scaling of ξ with θ in the critical regime. From the slope of extrapolated ξ on a log-log plot, we get $\nu \sim 1$ (Fig. 4.14(iii)).

Values of critical exponents characterize the phase transition in the Ising universality class. In fact, the relation is stronger. The phase transition can be mapped to the 2D classical Ising model, i.e., $D(\mathbb{Z}_4)$ QD and $\mathbb{Z}_4 \boxtimes \mathbb{Z}_2$ TC can be identified with the symmetry broken and disordered phases of Ising model respectively. This relation holds because of equivalence between the partition function of Ising model and the norm of the vacuum state which is described in (4.34).

$$\begin{array}{c}\text{Partition function of 2D}\\ \text{classical Ising model}\end{array} \quad \longleftrightarrow \quad \begin{array}{c}\text{Norm of}\\ \text{vacuum}\end{array} \tag{4.49}$$

Additionally, the anyonic excitations of quantum doubles can be mapped to the topological defects in Ising model [70]. A detailed account of this mapping is given in Sec. 4.5.2.

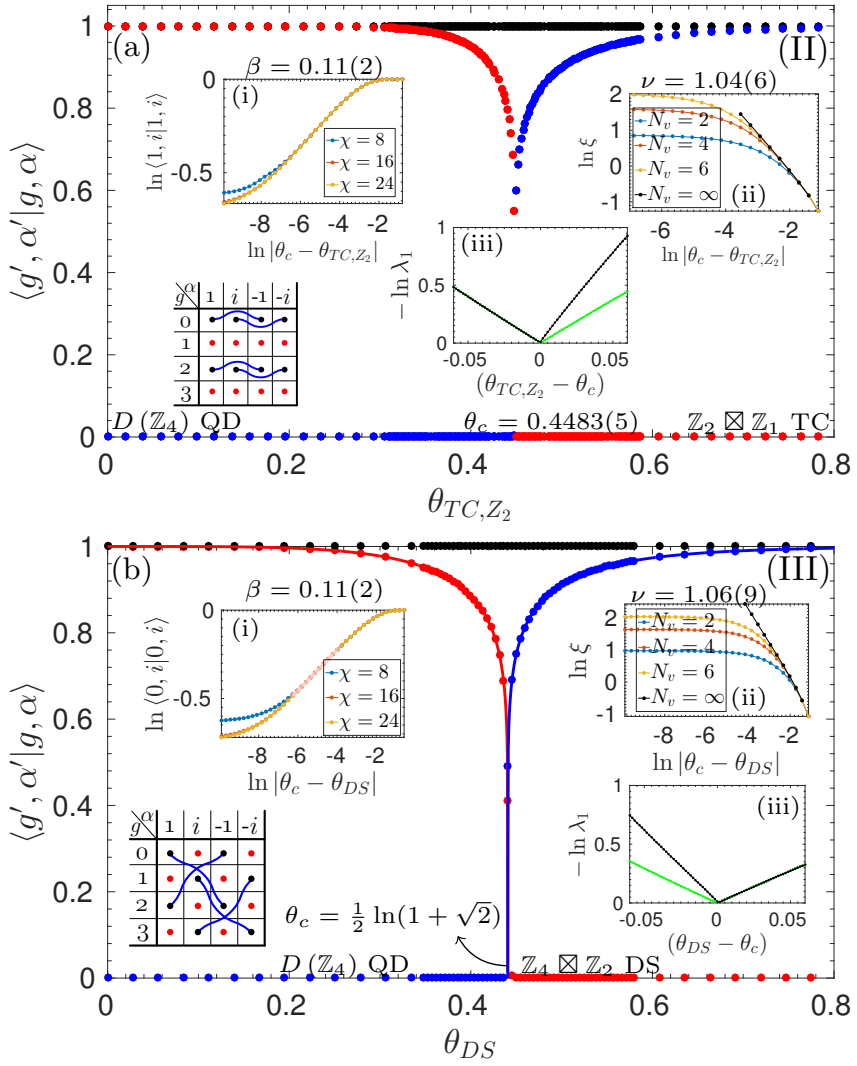

FIGURE 4.15: Phase transitions (a) $D(\mathbb{Z}_4)$ QD $\leftrightarrow$ $\mathbb{Z}_2 \boxtimes \mathbb{Z}_1$ TC and (b) $D(\mathbb{Z}_4)$ QD $\leftrightarrow$ $\mathbb{Z}_4 \boxtimes \mathbb{Z}_2$ DS. Anyon tables at the lower corners in (a) and (b) define the color of fractions as explained earlier for Fig. 4.10. Insets (i) and (ii) in (a) and (b) shows the critical exponents β and ν of an order parameter and correlation length respectively. Inset (iii) in (a) and (b) shows the scaling of first-excited state of transfer operator in the vicinity of phase transition.

The critical exponents of the phase transition between $D(\mathbb{Z}_4)$ QD and $\mathbb{Z}_4 \boxtimes \mathbb{Z}_2$ TC which is prescribed by the linear interpolation of the on-site transfer operators (see (4.44)) also classify the phase transition in the Ising universality class. These two observations suggest that the nature of phase transition between $D(\mathbb{Z}_4)$ QD and $\mathbb{Z}_4 \boxtimes \mathbb{Z}_2$ TC is independent of the path one chooses provided that the path respects the $\mathbb{Z}_4$-invariance of local tensor and it is a second-order phase transition which lies in the Ising universality class.

$D(\mathbb{Z}_4)$ QD and $\mathbb{Z}_2 \boxtimes \mathbb{Z}_1$ TC

We now describe the phase transition between $D(\mathbb{Z}_4)$ QD and $\mathbb{Z}_2 \boxtimes \mathbb{Z}_1$ TC as explained in (4.36) and labeled as (II) in Fig. 4.13a. Although the anyons in $\mathbb{Z}_4 \boxtimes \mathbb{Z}_2$ TC and $\mathbb{Z}_2 \boxtimes \mathbb{Z}_1$ TC have the same self and mutual statistics, they have different realizations. The system undergoes a phase transition from $D(\mathbb{Z}_4)$ QD to $\mathbb{Z}_2 \boxtimes \mathbb{Z}_1$ TC phase as we increase θ_{TC,Z_2}. As the critical point is approached the anyons $\{|1,*\rangle, |3,*\rangle\}$ get confined, and their confinement fractions vanish completely at the critical point. Fixed points of the transfer operator spontaneously break the $\mathbb{Z}_4 \boxtimes \mathbb{Z}_1$ symmetry to $\mathbb{Z}_2 \boxtimes \mathbb{Z}_1$. After the phase transition the anyon $|0,-1\rangle$ gets condensed to the vacuum. Overlaps $\langle 0,i|0,-i\rangle$, $\langle 2,1|2,-1\rangle$, and $\langle 2,i|2,-i\rangle$ become 1 and deep in the $\mathbb{Z}_4 \boxtimes \mathbb{Z}_2$ TC phase one could have only four distinguishable anyons.

Overlaps which summarize all condensation and confinement fractions for the phase transition between $D(\mathbb{Z}_4)$ QD and $\mathbb{Z}_2 \boxtimes \mathbb{Z}_1$ TC are shown in Fig. 4.15a. Initial numerical findings suggest a continuous phase transition which occurs at $\theta_c = 0.4483(5)$. The scaling of the order parameter ($\langle 1,i|1,i\rangle$ or $\langle 0,1|0,-1\rangle$) gives a critical exponent $\beta \sim 1/8$ as shown in Fig. 4.15a(i). We find the critical exponent of correlation length to be $\nu \sim 1$ (Fig. 4.15a(ii,iii)). Green lines in Fig. 4.15a(iii) represent topological excitations of the transfer operator with domain walls which are constructed by the broken symmetry actions. These excitations determine the critical behavior and decisively close the gap at the critical point. Again, the linear behavior of ξ^{-1} in Fig. 4.15a(iii) is a manifestation of the fact that $\nu \sim 1$. Furthermore, the phase transition between $D(\mathbb{Z}_4)$ QD and $\mathbb{Z}_2 \boxtimes \mathbb{Z}_1$ TC which is governed by linear interpolation of the on-site transfer operators also lies in the Ising universality class.

It is possible to map the phase transition between $D(\mathbb{Z}_4)$ QD and $\mathbb{Z}_2 \boxtimes \mathbb{Z}_1$ TC to the 2D Ising model by explicitly breaking the symmetry. This can be achieved by inserting a projector $|0\rangle\langle 0|$ in the blue ring in (4.36). Although the insertion would preserve the $\mathbb{Z}_4 \boxtimes \mathbb{Z}_4$ symmetry of the transfer operator, the action would restrict symmetry broken fixed points of the transfer operator from eight to four and the projector of $\mathbb{Z}_2 \boxtimes \mathbb{Z}_1$ TC no longer commutes with the on-site tensor (black ring) of $D(\mathbb{Z}_4)$ QD.

$D(\mathbb{Z}_4)$ QD and $\mathbb{Z}_4 \boxtimes \mathbb{Z}_2$ DS

Another interesting case is the phase transition between $D(\mathbb{Z}_4)$ QD and $\mathbb{Z}_4 \boxtimes \mathbb{Z}_2$ DS model via the path defined in (4.37) and which is labeled as (III) in Fig. 4.13a. The phase transition occurs at $\theta_c = \frac{1}{2}\ln\left(1+\sqrt{2}\right)$. The critical behavior is governed by vanishing confinement fractions of anyons $\{|0,\pm i\rangle, |1,\pm 1\rangle, |2,\pm i\rangle, |3,\pm 1\rangle\}$ and by the condensation of $|2,-1\rangle$ to the vacuum.

The numerical values of condensation and confinement fractions are shown in Fig. 4.15b. Just like the case of $\mathbb{Z}_4 \boxtimes \mathbb{Z}_2$ TC, the phase transition between $D(\mathbb{Z}_4)$ QD and $\mathbb{Z}_4 \boxtimes \mathbb{Z}_2$ DS can be mapped to the 2D Ising model (see Sec 4.5.2) and one can use this mapping to extract the closed form of different fractions. Analytic results are represented by solid lines in Fig. 4.15b. Not surprising but as an evidence of validity, the numerical findings of the critical exponent β in Fig. 4.15b(i) and ν in Fig. 4.15b(ii,iii) also identify the phase transition with the Ising universality class.

4.5.2 Ising model and topological phase transitions

Now we discuss a mapping between the partition function of classical Ising model and the norm of vacuum state which is parametrized by the tuning variable θ. We will focus our attention here on the phase transition between $D(\mathbb{Z}_4)$ QD and $\mathbb{Z}_4 \boxtimes \mathbb{Z}_2$ TC, but the description is generic enough to be applied in other cases.

Classical Ising model

We begin by writing down the partition function in terms of Ising variables s_i assigned to each vertex (Fig. 4.16a),

$$\mathcal{Z} = \sum_{\boldsymbol{s}} \prod_{\langle i,j \rangle} e^{\beta s_i s_j}. \tag{4.50}$$

For later purposes, it will be convenient to interchangeably use binary variables $b_i = \{0, 1\}$ and $s_i = \{-1, 1\}$, where $s_i = (-1)^{b_i}$, to express each Ising configuration. We use the following graphical notation to represent Boltzmann weights on the horizontal and vertical edges of square lattice.

$$= \begin{cases} e^{\beta} & \text{if } b_i = b_j \\ e^{-\beta} & \text{otherwise} \end{cases} \tag{4.51}$$

It is possible to construct a defective edge by inserting a Pauli-x between connecting sites, which modify the Boltzmann weights as follows

$$= \begin{cases} e^{-\beta} & \text{if } b_i = b_j \\ e^{\beta} & \text{otherwise} \end{cases} \tag{4.52}$$

We use here a blue line to indicate the presence of a Pauli-x (or X) at an edge in (4.52). Its presence at an edge switches the interaction from ferromagnetic to anti-ferromagnetic while preserving the whole object as a valid partition function. Pauli-x at an edge also denotes the symmetry action. It is possible to have a tensor network description of the

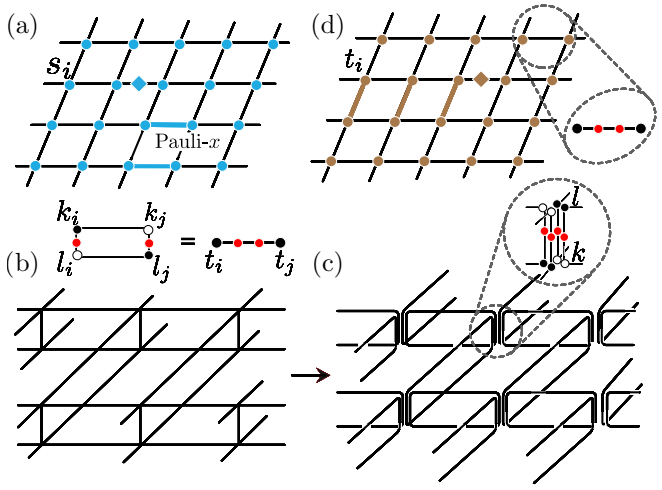

FIGURE 4.16: (a) Standard Ising model on a square lattice. The string of defective edges shown by colored edges indicates the presence of Pauli-x in the link. An edge with the diamond denotes an action corresponding to local order parameter. (b) The norm of the vacuum $|0,1\rangle$ constructed by contracting the bra and ket index. (c) More descriptive illustration for the tensor network of vacuum with the local structure of on-site tensors. (d) Ising model which emerged from the norm of the vacuum.

partition function where all the local tensors are invariant under the action of X on all the legs. This also implies that a partition function with a string of X's will remain invariant under any continuous deformation in the string provided that the endpoints remain fixed.

At this point, it is instructive to write down an analytic expression for the expectation value of average magnetization per two sites.

$$\sum_{\mathbf{b}} (\bullet\!-\!\blacklozenge\!-\!\bullet) \prod_{\substack{\langle i,j\rangle \\ \neq\langle 0,1\rangle}} \diagup = \sum_{\mathbf{s}} (s_0 + s_1)\, e^{\beta} \prod_{\substack{\langle i,j\rangle \\ \neq\langle 0,1\rangle}} e^{\beta s_i s_j} = \left(1 - \sinh^{-4}(2\beta)\right)^{1/8} \tag{4.53}$$

where the horizontal and vertical links in the product are expressed by an inclined edge. The cross sign on edge indicates local order parameter Z on the vertices labeled 0 and 1. Although, the link has negative weights, in analogy to (4.52), we define it as follows,

$$\bullet\!-\!\blacklozenge\!-\!\bullet := \begin{cases} (-1)^{b_i}\, e^{\beta} & \text{if } b_i = b_j \\ 0 & \text{otherwise.} \end{cases} \tag{4.54}$$

Anyonic vacuum and excitations

An important object to inspect in order to analyze the norm of a quantum state is the on-site transfer operator. We start by writing it pictorially for the $D(\mathbb{Z}_4)$ QD with deformation.

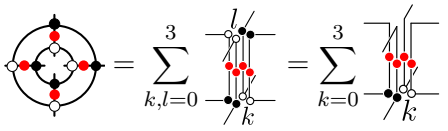

(4.55)

where each black circle in the sum with label k denotes X^k and X is the generator of $\mathbb{Z}_4$ with regular representation. The outline of circles specifies Hermitian conjugate. Red bubbles represent deformation $\exp(\theta X^2)$. The last equality is possible since black and red circles commute and the on-site tensors are isometric. The deformation modeled by the red bubbles drives the system from the $D(\mathbb{Z}_4)$ QD to $\mathbb{Z}_4 \boxtimes \mathbb{Z}_2$ TC phase. Using (4.55) we can write the norm of vacuum as

$$\langle 0,1|0,1\rangle = \sum_{k_i,l_i=0}^{3} \prod_{\text{rings}}$$ 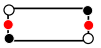 $$= \sum_{\boldsymbol{t}} \prod_{\text{edges}}$$  , (4.56)

where the product is over all the rings (Fig. 4.16(b,c)) and by using (4.55) we can shrink each ring 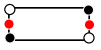 to an edge  with the following definition.

$$\text{  } = \operatorname{tr}\left(X^{t_i} e^{2\theta X^2} X^{t_j}\right)$$
$$= \begin{cases} 2(e^{\theta} + e^{-\theta}) & \text{if } t_i - t_j = 0 \pmod 4 \\ 2(e^{\theta} - e^{-\theta}) & \text{if } t_i - t_j = 2 \pmod 4 \\ 0 & \text{otherwise} \end{cases} \tag{4.57}$$

Each edge can be identified as an interaction in the Ising model on a square lattice. In order to be succinct we will write  as  . Since the Boltzmann weights are zero if $t_i - t_j = 1 \pmod 2$, we can write (4.56) as a sum over two copies of the Ising model on a square lattice (Fig. 4.16b).

$$\langle 0,1|0,1\rangle = \sum_{t_i=0,2} \prod_{\langle i,j\rangle}$$ $$+ \sum_{t_i=1,3} \prod_{\langle i,j\rangle}$$ (4.58)

Terms in (4.50) behave analogously to (4.58). By identifying different combinations in (4.51) and (4.57) with each other we can write

$$e^{\beta} = 2\left(e^{\theta} + e^{-\theta}\right) \ , \ e^{-\beta} = 2\left(e^{\theta} - e^{-\theta}\right)$$

which implies $\beta = \tanh^{-1}\left(e^{-2\theta}\right)$.

Standard Ising model							Norm of vacuum
$b_i = b_j$	e^{β}	$e^{-\beta}$	$(-1)^{b_i}\, e^{\beta}$	$2\left(\sqrt{-1}\right)^{t_i}$	$2(e^{\theta} - e^{-\theta})$	$2(e^{\theta} + e^{-\theta})$	$t_i - t_j = 0$
$b_i \neq b_j$	$e^{-\beta}$	e^{β}	0	0	$2(e^{\theta} + e^{-\theta})$	$2(e^{\theta} - e^{-\theta})$	$t_i - t_j = 2$
				0	0	0	$t_i - t_j = 1$ $t_i - t_j = 3$

TABLE 4.1: Comparison between the Boltzmann weights of standard Ising model(blue) and two decoupled copies of Ising models(brown) on the square lattice which emerged from the norm of the quantum vacuum.

Now, consider the anyon excitation $|0, i\rangle$ which gets confined as the system approaches the critical point. More precisely, the norm of $|0, i\rangle$ is zero in the $\mathbb{Z}_4 \boxtimes \mathbb{Z}_2$ TC phase. The norm of the excitation, $\langle 0, i|0, i\rangle$, contains the ring 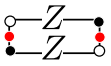 which shrinks to the edge 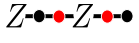 . We can write the norm as

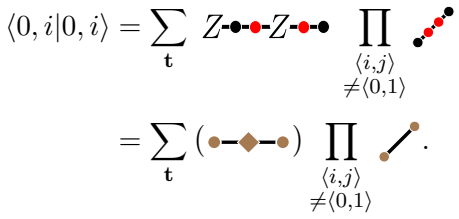

(4.59)

The brown diamond indicates a charge which is given by $Z := Z_1$ in the ket and bra layer. The trace over each configuration on the edge is defined as follows

$$= \mathrm{tr}\left(ZX^{t_i}e^{\theta X^2}Ze^{\theta X^2}X^{t_j}\right)$$

$$= \begin{cases} 2\left(\sqrt{-1}\right)^{t_i} & \text{if } t_i - t_j = 0 \pmod 4 \\ 0 & \text{otherwise.} \end{cases} \tag{4.60}$$

We summarize the Boltzmann weight of all the configurations for two models in Tab.4.1.

It is clear from the table that an edge  corresponds to the evaluation of magnetization per site up to a weighting factor $2(e^{\theta} + e^{-\theta})$. Using (4.53) for magnetization per site and dividing by

$$2(e^{\theta} + e^{-\theta}) = \frac{1}{2}\left(\tanh^{1/2}\beta + \tanh^{-1/2}\beta\right),$$

in order to compensate for the weighing factor we get an analytic expression for the norm of $|0, i\rangle$.

$$\langle 0, i|0, i\rangle = \frac{2\left(1 - \sinh^{-4} 2\beta\right)^{1/8}}{\tanh^{1/2}\beta + \tanh^{-1/2}\beta} \tag{4.61}$$

The excitation $|2,0\rangle$ gets condensed to the vacuum in the $\mathbb{Z}_4 \boxtimes \mathbb{Z}_2$ TC phase. Rings 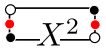 create a string of defective edges. In order to be consistent with notation used in (4.52), we write 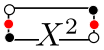 as . Tab. 4.1 contains the Boltzmann weights for different configurations of in column 6. Overlap of excitation $|2,1\rangle$ with vacuum $|0,1\rangle$ creates a semi-infinite string of edges (Fig. 4.16d). In order to get an analytic expression for condensate fraction $\langle 0,1|2,1\rangle$, we first map the model from the 2D classical Ising on the square lattice to a 1D quantum Ising chain. The Kramers-Wannier duality of the 2D classical Ising model manifests itself as a 1D quantum Ising duality using disorder operators on the dual lattice.

$$\tau^z_{i+1/2} = \prod_{j\leq i} \sigma^x_j \quad , \quad \tau^x_{i+1/2} = \sigma^z_i \sigma^z_{i+1} \tag{4.62}$$

$\sigma^x_i \left(\tau^x_{i+1/2}\right)$ and $\sigma^z_i \left(\tau^z_{i+1/2}\right)$ are Pauli matrices on (dual) square lattice. Using this transformation, a semi-infinite domain wall created by a string of X's $(...XXX)$ translates into point operator corresponding to magnetization per site on the dual lattice. The condensate fraction $\langle 0,1|2,1\rangle$ can be written analytically as

$$\langle 2,1|0,1\rangle = \left(1 - \sinh^{-4} 2\beta^*\right)^{1/8}, \tag{4.63}$$

where β^* is related to β by $\sinh 2\beta \ \sinh 2\beta^* = 1$.

We have computed analytically two condensate fractions in (4.61) and (4.63). The rest of the non-zero but not constant overlaps can be proved equal to either of the two by using following identities.

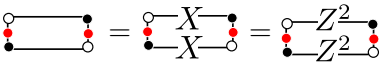

(4.64)

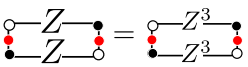

(4.65)

The equality holds for every value of θ along the phase transition. The analytic results conforms exactly with the numerical data in Fig. 4.14a.

The norm of the vacuum for the phase transition between the $D(\mathbb{Z}_4)$ QD and $\mathbb{Z}_2 \boxtimes \mathbb{Z}_1$ TC with explicit symmetry breaking can also be mapped to the classical Ising model where the Ising variables have different Boltzmann weights. The $D(\mathbb{Z}_4)$ QD $\leftrightarrow \mathbb{Z}_4 \boxtimes \mathbb{Z}_2$ DS phase transition also gives rise to an Ising model but the identification of Ising variables is subtle as the local tensor network description of the DS model breaks the lattice symmetry.

4.5.3 Phase transitions between toric codes and double semion model

The phase transition between toric codes and double semion model have been studied using exact diagonalization in [71] and the findings indicate that the phase transition is first-order on a 2D system. Here, we present our results regarding the phase transition between the two models and explore the different possibilities which open up by realizing these topological phase in the framework of $\mathbb{Z}_4$-invariant tensors.

$\mathbb{Z}_4 \boxtimes \mathbb{Z}_2$ TC and $\mathbb{Z}_4 \boxtimes \mathbb{Z}_2$ DS

We have already studied a phase transition between $\mathbb{Z}_4 \boxtimes \mathbb{Z}_2$ DS and $\mathbb{Z}_4 \boxtimes \mathbb{Z}_2$ TC which is governed by linear interpolation of the on-site transfer operators (Fig. 4.10a). Using different numerical probes, we characterized the phase transition to be first-order. As the system approaches the transition point from the RG fixed point of $\mathbb{Z}_4 \boxtimes \mathbb{Z}_2$ DS phase, the deconfined anyons $\{|1, \pm i\rangle, |3, \pm i\rangle\}$ get confined. Similarly, after phase transition in the $\mathbb{Z}_4 \boxtimes \mathbb{Z}_2$ TC phase the anyons $\{|1, \pm 1\rangle, |3, \pm 1\rangle\}$ get deconfined while the anyon $|2, 1\rangle$ gets condensed to the vacuum.

It turns out that the boundaries of two phases, TC and DS model, exhibit a much richer behavior. In addition to the first-order phase transition, we can also make a continuous phase transition between the two models. There exists a multi-critical point on $\theta_{\mathrm{TC},Z_2} = 0$ hyperplane which is analytic and shared by four phases. A path through it with endpoints in the $\mathbb{Z}_4 \boxtimes \mathbb{Z}_2$ DS and $\mathbb{Z}_4 \boxtimes \mathbb{Z}_2$ TC phase yields a second-order phase transition. The continuous nature of phase transition is illustrated by the behavior of condensation/decondensation and confinement/deconfinement fractions in Fig. 4.17a, where the solid lines denote the closed form solutions. The path traversed in Fig. 4.17a is along the line labeled as (III) in the phase diagram (Fig. 4.13a) and it is parametrized as $(\theta_{\mathrm{TC}}, \theta_{\mathrm{TC},Z_2}, \theta_{\mathrm{DS}}) = (\theta, 0, (\theta_c - 1)\theta/\theta_c + 1)$, where $\theta_c = \frac{1}{2}\ln(1 + \sqrt{2})$.

The continuous nature of phase transition is also exhibited by the diverging correlation length ξ as the system approaches critical point. Fig. 4.17a(i) shows ξ computed from the fixed points of the transfer operator using channel operator. Correlation length of the system computed from the gap of the transfer operator using excitation ansatz also diverges (Fig. 4.17a(ii)). Since the phase transition lies in the Ising universality class, we observe a linear scaling for $\xi^{-1} = \ln \lambda_1$ in the critical regime.

Although, the boundary phases of TC and DS model have $\mathbb{Z}_4 \boxtimes \mathbb{Z}_2$ symmetry, the projective action of (X, X) and $(\mathbb{I}, X^2)$ onto the virtual indices of boundary phase is characteristically different for the two phases (also see Eqs. (4.23) and (4.30)). A

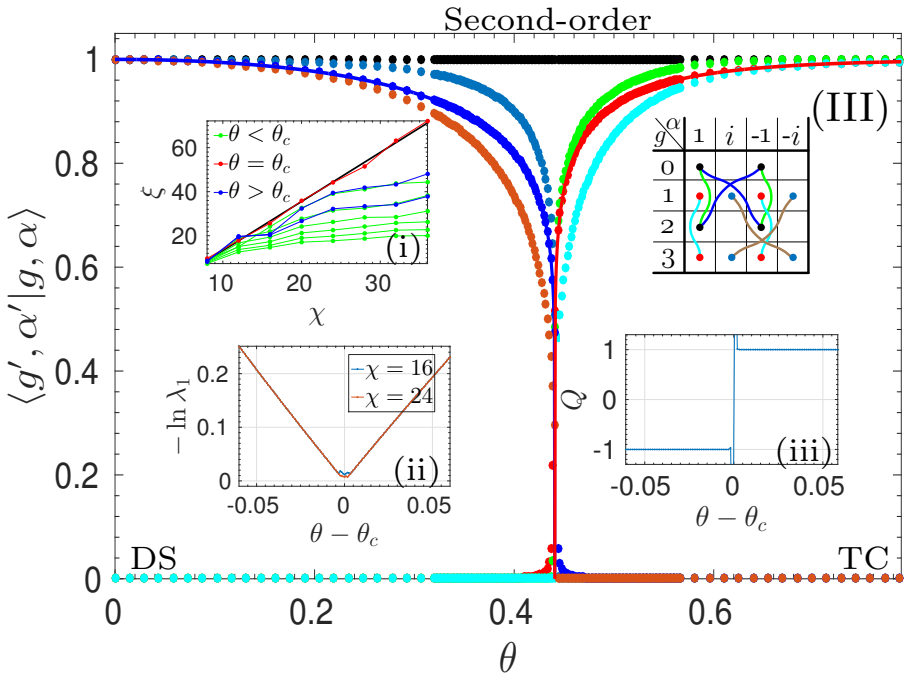

FIGURE 4.17: Different fractions for the phase transition between DS and TC across the line (III) in Fig. 4.13a with $\chi = 24$. Anyon table at the top right defines the color legend of overlaps. (i) Shows the correlation length ξ of the boundary phase. (ii) First-excited state of the transfer operator computed using excitation ansatz. (iii) Behavior of an SPT gauge-invariant in the vicinity of phase transition.

measure defined by the gauge invariant of the form

$$Q = \mathrm{Tr}\left(\sigma_{1,1}\sigma_{0,2}\sigma_{1,1}^{-1}\sigma_{0,2}^{-1}\right), \tag{4.66}$$

where $\sigma_{g,g'}$ are the largest eigenvectors of dressed channel operator $\mathbb{F}_{g,g'}$ (Fig. 4.9b). The value of Q can be used to distinguish TC and DS phase by exploiting the distinct nature of SPT order in their boundary phase [72]. Fig. 4.17a(iii) shows Q in the vicinity of phase transition. Although the sharp behavior of Q around the critical point hides the universal features of phase transition, the jump in its value can be used to determine the position of the critical point.

$\mathbb{Z}_2 \boxtimes \mathbb{Z}_1$ TC and $\mathbb{Z}_4 \boxtimes \mathbb{Z}_2$ DS

In contrast to $\mathbb{Z}_4 \boxtimes \mathbb{Z}_2$, there does not exist a direct path between $\mathbb{Z}_2 \boxtimes \mathbb{Z}_1$ TC and $\mathbb{Z}_4 \boxtimes \mathbb{Z}_2$ DS on $\theta_{\mathrm{TC}} = 0$ hyperplane in Fig. 4.13a. However, a direct phase transition between the two phases can be induced by linear interpolation of the on-site transfer operators. Moving along the path which is traced by linear interpolation (see (4.44)) leads to a direct transition (i.e., does not encounter an intermediate phase) between the two phases. The phase transition is governed by the vanishing condensation/decondensation fractions

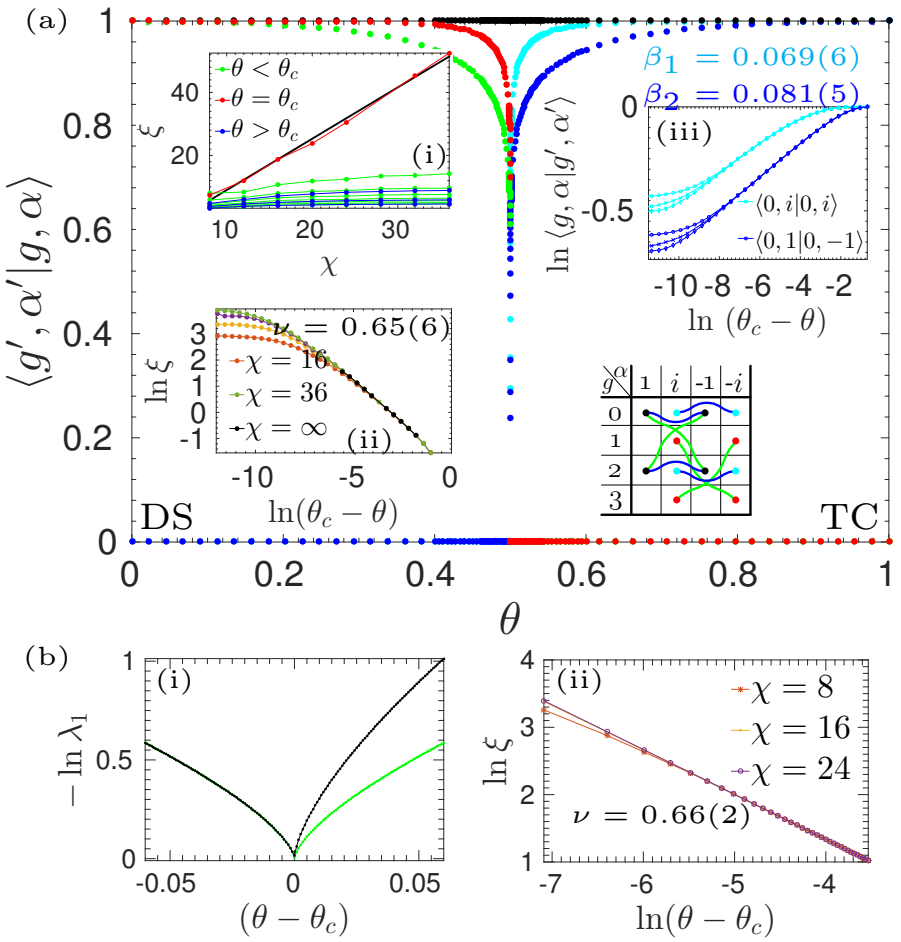

FIGURE 4.18: Different fractions along the phase transition between $\mathbb{Z}_4 \boxtimes \mathbb{Z}_2$ DS and $\mathbb{Z}_2 \boxtimes \mathbb{Z}_1$ TC. Anyon table defines the legend of different fractions as explained earlier. a(i, ii) illustrates the correlation length of the boundary phase for different bond dimension χ in the vicinity of the critical point. a(iii) shows the scaling condensation and confinement fraction used for the computation of critical exponents β_1 and β_2. b(i) The gap above the lowest energy state of transfer operator computed by using excitation ansatz. b(ii) Almost the same value of critical exponent ν is obtained from the scaling of correlation length computed by using the excitation ansatz.

and enriched by an occurrence of spontaneous symmetry breaking in the fixed points of the transfer operator. As the system moves from $\mathbb{Z}_4 \boxtimes \mathbb{Z}_2$ DS towards $\mathbb{Z}_2 \boxtimes \mathbb{Z}_1$ TC phase, anyon $|2, -1\rangle$ gets de-condensed which is followed by the condensation of anyon $|0, -1\rangle$ into the vacuum. Deconfined anyons $\{|1, \pm i\rangle, |3, \pm i\rangle\}$ get confined as the system is tuned towards the critical point in DS phase. After the phase transition we observe the deconfinement of anyons $\{|0, \pm i\rangle|2, \pm i\rangle\}$.

Fig. 4.18a shows the overlap of anyonic excitations in the two phases. Phase transition occurs at $\theta_c = 0.5$. Diverging correlation length of the boundary phase as the system approaches the critical point in Fig. 4.18a(i) is an indication of continuous phase transition. Critical exponent ν is obtained from the slope of boundary phase correlation

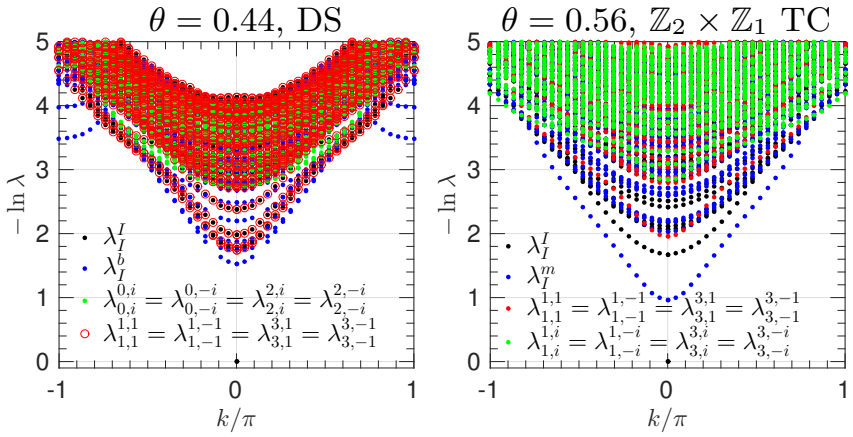

FIGURE 4.19: Dispersion relation of the transfer operator at the data points in the vicinity of phase transition in the $\mathbb{Z}_4 \boxtimes \mathbb{Z}_2$ DS and $\mathbb{Z}_2 \boxtimes \mathbb{Z}_1$ TC phase. The computations have been performed for the bond dimension $\chi = 24$.

length ξ on the log-log plot as shown in Fig. 4.18a(ii) and we find that $\nu = 0.65(6)$. Fig. 4.18a(iii) shows the scaling of $\ln\langle 0, i|0, i\rangle$ (light blue) and $\ln\langle 0, -1|0, 1\rangle$ (dark blue) as a function of distance from the critical point on log-scale. From the slopes we get $\beta_1 = 0.069(6)$ and $\beta_2 = 0.081(5)$. The values of the critical exponents identify the phase transition with the Ashkin-Teller universality class.

The behavior of phase transition around the critical point is determined by the topological excitations created by the domain walls. As one move from $\mathbb{Z}_2 \boxtimes \mathbb{Z}_1$ TC towards $\mathbb{Z}_4 \boxtimes \mathbb{Z}_2$ DS, the broken symmetries $(\mathbb{I}, X^2)$ and (X, X) get restored. The domain wall excitations created by these symmetries decisively close the gap at the critical point. Fig. 4.18b(i) shows the first excited state of the transfer operator. Green excitations represent excited states which have been constructed by broken symmetry domain walls. The slope of $\ln \lambda_1 = \xi^{-1}$ on the log-log plot also gives the same critical exponent ν as we obtained in Fig. 4.18a(ii).

Fig. 4.19 shows the distinct features of the dispersion relation of the transfer operator at the data points in the vicinity of the phase transition. Since the transfer operator is $\mathbb{Z}_4 \boxtimes \mathbb{Z}_4$ invariant, we can label each excitation of the transfer operator for the given k as $\lambda_{g,\alpha}^{g',\alpha'}$, where (g, g') is a label for the conjugacy class and (α, α') is a label for an irrep of $\mathbb{Z}_4 \boxtimes \mathbb{Z}_4$. It is important to note that the different species of anyonic particles in the TC and DS phase can be labeled by (g, α).

As the system is tuned from the DS phase towards the critical point, bosonic excitations get condensed to the vacuum, and this property is crucial in determining the behavior of the system. Remarkably as first suggested in [13], that condensation of bosonic anyons is manifested in the excitation spectrum of the transfer operator. The low lying excitations labeled as λ_I^b in Fig. 4.19a are identified with the condensation of bosons. Furthermore,

the excitations labeled as $\lambda_{0,i}^{0,i}$ and $\lambda_{2,i}^{2,i}$ represent the deconfinement of e and em anyons respectively.

Similarly, on the other side of the critical point in $\mathbb{Z}_2 \boxtimes \mathbb{Z}_1$ TC phase, the behavior of the system is characterized by the condensation of magnetic anyons (labeled as λ_I^m in Fig. 4.19b). Excitation labeled as $\lambda_{1,i}^{1,i}$ and $\lambda_{1,-i}^{1,-i}$ manifest the deconfinement of semions and their conjugates.

Unitary equivalence between $\mathbb{Z}_4 \boxtimes \mathbb{Z}_2$ DS and $\mathbb{Z}_2 \boxtimes \mathbb{Z}_1$ TC

The existence of critical point θ_c to be at exactly 0.5 and the equivalence of different fractions on the two sides of θ_c (Fig. 4.18a) points to a deeper structure in the transfer operator $\mathbb{T}$ as these fractions are a manifestation of the spectral properties of the transfer operator. It turns out that the transfer operators at the RG fixed point of $\mathbb{Z}_4 \boxtimes \mathbb{Z}_2$ DS and $\mathbb{Z}_2 \boxtimes \mathbb{Z}_1$ TC phase can be transformed into each other by a unitary U which has a finite bond dimension. The local action of unitary on the on-site transfer operators implies the following relation between the transfer operators on the two sides of the critical point.

$$U\mathbb{T}(\theta)U^\dagger = \mathbb{T}(1-\theta), \tag{4.67}$$

where U is a unitary and θ models the deformation which is prescribed by linear interpolation. Furthermore, it has been tested numerically that the eigenvalues of the transfer operator satisfy $\boldsymbol{\sigma}(\mathbb{T}(\theta)) = \boldsymbol{\sigma}(\mathbb{T}(1-\theta))$, where the eigenvalues have been calculated for finite transfer operators with open boundary conditions.

Here, we give an MPO construction of a unitary which transform the transfer operators of $\mathbb{Z}_4 \boxtimes \mathbb{Z}_2$ DS and $\mathbb{Z}_2 \boxtimes \mathbb{Z}_1$ TC into each other. It is helpful for later purposes to first write down the local tensors which represent the RG fixed points of two phases. In the case of the $\mathbb{Z}_4 \boxtimes \mathbb{Z}_2$ DS model

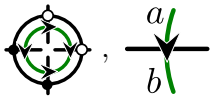

$$= \begin{pmatrix} \{\mathbb{I}\}_{a=0,b=0} & \{X^2Z^2\}_{a=0,b=1} \\ \{Z^2\}_{a=1;b=0} & \{X^2\}_{a=1;b=1} \end{pmatrix} \tag{4.68}$$

The green ring is an MPO projector for $\mathbb{Z}_4 \boxtimes \mathbb{Z}_2$ DS applied on $D(\mathbb{Z}_4)$ QD (black ring). In later usage, we will drop the subscripts in matrix notation. Similarly, for the $\mathbb{Z}_2 \boxtimes \mathbb{Z}_1$ TC

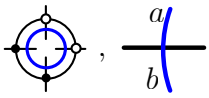

$$= \begin{pmatrix} \mathbb{I}+Z^2 & 0 \\ 0 & \mathbb{I}-Z^2 \end{pmatrix} \tag{4.69}$$

Moreover, the on-site transfer operators or the double tensors of two models have the same representation as given in (4.68) and (4.69). The transfer operator constructed by blocking the double tensors, $\mathbb{E}(\theta) = \theta\mathbb{E}_{\mathrm{DS}} + (1-\theta)\mathbb{E}_{\mathrm{TC}}$, can be interpreted as a sum of alphabetic strings where each alphabet is either DS or TC double tensor. And the local

tensor u of the desired MPO unitary U is expected to swap the double tensor of $\mathbb{Z}_4 \boxtimes \mathbb{Z}_2$ DS with the double tensor of $\mathbb{Z}_2 \boxtimes \mathbb{Z}_1$ TC. Local tensor u should act to substitute the double tensor of the DS with the double tensor of TC and vice-versa.

Motivated by the construction of discriminating string order parameters for topological phases in [73], we start by writing the local tensor description of MPO U.

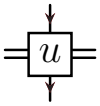

$$= \begin{pmatrix} \mathbb{I} \otimes (\mathbb{I} + X^2) & \mathbb{I} \otimes (\mathbb{I} - X^2) \\ X \otimes (X^3 - X) & X \otimes (X^3 + X) \end{pmatrix}, \tag{4.70}$$

where the top (bottom) index is identified with the row (column) index of the matrix and the arrow head points in the direction of column index. Now, we show why (4.70) is the right description of u by showing its action on the on-site transfer operators. With u defined in (4.70), its action on $\mathbb{Z}_4 \boxtimes \mathbb{Z}_2$ DS tensor is

$$= \begin{pmatrix} X_+ & Z^2X_+ & X_- & -Z^2X_- \\ Z^2X_+ & X_+ & Z^2X_- & -X_- \\ X_- & Z^2X_- & X_+ & -Z^2X_+ \\ -Z^2X_- & -X_- & -Z^2X_+ & X_+ \end{pmatrix}, \tag{4.71}$$

where $X_\pm = \mathbb{I} \pm X^2$. Although, it is not very clear in the above form, it is more insightful to understand the action by a unitary transformation. Consider a unitary M with the following definition,

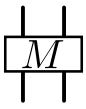

$$:= \frac{1}{2} \begin{pmatrix} -1 & 1 & 1 & 1 \\ 1 & -1 & 1 & 1 \\ 1 & 1 & -1 & 1 \\ 1 & 1 & 1 & -1 \end{pmatrix} \tag{4.72}$$

where the joint of the top (bottom) indices corresponds to the row (column) index of the matrix. By applying M to (4.71), we obtain

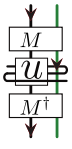

$$= \begin{pmatrix} Z_+ & 0 & 0 & 0 \\ 0 & Z_+X^2 & 0 & 0 \\ 0 & 0 & Z_- & 0 \\ 0 & 0 & 0 & Z_-X^2 \end{pmatrix} \tag{4.73}$$

where $Z_\pm = \mathbb{I} \pm Z^2$. Matrix entries across the main diagonal correspond to the four blocks (or fixed points since each block can be identified with a fixed point) of $\mathbb{Z}_2 \boxtimes \mathbb{Z}_1$ TC (see (4.25)). MPO projectors (blue and green rings) in (4.68) and (4.69) commute with the black MPO of the $D(\mathbb{Z}_4)$ QD, so the action of u on the DS tensor can be

summarized as

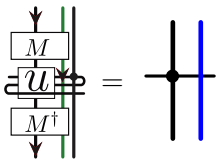

(4.74)

where,

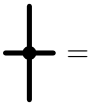

$$= \begin{pmatrix} \mathbb{I} & 0 & 0 & 0 \\ 0 & X & 0 & 0 \\ 0 & 0 & X^2 & 0 \\ 0 & 0 & 0 & X^3 \end{pmatrix}. \tag{4.75}$$

Now, we consider the action of u on the local tensor of the $\mathbb{Z}_2 \boxtimes \mathbb{Z}_1$ TC.

$$= \begin{pmatrix} X_+Z_+ & X_-Z_+ & 0 & 0 \\ X_-Z_- & X_+Z_- & 0 & 0 \\ 0 & 0 & X_+Z_- & X_-Z_- \\ 0 & 0 & X_-Z_+ & X_+Z_+ \end{pmatrix} \tag{4.76}$$

In order to study the structure of $\mathbb{Z}_4 \boxtimes \mathbb{Z}_2$ DS blocks, again we define a unitary

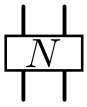

$$:= \frac{1}{\sqrt{2}} \begin{pmatrix} 1 & 1 & 0 & 0 \\ 1 & -1 & 0 & 0 \\ 0 & 0 & -1 & 1 \\ 0 & 0 & 1 & 1 \end{pmatrix} \tag{4.77}$$

By doing a unitary transformation on (4.76),

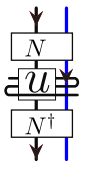

$$= \begin{pmatrix} \mathbb{I} & X^2Z^2 & 0 & 0 \\ Z^2 & X^2 & 0 & 0 \\ 0 & 0 & \mathbb{I} & X^2Z^2 \\ 0 & 0 & Z^2 & X^2 \end{pmatrix} \tag{4.78}$$

The two blocks are completely identical and correspond to one of the symmetry broken fixed points of $\mathbb{Z}_4 \boxtimes \mathbb{Z}_2$ DS model. Similar to (4.74), the action of u on the $\mathbb{Z}_2 \boxtimes \mathbb{Z}_1$ tensor with the local tensor of $D(\mathbb{Z}_4)$ QD produces the local tensor of the $\mathbb{Z}_4 \boxtimes \mathbb{Z}_2$ DS model.

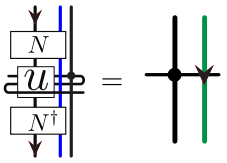

(4.79)

Furthermore, from the action of u in (4.74) and (4.79), we can also verify that the following relation also holds between u and the on-site transfer operators of the $\mathbb{Z}_4 \boxtimes \mathbb{Z}_2$

DS and the $\mathbb{Z}_2 \boxtimes \mathbb{Z}_1$ TC.

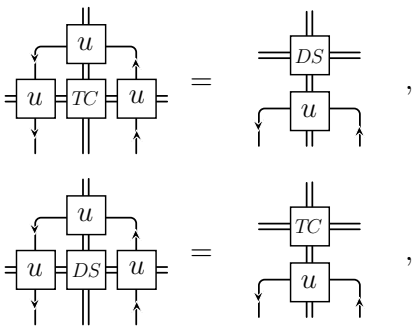

(4.80)

where,

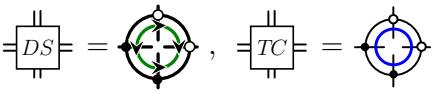

(4.81)

In order for the relation in (4.67) to hold, we insert u at one end of the transfer operator and by using (4.80) and by zipping u to the other end of the transfer operator we can achieve the global action of U as required.

4.5.4 Important features of $\mathbb{Z}_4$ phase diagram

Here we discuss some of the generic features of the phase diagram of $\mathbb{Z}_4$-invariant tensors which we mapped in Fig. 4.13.

First, we consider the $\theta_{\mathrm{DS}} = 0$ hyperplane. The plane is characterized by four phases. The origin lies in $D(\mathbb{Z}_4)$ QD and the other three corners correspond to the $\mathbb{Z}_4 \boxtimes \mathbb{Z}_2$ TC, $\mathbb{Z}_2 \boxtimes \mathbb{Z}_1$ TC and $\mathbb{Z}_2 \boxtimes \mathbb{Z}_2$ TP. The phase transitions across the lines (I) and (II) in Fig. 4.13 lie in the Ising universality class as already discussed (Fig. 4.14,4.15a). Critical exponents of the phase transitions between $\mathbb{Z}_4 \boxtimes \mathbb{Z}_2$ TC $\leftrightarrow$ $\mathbb{Z}_2 \boxtimes \mathbb{Z}_2$ TP and $\mathbb{Z}_2 \boxtimes \mathbb{Z}_1$ TC $\leftrightarrow$ $\mathbb{Z}_2 \boxtimes \mathbb{Z}_2$ TP on $\theta_{\mathrm{DS}} = 0$ hyperplane also classify the phase transition in the Ising universality class. Moreover, numerical tests of phase transitions between points in different phases on this hyperplane (away from the multi-critical regime) indicate that all the phase transitions on this hyperplane can be identified with the Ising universality class.

$\theta_{\mathrm{TC}} = 0$ hyperplane is characterized by $D(\mathbb{Z}_4)$ QD, $\mathbb{Z}_2 \boxtimes \mathbb{Z}_1$ TC, $\mathbb{Z}_4 \boxtimes \mathbb{Z}_2$ DS, and $\mathbb{Z}_2 \boxtimes \mathbb{Z}_2$ TP. The phase transition across the line labeled as (III) between $D(\mathbb{Z}_4)$ QD and $\mathbb{Z}_4 \boxtimes \mathbb{Z}_2$ DS can be mapped to the Ising model (Fig. 4.15b). On the other hand, phase transitions $\mathbb{Z}_4 \boxtimes \mathbb{Z}_2$ DS $\leftrightarrow$ $\mathbb{Z}_2 \boxtimes \mathbb{Z}_2$ TP and $\mathbb{Z}_2 \boxtimes \mathbb{Z}_1$ TC $\leftrightarrow$ $\mathbb{Z}_2 \boxtimes \mathbb{Z}_2$ TP on $\theta_{\mathrm{TC}} = 0$ plane across lines (VI) and (VII) have the same critical exponents but they do not map to the Ising universality class. The critical exponents are $\beta_1 = 0.04(1)$, $\beta_2 = 0.23(4)$, and $\nu = 1$.

In case of $\theta_{\mathrm{TC},Z_2} = 0$ hyperplane, we again have four distinct phases and there exists a multi-critical point at $\boldsymbol{\theta} = \left(\frac{1}{2}\ln(1+\sqrt{2}), 0, \frac{1}{2}\ln(1+\sqrt{2})\right)$ which is shared by the boundaries of four phases. The multi-critical point vanishes for the values $\theta_{\mathrm{TC},Z_2} > 0$. The phase transitions across the lines labeled as (I), (III), and (IV) in Fig. 4.13 has already been discussed earlier with an explicit mapping to the 2D Ising model in case of (I) (see Sec. 4.5.2). Phase transitions on this plane are analytic. Exact mapping in terms of Ising variables is not known but the analytic expressions of order parameters (condensation and confinement fractions) suggest that every phase transition on this plane can be mapped to the Ising model.

An interesting feature of the phase diagram is a continuous change in the universality class of phase transitions across the $\theta_{\mathrm{DS}} = 1$ hyperplane (Fig. 4.20a). The plane is characterized by $\mathbb{Z}_4 \boxtimes \mathbb{Z}_2$ DS and $\mathbb{Z}_2 \boxtimes \mathbb{Z}_2$ TP. As mentioned above, the phase transition across the line (V) maps to Ising model with critical exponent of order parameter $\beta_\pm = 1/8$, on the other hand the critical exponents of the order parameters across the line (VI) are different. We observe a continuous change in the value of β's as one move across the critical regime on $\theta_{\mathrm{DS}} = 1$ hyperplane. Let $(\theta_{\mathrm{TC}}, \theta_{\mathrm{TC},Z_2}) = t\,(\cos\phi, \sin\phi)$ be the parametrization of lines passing through the origin of $\theta_{\mathrm{DS}} = 1$ hyperplane. Fig. 4.20c shows the scaling of order parameters (i.e. $\langle 0, i|0, i\rangle$ and $\langle 0, 1|2, -1\rangle$) in the critical regime for $\phi = [0, \pi/2]$. Critical exponents $\beta_\pm$ computed from the slope of order parameters on a log-log plot are given in Fig. 4.20d. It is important to emphasize at this point that the universal features of the phase transition (i.e. the values of critical exponents) do not depend on the direction one chooses to approach the critical point.

4.5.5 Phase diagrams of toric codes and double semion model

We now examine the behavior of phase transitions which can be obtained by further deforming the toric codes and double semion model down to the trivial phases.

$\mathbb{Z}_4 \boxtimes \mathbb{Z}_2$ Toric code

In the case of $\mathbb{Z}_4 \boxtimes \mathbb{Z}_2$ toric code, an action of the form defined in (4.39) on the physical indices of on-site tensors can induce a phase transition to either $\mathbb{Z}_4 \boxtimes \mathbb{Z}_4$ TP or $\mathbb{Z}_2 \boxtimes \mathbb{Z}_2$ TP by spontaneously enhancing or reducing the symmetry of the transfer operator fixed points. The deformation is parametrized by two variables (θ_1, θ_2). At (high-θ_1, low-θ_2) the system is in $\mathbb{Z}_4 \boxtimes \mathbb{Z}_4$ TP, whereas at (low-θ_1, high-θ_2) the deformation acts to give $\mathbb{Z}_2 \boxtimes \mathbb{Z}_2$ TP. Motion towards the $\mathbb{Z}_4 \boxtimes \mathbb{Z}_4$ TP from $\mathbb{Z}_4 \boxtimes \mathbb{Z}_2$ TC leads to the confinement of anyons $|*, -1\rangle$ which is followed by the condensation of $\{|1, 1\rangle, |3, 1\rangle\}$ to the vacuum. Increase in θ_2 at low-θ_1 confines anyons $\{|1, \pm 1\rangle, |3, \pm 1\rangle\}$. The phases

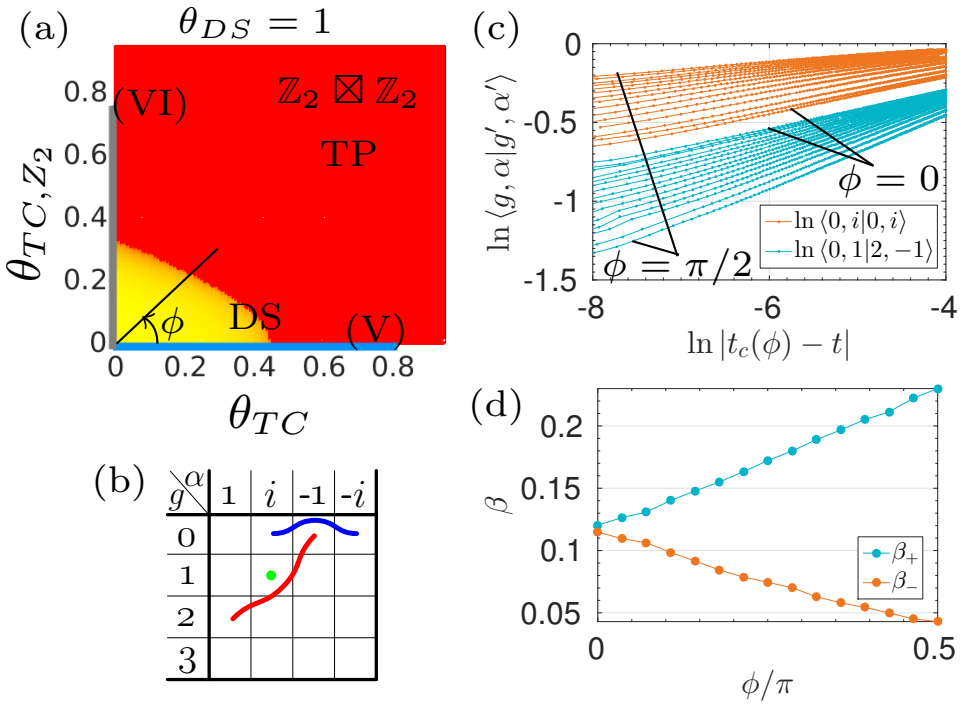

FIGURE 4.20: (a) $\theta_{\text{DS}} = 1$ hyperplane of the phase diagram which we constructed in Fig. 4.13.(b) Anyon table define the color of fractions which have been used for filling the RGB value of each point on the plane in (a). (c) Scaling of $\langle 0, i | 0, i \rangle$ and $\langle 0, 1 | 2, -1 \rangle$ for values of ϕ between 0 and $\pi/2$. (d) Change in the value of β's for different ϕ's.

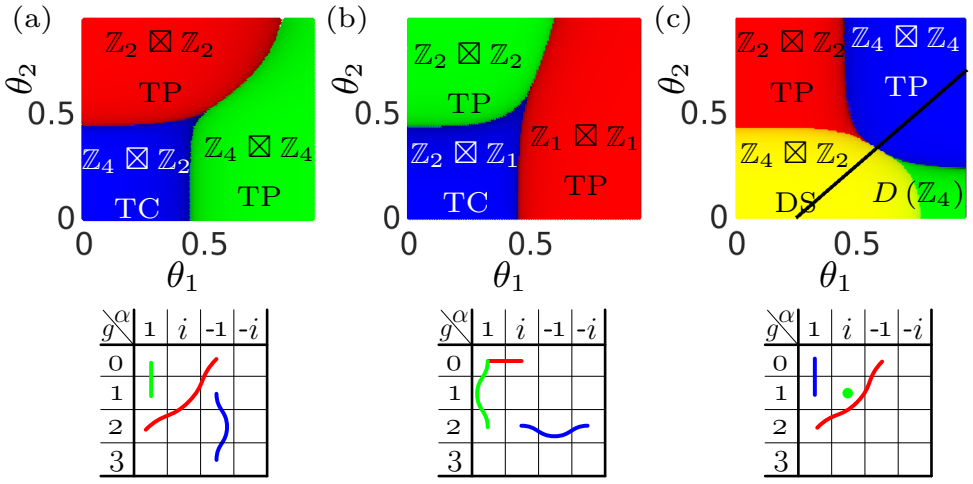

FIGURE 4.21: Phase diagrams of topologically trivial phases which can be induced by continuous deformations on $\mathbb{Z}_4 \boxtimes \mathbb{Z}_2$ TC(a), $\mathbb{Z}_2 \boxtimes \mathbb{Z}_1$ TC(b), and $\mathbb{Z}_4 \boxtimes \mathbb{Z}_2$ DS(c). The corresponding anyon table below each of the phase diagram defines the colors of overlaps (condensation+confinement fractions) which have been used to depict and distinguish different phases. $\chi = 16$ has been used for the computation of fractions using iMPS algorithm.

which can be realized by the deformation as a function of (θ_1, θ_2) can be illustrated by plotting certain fractions which can sufficiently distinguish the phases (Fig. 4.21a).

We find that away from the multi-critical regime, the phase transitions at the interface of $\mathbb{Z}_4 \boxtimes \mathbb{Z}_2$ TC and the two trivial phases in Fig. 4.21a lie in the Ising universality class.

$\mathbb{Z}_2 \boxtimes \mathbb{Z}_1$ Toric code

The phase diagram of $\mathbb{Z}_2 \boxtimes \mathbb{Z}_1$ TC can be studied by the deformation in (4.40). The phase transition from $\mathbb{Z}_2 \boxtimes \mathbb{Z}_1$ TC to $\mathbb{Z}_1 \boxtimes \mathbb{Z}_1$ TP is accomplished by confinement of anyons $|2, *\rangle$. The charge excitations are condensed in $\mathbb{Z}_1 \boxtimes \mathbb{Z}_1$ TP. On the other hand, as the system approaches the critical point from $\mathbb{Z}_2 \boxtimes \mathbb{Z}_1$ towards $\mathbb{Z}_2 \boxtimes \mathbb{Z}_2$ TP a spontaneous restoration of a broken symmetry leads to the condensation of anyons $|2, \pm 1\rangle$, while the excitations $\{|0, \pm i\rangle, |2, \pm i\rangle\}$ get confined. The phase diagram which is unfolded by the deformation is shown in Fig. 4.21b. At $\theta_1 = 0$, the phase transition between $\mathbb{Z}_2 \boxtimes \mathbb{Z}_1$ TC and $\mathbb{Z}_2 \boxtimes \mathbb{Z}_2$ TP can be mapped to the Ising model. Furthermore away from the multi-critical regime, the boundaries between $\mathbb{Z}_2 \boxtimes \mathbb{Z}_1$ TC and the two trivial phases can be described by the phase transitions which lie in the Ising universality class.

$\mathbb{Z}_4 \boxtimes \mathbb{Z}_2$ Double semion model

Now, we explain how $\mathbb{Z}_4 \boxtimes \mathbb{Z}_2$ DS model can be deformed into TPs and describe the properties of corresponding phase transitions. The deformation can be modeled by the action in (4.41). Different phases which can be realized as a function of (θ_1, θ_2) are plotted in Fig. 4.21c. The four corners of the plane correspond to $\mathbb{Z}_4 \boxtimes \mathbb{Z}_2$ DS, $D(\mathbb{Z}_4)$ QD, $\mathbb{Z}_2 \boxtimes \mathbb{Z}_2$ TP, and $\mathbb{Z}_4 \boxtimes \mathbb{Z}_4$ TP.

It is only in the vicinity of $D(\mathbb{Z}_4)$ QD that $\mathbb{Z}_4 \boxtimes \mathbb{Z}_2$ DS shares a boundary with $\mathbb{Z}_4 \boxtimes \mathbb{Z}_4$ TP. $(\theta_1^T, \theta_2^T) = (0.5830, 0.3313)$ is one the transition points between DS and $\mathbb{Z}_4 \boxtimes \mathbb{Z}_4$ TP. The phase transition along the path $\theta_2 = \theta_1 - (\theta_1^T - \theta_2^T)$, marked by the black line in Fig. 4.21c, is a first-order phase transition (Fig. 4.22). On the other hand, the phase transitions from $\mathbb{Z}_4 \boxtimes \mathbb{Z}_2$ DS to $D(\mathbb{Z}_4)$ QD across the horizontal axis and between $\mathbb{Z}_4 \boxtimes \mathbb{Z}_2$ DS and $\mathbb{Z}_2 \boxtimes \mathbb{Z}_2$ TP across the vertical axis lie in the Ising universality class.

4.6 Summary

Condensation and confinement fraction of anyons can be used as order parameters to extract the universal features of topological phase transitions. Different patterns of symmetry breaking in the fixed points of the transfer operator can be used to label distinct topological phases. Furthermore, the techniques developed within the framework

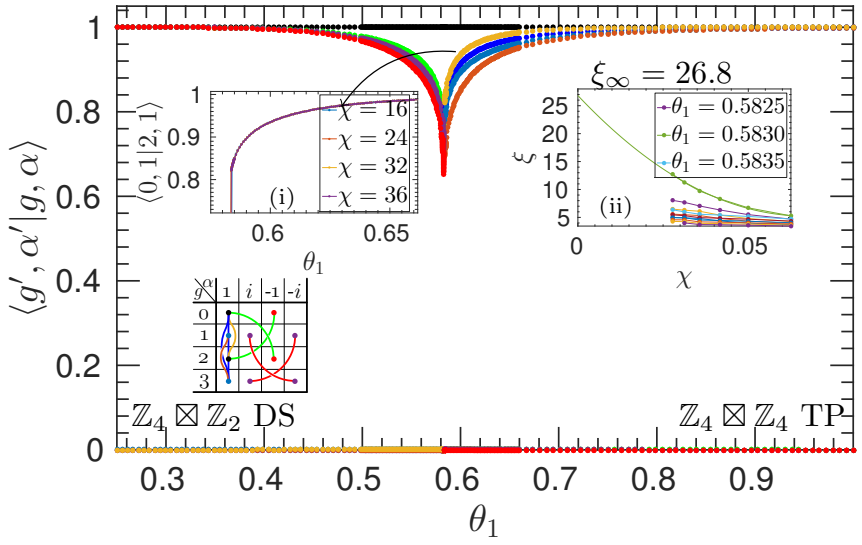

FIGURE 4.22: Phase transition between DS model and $\mathbb{Z}_4 \boxtimes \mathbb{Z}_4$ TP phase across the black line in Fig. 4.21c. The main panel shows the behavior of different anyonic excitations. The sharp behavior of fractions in (i) is an indication of first-order phase transition. (ii) Shows that the correlation length remains finite at the transition point. Extrapolated value of the correlation length ξ at the transition point $\theta_1 = 0.5830$ has been obtained by a quadratic fit.

of tensor networks are robust enough to be reliably used for the study of quantum phase transitions between topologically trivial and non-trivial phases.

The phase diagram of $\mathbb{Z}_4$-invariant tensors exhibits some remarkable features. Aside from the occurrence of first-order phase transitions, we have observed a variety of continuous phase transitions which lie in different universality classes. Moreover, the boundaries of topological phases allow for phase transitions where the universality class of phase transition could change continuously.

The class of $\mathbb{Z}_4$-invariant tensors enables a unified approach to study the toric code and the double semion model. The phase boundaries of toric code and double semion model not only support the existence of continuous phase transition with different universality classes but also allow for the possibility of first-order phase transition.

Chapter 5

Toric code and double semion spin liquids

Magnetic behavior of the materials around us is an example of emergent phenomena which results from interactions among constituents of the system at the microscopic scale. One of the most fundamental but a recent insight is that the spin degrees of freedom are not only responsible for the existence of ordered magnetic phases like ferro and antiferromagnets, they can also give rise to exotic phases which defy our conventional explanations [74]. The unsatisfiability of constraints imposed by the interactions (or more precisely by the local antiferromagnetic interactions) leads to a *frustrated* quantum spin system. The presence of frustration (which happens to occur on geometries with high coordination numbers like triangular or kagome lattice) prohibits the appearance of local order among the spin degrees of freedom and the system retains a disordered state even at zero temperature. These phases are termed as *quantum spin liquids* [18], where the word liquid is meant to emphasize the invariance of the state under the actions of the group $SU(2)$ and lattice symmetries.

In this chapter, we study the spin liquid phases of the toric code and the double semion model in the framework of $\mathbb{Z}_N$-invariant tensors. The spin liquid phases of the two topological phases have the same ground state degeneracy on the torus and the same topological entanglement entropy correction, but the elementary excitations of the two model are different (i.e., they have different self and exchange statistics). In the gapped $\mathbb{Z}_2$ or the toric code spin liquid phase the anyonic character of spinons and visons is identified with the elementary particles of the toric code model. Similarly, in the double semion spin liquid phase, the anyonic features are determined by the fundamental particles of the double semion model. The motivation is to apply the insights from these studies in the later chapter and the future work to establish the gapped/gapless and

spin liquid nature (whether it is toric code or double semion) for the ground state of Heisenberg antiferromagnet on the kagome lattice conclusively.

This chapter has been organized as follows. Firstly in Sec. 5.1, we study the phase diagram of $\mathbb{Z}_2$ spin liquids on the kagome lattice using the formalism of $\mathbb{Z}_2$-invariant tensors with $SU(2)$ symmetry. In Sec. 5.2, we extend our studies from $\mathbb{Z}_2$ to $\mathbb{Z}_4$-invariant tensors which allows us to study the toric code and double semion spin liquids in a unified framework. We analyze the condensation/decondensation and confinement/deconfinement of anyons at the phase boundaries of the spin liquid phases. In Sec. 5.3, we present our findings regarding the entanglement properties of semionic resonating valence bond state which defines the most important point in the spin liquid phase of the double semion model.

5.1 Gapped $\mathbb{Z}_2$ spin liquids

We start this section by giving the $\mathbb{Z}_2$-invariant tensor network description of distinct phases. In the later subsections, we describe phase transitions and study the whole phase diagram.

5.1.1 Description of topologically distinct phases using $\mathbb{Z}_2$-invariant tensors

Topologically distinct phases which could be realized by $\mathbb{Z}_2$-invariant tensors in the presence of $SU(2)$ symmetry on the kagome lattice include the gapped $\mathbb{Z}_2$ spin liquid phase, the valence bond crystal phase, and the spinon doped trivial phase.

Gapped $\mathbb{Z}_2$ spin liquid phase

$\mathbb{Z}_2$ spin liquid (SL) is a disordered phase of the quantum system, and it enables the most straightforward realization of quantum matter with a non-trivial topological order in physical systems [75–77]. From the conceptual point of view, the simplest way to understand gapped $\mathbb{Z}_2$ SL on the kagome lattice is by analyzing the nearest neighbor resonating valence bond (RVB) wavefunction.

Resonating valence bond state as we have already discussed in Sec. 2.4.2 is a superposition of nearest neighbor singlet coverings. It was first used by Anderson [78] to study the properties of quantum spin systems. Here we slightly modify the earlier tensor network

construction of RVB wavefunction, in particular, the tensor E, so that later we could easily construct the tensor network of spinon doped phase.

$$E = \quad = \begin{cases} \sigma_{\beta_2\beta_3} & \beta_1 = 2 \\ \sigma_{\beta_3\beta_1} & \beta_2 = 2 \\ \sigma_{\beta_1\beta_2} & \beta_3 = 2 \\ 1 & \beta_1 = \beta_2 = \beta_3 = 2 \\ 0 & \text{otherwise,} \end{cases} \tag{5.1}$$

where $\beta_1, \beta_2, \beta_3 \in \{0, 1, 2, 3\}$, and the matrix $\sigma = \text{diag}\left(\frac{1}{\sqrt{2}}\begin{pmatrix} 0 & -1 \\ 1 & 0 \end{pmatrix},\ 0,\ 1\right)$. The 3-legged tensor E which is placed inside each triangle of the kagome should be interpreted as the sum of seven configurations.

- In three configurations, there is a singlet on one of the edges of the triangle and the third vertex is in the state $|2\rangle$.
- The three vertices of the triangle form a product state $|222\rangle$ in one configuration.
- And in the remaining three configurations there is a broken singlet embedded as $|33\rangle$ on one of the edges of the triangle and the third vertex is in the state $|2\rangle$.

The addition of the three configurations corresponding to the broken singlets in the definition of tensor E is not necessary for the tensor network construction of the RVB state but will be used for the tensor network construction of spinon doped phase. The definition of on-site tensor P_{RVB} remains the same as given in (2.16), i.e.

$$P_{\text{RVB}} = \quad = \begin{cases} \delta_{\beta_1 p} & \beta_2 = 2 \\ \delta_{\beta_2 p} & \beta_1 = 2 \\ 0 & \text{otherwise,} \end{cases} \tag{5.2}$$

where $p \in \{0, 1\}$.

Here we note that since on-site tensor P_{RVB} discard the information about source triangle of the singlet, and so the resulting coverings are not orthogonal. An approach to locally ensure the orthogonality of singlets in the tensor network framework was introduced in [17]. By attaching a label of the triangle with the spin at each site, we can obtain the coverings of dimers which are orthogonal to each other. Triangle labels can be attached

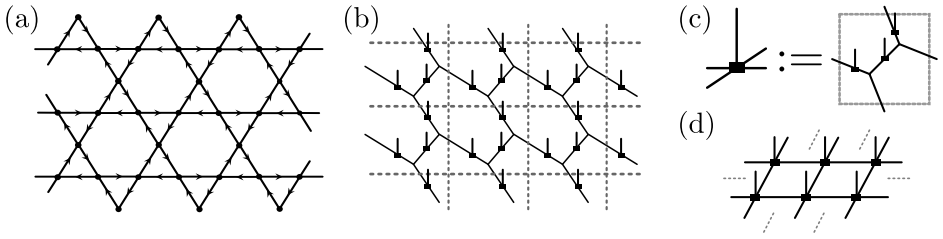

FIGURE 5.1: (a) The graphical representation of the kagome lattice. Each vertex represents a spin-1/2 particle. Arrowheads oriented in a clockwise fashion specify the direction of singlets. (b) We use the medial graph of the kagome (the hexagonal lattice) for the tensor network representation of RVB and the other states in this chapter. Vertices of the hexagonal lattice represent the 3-legged vertex tensor given in (5.1). Each dashed box represents a unit cell of the tensor network. (c) Translation invariant description is given by the unit tensor which has been obtained by collating the three physical indices as one index. (d) The resulting tensor network which has been obtained by using the blocking defined in (c).

with the spins by modifying the tensor in (5.2) as,

$$P_\perp = \beta_1 \overset{p}{\underset{}{|}} \overset{q}{\underset{}{|}} \beta_2 = \begin{cases} \delta_{\beta_1 p} & \beta_2 = 2,\ q = L \\ \delta_{\beta_2 p} & \beta_1 = 2,\ q = R \\ 0 & \text{otherwise} \end{cases} \tag{5.3}$$

where $p \in \{0, 1\}$ and $q \in \{L, R\}$. The resulting quantum state corresponds to the Rokhsar and Kivelson (RK) point of the quantum dimer model [79]. Furthermore we can describe an action which enables us to discard the triangle information from dimer continuously. By acting with $\multimap\!\!\circ\!\!-$ $:= |+\rangle\langle+| + \lambda|-\rangle\langle-|$, where $|\pm\rangle := \frac{1}{\sqrt{2}}(|L\rangle \pm |R\rangle)$, on the dimer index at each site, we can interpolate between the spaces of orthogonal dimer and non-orthogonal singlet coverings. The on-site tensor

$$P(\lambda) = \quad , \tag{5.4}$$

gives P_{RVB} and $P_\perp$ at $\lambda = 0$ and $\lambda = 1$ respectively and system remains in the gapped spin liquid phase for any value of λ between 0 and 1.

Valence bond crystal

The crystallization of singlet coverings in the spin liquid phase leads to a product state of singlets called valence bond crystal (VBC). Although the VBC state is $SU(2)$ invariant, it breaks the lattice symmetries. The smallest unit cell of VBC state with long-range order contains 6 sites on the kagome lattice (Fig. 5.2).

Tensor network representation of the valence bond crystal state can be obtained by defining tensors,

$$P_L = \beta_1 \overset{p}{\underset{\beta_2}{\leftarrow\blacksquare\leftarrow}} = \begin{cases} \delta_{\beta_1 p} & \beta_2 = 2 \\ 0 & \text{otherwise,} \end{cases}$$
$$P_R = \beta_1 \overset{p}{\underset{\beta_2}{\rightarrow\blacksquare\rightarrow}} = \begin{cases} \delta_{\beta_2 p} & \beta_1 = 2 \\ 0 & \text{otherwise,} \end{cases} \tag{5.5}$$

where the tensors P_L and P_R pick a singlet from the left and right pointing triangles respectively, and an arrowhead on the virtual index points to the center of the triangle which contains the singlet. It is important to note here that

$$P_{\text{RVB}} = P_L + P_R, \tag{5.6}$$

where P_{RVB} is defined in (5.2).

Now for the 6-site VBC configuration given in Fig. 5.2b, we can define the on-site tensors $\left\{P^{[i]}\right\}_{i=0}^{6}$ for the six sites in the unit cell as

$$\begin{aligned} P^{[a]} &:= P_L \\ P^{[b]} &:= P_R \end{aligned} \tag{5.7}$$

where $a \in \{1, 2\}$ and $b \in \{3, 4, 5, 6\}$.

Spinon doped phase

A spinon doped trivial phase which breaks the $SU(2)$ symmetry but preserves the lattice symmetries can be given by a product state of spinons. Tensor network representation of spinon doped phase in terms $\mathbb{Z}_2$-invariant tensors can be obtained by using terms corresponding to broken singlets in the vertex tensor E as defined in (5.1). By placing an on-site tensor P_{doped} at each physical site,

$$P_{\text{doped}} = \beta_1 \overset{p}{\underset{\beta_2}{\blacksquare}} = \begin{cases} 1 & \beta_1 = 2,\ \beta_2 = 3 \\ 1 & \beta_1 = 3,\ \beta_2 = 2 \\ 0 & \text{otherwise,} \end{cases} \tag{5.8}$$

we get a product state of $|+\rangle$. It is important to note here that the tensor network description of spinon doped phase like the previous constructions of RVB and VBC states is also $\mathbb{Z}_2$-invariant since the spinons have been added as broken singlets.

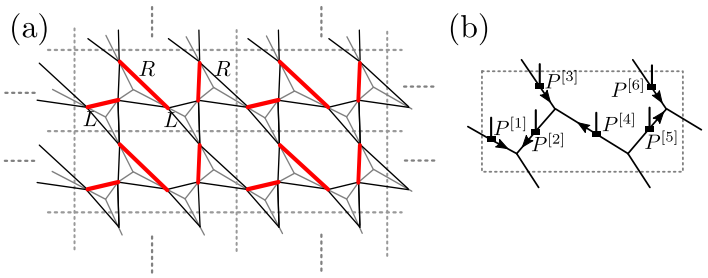

FIGURE 5.2: (a) Pictorial representation of 6-site VBC state on the kagome lattice. Red lines denote singlets. Labels 'L' and 'R' specify the left and right pointing triangles. Dashed boxes define the unit cell. (b) Unit cell for the translation invariant tensor network representation of 6-site VBC. Vertices of the hexagonal lattice represent the 3-legged vertex tensor as defined in (5.1).

5.1.2 Topological phase transitions

Now we describe an approach to induce phase transitions from the gapped SL to VBC and spinon doped phase along the simplest trajectories as prescribed by the linear interpolation of on-site tensors.

$\mathbb{Z}_2$ spin liquid and valence bond crystal

The on-site tensor P_L (P_R) picks a singlet from the left (right) pointing triangle, and as we noted earlier in (5.6), the tensor P_{RVB} can be written as a sum of P_L and P_R. This fact can be used to parametrize the on-site tensor in a way that breaks the lattice symmetries but can drive the system from topologically non-trivial SL phase to the VBC phase. We parametrize the on-site tensors as,

$$\begin{aligned} P^{[a]}(\theta_f) &:= P_L + (1-\theta_f)P_R \\ P^{[b]}(\theta_f) &:= (1-\theta_f)P_L + P_R, \end{aligned} \tag{5.9}$$

where $a \in \{1,2\}$ and $b \in \{3,4,5,6\}$.

Using the definition of vertex tensor as given in (5.1), and the on-site tensors $\left\{P^{[i]}(\theta_f)\right\}_{i=0}^{6}$ as parameterized above, we can interpolate between the SL and the VBC phase by freezing the superposition of all the singlet coverings to one covering. At $\theta_f = 0$, all the on-site tensors are equal to P_{RVB}, and the system realizes nearest neighbor RVB state, while at $\theta_f = 1$, the state of the system is given by the 6-site VBC.

$\mathbb{Z}_2$ spin liquid and spinon doped phase

The doping of the spin liquid state with broken singlets can drive a phase transition which leads to the trivial phase of polarized spins. It can be achieved by simply adding

the tensor P_{doped} as defined in (5.8) to the on-site tensor P_{RVB} as

$$P\left(\theta_d\right) = P_{\text{RVB}} + \frac{\theta_d}{\sqrt{2}} P_{\text{doped}}. \tag{5.10}$$

By tuning θ_d, we can drive the system between the gapped SL and spinon doped trivial phase.

Composition of different phase transitions

After describing the interpolations from $\mathbb{Z}_2$ SL to VBC and spinon doped trivial phases, here we compose these phase transitions to get an enriched phase diagram. The addition of doping term (5.8) to the on-site tensors in (5.9) gives a two-parameter family of wavefunctions,

$$P^{[i]}\left(\theta_f,\ \theta_d\right) = P^{[i]}\left(\theta_f\right) + \frac{\theta_d}{\sqrt{2}} P_{\text{doped}}, \tag{5.11}$$

where $i \in \{1, 2, ..., 6\}$. The extremal properties of the on-site tensors $\left\{P^{[i]}(\theta_f, \theta_d)\right\}_{i=0}^{6}$ are as follow

- At $(\theta_f, \theta_d) = (0, 0)$, $P^{[i]} = P_{\text{RVB}}\ \forall i$, and system is in the topologically non-trivial $\mathbb{Z}_2$ SL phase. It realizes nearest neighbor RVB sate. Since the topological structure of $\mathbb{Z}_2$ spin liquid is derived from the underlying theory of $D\left(\mathbb{Z}_2\right)$ quantum double namely the toric code model, the fundamental excitations $\{|vac\rangle, |spinon\rangle, |vison\rangle, |bound\ state\rangle\}$ (which can be identified with the pair of a conjugacy class and an irrep of $\mathbb{Z}_2$) are deconfined at the RVB point.

- At $(\theta_f, \theta_d) = (1, 0)$, the on-site tensors in (5.11) are equivalent to the description of on-site tensors in (5.9) and the system realizes a VBC state. The string operation on the entanglement degrees of the tensor network which leads to the creation of vison in the SL phase acts trivially on the vacuum in the VBC phase. This implies that the visons are condensed in the valence bond crystal phase. On the other hand, the action of operators which lead to the creation of spinon and the bound state of a spinon and a vison annihilate the vacuum, so the spinons and the bound states are confined in the VBC phase.

- At $(\theta_f, \theta_d) = (0, \infty)$, the P_{doped} term in (5.11) dominates the behavior of on-site tensors and the system realizes a product state where the spinons are condensed. On the other hand in contrast to the VBC, in the spinon doped phase, the visons and the bound states are confined.

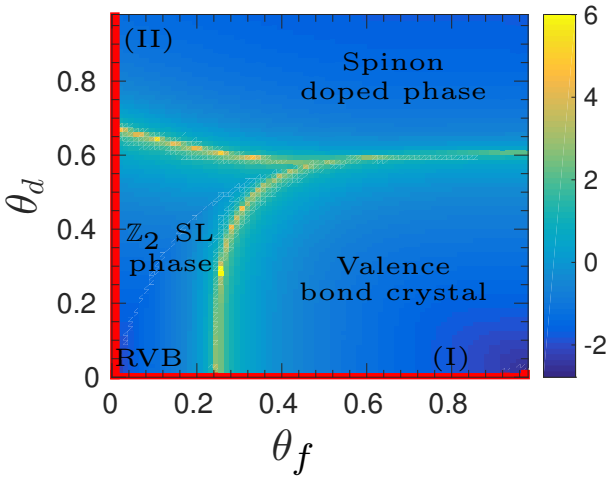

FIGURE 5.3: Log of the correlation length ξ of the system as the function of θ_f and θ_d. ξ has been computed by using the iMPS algorithm with bond dimension $\xi = 16$. The system breaks the $SU(2)$ and lattice symmetries at every point in the phase diagram except across the red lines (I) and (II), where only one of those two symmetries are broken.

5.1.3 Phase diagram of $\mathbb{Z}_2$ spin liquid

Tensor network descriptions of the phase transitions, as given above, between topologically non-trivial and trivial phases preserve the $\mathbb{Z}_2$-invariant structure of local tensors. The $\mathbb{Z}_2$-invariance of local tensors can be used to systematically study the condensation and confinement of anyonic excitations as we tune the system from one topological phase to another.

We start by analyzing the correlation length ξ of the system as the function of tuning variables (θ_f, θ_d) by using iMPS algorithm (Fig. 5.3) . The phase boundaries can be defined by the lines of diverging correlation length.

As the system is tuned from the $\mathbb{Z}_2$ SL to VBC phase at $\theta_d = 0$ (i.e., across the line (I) in Fig. 5.3), the system undergoes a phase transition. In the SL phase, the behavior of the phase transition in the critical regime is determined by the correlation length which corresponds to the condensation of vison. On the other hand near the critical point in the VBC phase, the dominant contribution to the correlation length comes from the deconfinement of spinons (Fig. 5.4a).

Similarly, the phase transition between $\mathbb{Z}_2$ SL and spinon doped phase at $\theta_f = 0$ (i.e., across the line (II) in Fig. 5.3) is driven by the condensation of spinons. In the vicinity of phase transition in the SL phase, the largest correlation length is identified with the condensation of spinons. The correlation length which corresponds to the deconfinement

of visons determine the behavior of the system in the critical regime of the spinon doped phase (Fig. 5.4b).

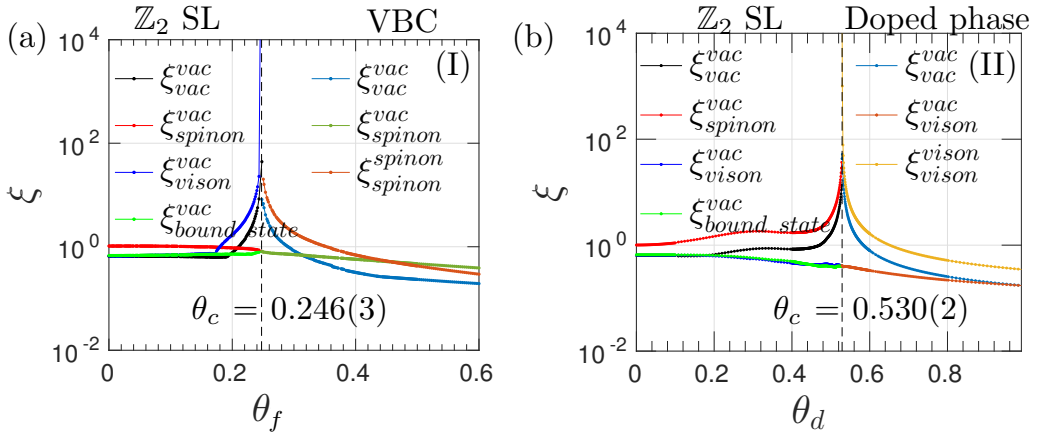

FIGURE 5.4: (a) Correlation length of anyonic excitations for the phase transitions across the lines marked as (I) and (II) in Fig. 5.3. Correlation lengths have been computed from the fixed points of the transfer operator by using the iMPS algorithm.

It is important to be emphasized here that since the topological structure of $\mathbb{Z}_2$ spin liquid is derived from the underlying theory of $D(\mathbb{Z}_2)$ quantum double namely the toric code model [7], the phase transitions we have described are characterized by the spontaneous symmetry breaking in the fixed points of the transfer operator and topologically trivial and non-trivial phases of $\mathbb{Z}_2$ theory realizes different patterns of symmetry breaking in the fixed points of the transfer operator. In the $\mathbb{Z}_2$ SL phase, the fixed points of the transfer operator have $\mathbb{Z}_2 \boxtimes \mathbb{Z}_1$ symmetry. On the other hand, in VBC (spinon doped) trivial phase the fixed points of the transfer operator enhance (break) the symmetry to $\mathbb{Z}_2 \boxtimes \mathbb{Z}_2$ ($\mathbb{Z}_1 \boxtimes \mathbb{Z}_1$).

The quantum states realized by the on-site tensors in (5.11) for $(\theta_f, \theta_d) \neq 0$ break either the $SU(2)$, the lattice, or both symmetries. The order parameters corresponding to these symmetries do not encounter any critical behavior as the system undergoes different topological phase transitions (5.5). So the phase transitions are indeed driven by the condensation of anyons.

5.2 Spin liquid phases of toric code and double semion model

The canonical way to describe toric code (TC) and double semion (DS) model is by using the language of loop patterns [64]. We begin this section by giving the $\mathbb{Z}_4$-invariant tensor network of TC and DS model where the physical indices have the interpretation of closed loop patterns on the hexagonal lattice. Furthermore, there exists a map with

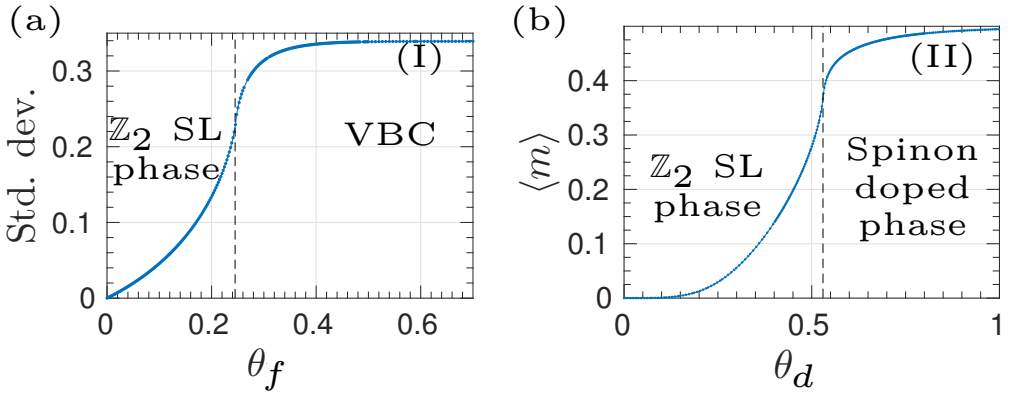

FIGURE 5.5: Phase transitions across the lines marked as (I) and (II) in Fig. 5.3. (a) Standard deviation of energy per edge for the Heisenberg interaction $\boldsymbol{S}_i.\boldsymbol{S}_j$ for the 6-site unit cell (Fig. 5.2). (b) Mean value of magnetization per site.

local action $M_1 \otimes M_2$ to associate each loop patterns on the honeycomb lattice to singlet coverings on the kagome lattice via arrow representation [80, 81]. By applying the map to the $\mathbb{Z}_4$-invariant local tensors, we get the descriptions of TC and DS SLs. In the later subsection we present our findings regarding different anyonic fractions and map out the phase diagram of spin liquids.

5.2.1 Description of topologically distinct phases using $\mathbb{Z}_4$-invariant tensors

The most important example of a spin liquid state with the toric code topological order is the RVB state. Similarly, we can also construct a spin liquid state with double semion topological order and call it semionic resonating valence bond state [65]. The constructions of TC and DS models using $\mathbb{Z}_4$-invariant tensors that are motivated by the symmetry properties of the boundary phases are given in Sec. 4.3. Here, we again start by defining the on-site tensor of $D(\mathbb{Z}_4)$ quantum double to get the representation in the language of loop patterns (see Sec. 4.1.6).

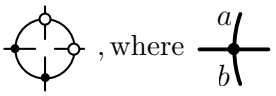

(5.12)

and $a, b \in \{0, 1, 2, 3\}$. The indices on the inside (outside) of the ring correspond to the physical (virtual) degrees of freedom. To later get the closed loop patterns on the physical indices, we assume $X := \sum_{i=0}^{3} i^g |g\rangle\langle g|$ is the generator of $\mathbb{Z}_4$ with diagonal representation. Now we apply the following deformation (green MPO) on the physical

indices of the on-site tensor in (5.12).

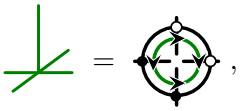

$$= \begin{cases} (|0\rangle_v + |2\rangle_v)\,\langle 0|_p & a=0,\ b=0 \\ (|0\rangle_v + C|2\rangle_v)\,\langle 0|_p & a=1,\ b=1 \\ (|1\rangle_v + |3\rangle_v)\,\langle 1|_p & a=0,\ b=1 \\ (|1\rangle_v + C|3\rangle_v)\,\langle 1|_p & a=1,\ b=0 \end{cases}, \tag{5.13}$$

Arrowhead points in the direction of index b. Subscripts p (v) indicate the physical (virtual) indices on the inside (outside) of the ring. The dimension of each local physical space is 2, and by interpreting the basis vectors $|0\rangle$ and $|1\rangle$ as having a vacuum and string on the physical site, we get the superpositions of closed loop patterns.

The on-site tensor in (5.13) is parametrized by a complex variable C. And for every value of C, the description only allow patterns of closed loops on the physical level. The on-site tensor in (5.13) realizes the following quantum states.

- At $C = -1$, the on-site tensor realizes the TC model where the boundary phase has $\mathbb{Z}_2 \boxtimes \mathbb{Z}_1$ symmetry. Locally the on-site tensor in (5.13) is equal to the sum of configurations in Fig. 4.6. The description gives us a TC on the physical level from two copies of the TC on the virtual level.
- At $C = 1$, the on-site tensor realizes DS model with the boundary phase having $\mathbb{Z}_4 \boxtimes \mathbb{Z}_2$ symmetry. Furthermore, the on-site tensor is equal to the sum of string configurations in Fig. 4.7.
- At $C = 0$, the on-site tensor realizes a topologically trivial phase where the boundary phase has $\mathbb{Z}_2 \boxtimes \mathbb{Z}_2$ symmetry.

Now, to get the spin liquid state, we need a map between loop patterns and the singlet coverings. The map can be obtained via arrow representation of loop patterns and by fixing a reference configuration [65, 80, 82]. Pictorially the on-site tensor can be written as

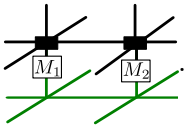

(5.14)

The green component is defined in (5.13) and $M_1 \otimes M_2$ is the local action of the map between loop patterns and singlet coverings on a $(3+3)$-site cell. The black tensor has been defined by modifying the definition of on-site tensor in (5.3).

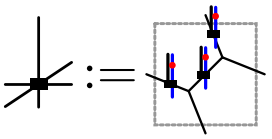
, where 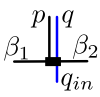
$$= \begin{cases} \delta_{\beta_1 p} & \beta_2 = 2,\ q_{in} = q = L \\ \delta_{\beta_2 p} & \beta_1 = 2,\ q_{in} = q = R \\ 0 & \text{otherwise} \end{cases}, \tag{5.15}$$

 $:= |+\rangle\langle+| + \lambda|-\rangle\langle-|$, and $|\pm\rangle := \frac{1}{\sqrt{2}}(|L\rangle \pm |R\rangle)$.

5.2.2 Phase diagram of the toric code and double semion spin liquids

Now we examine the behavior of the phase diagram of quantum states realized by on-site tensor in (5.14) for the possible values of C by analyzing the behavior of anyonic fractions. To map out the phase diagram, we consider the following three fractions.

1. In the toric code phase, the anyon $|0, i\rangle$ is identified with the charged anyon e. The quantity $\langle 0, i|0, i\rangle$ measures the deconfinement of e.

2. The overlap $\langle 1, i|1, i\rangle$ quantifies the deconfinement of semion in the double semion phase. It should be noted that the semions are confined in the toric code and trivial phase.

3. The overlap $\langle 0, 1|0, 2\rangle$, characterizes the condensation of anyon $|0, 2\rangle$ and non-zero only in $\mathbb{Z}_2 \boxtimes \mathbb{Z}_2$ trivial phase.

The three fractions as the function of C are shown in Fig. 5.6 and they are sufficient to label the distinct topological phases. The on-site tensor in (5.14) realizes quantum states of dimer coverings (Fig. 5.6a) at $\lambda = 1$ and singlet coverings (Fig. 5.6b) at $\lambda = 0$. The qualitative features of these two phase diagrams are similar. The TC spin liquid is separated from the DS spin liquid by an intermediate valence bond crystal phase. The behavior of all the non-zero anyonic fractions across the line marked as (II) in Fig. 5.6 are shown in Fig. 5.7.

5.3 Entanglement properties of double semion spin liquid

As we discussed earlier in Sec. 3.1.2, the entanglement spectrum, and boundary Hamiltonians contain useful information to characterize the topological order of the given phase.

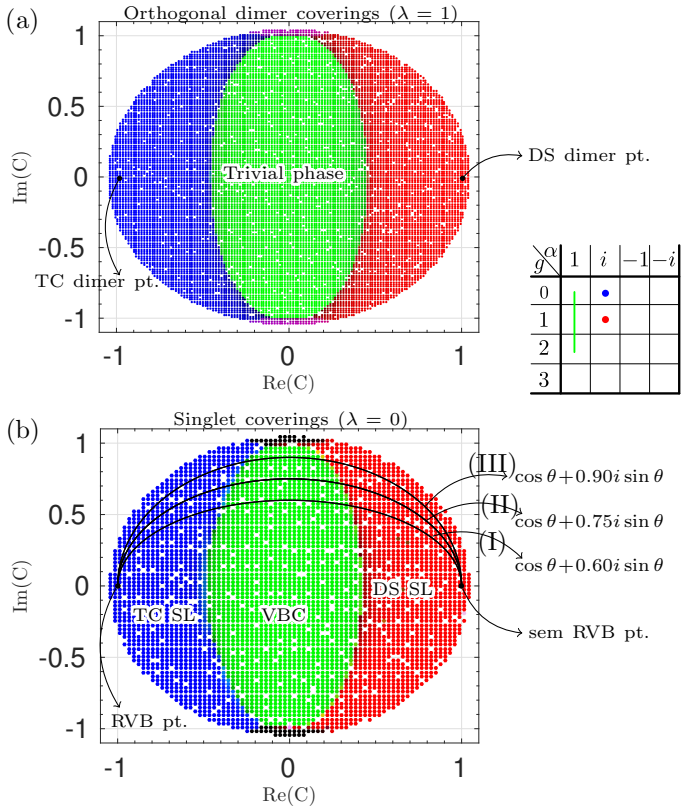

FIGURE 5.6: Overlaps of anyonic excitation $\langle 1, i|1, i\rangle$, $\langle 0, 1|2, 1\rangle$, and $\langle 0, i|0, i\rangle$ are labeled by the red, green and blue colors respectively as also indicated in the anyon table. (a) A projection of the phase diagram of orthogonal dimer coverings on the complex plane C containing toric code and double semion point at $C = -1$ and at $C = 1$ respectively. (b) Phase diagram of spin liquids with RVB and semionic RVB points. The behavior of the system along the three trajectories labeled as (I), (II), and (III) have been examined in greater detail in the next chapter (see Figs. 6.7,6.8).

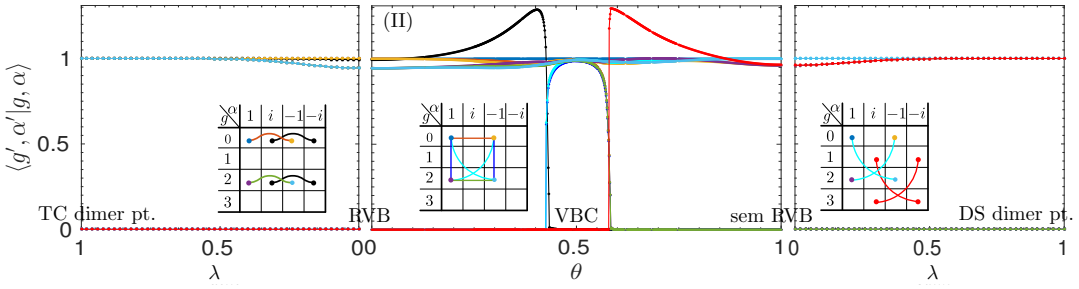

FIGURE 5.7: The middle plot shows the behavior of anyonic excitation across the path labeled as (II) in Fig. 5.6. The path (II) connects the normal RVB state to semionic RVB state and the phase transition along the path between toric code, and the double semion spin liquid is not direct but via an intermediate topologically trivial phase of valence bond crystal. The leftmost plot shows the behavior of anyonic fractions along the path between toric code and RVB state. The rightmost plot connect semionic RVB state with the double semion model.

5.3.1 Entanglement spectrum

Topological correction to the entanglement entropy is the same for the ground states in the TC and DS spin liquids but their entanglement spectrum shows different features. Here, we compute the entanglement spectrum for the different points along the interpolation between semionic RVB and semionic dimer states in the spin liquid phase of the DS model (Fig. 5.8). Furthermore, we label each of the eigenstate with the spin quantum number S. The eigenstates in the bosonic (semionic) sectors exhibit only the integer (half-integer) spin. A defining feature of the entanglement spectrum of the DS spin liquid is that in the half integer spin sector the minimum of the dispersion is at $k = \pm\pi/2$ which is different from the TC spin where the minimum is at $k = 0$ [16, 17, 83].

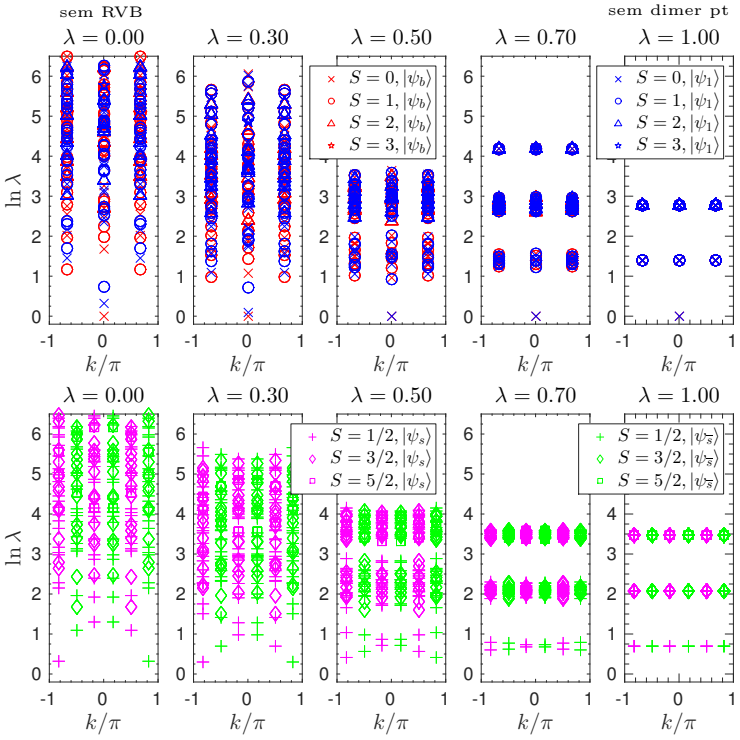

FIGURE 5.8: Entanglement spectrum of four topologically degenerate ground states at different points in the double spin liquid computed on an infinite cylinder with perimeter $N_v = 6$. The endpoints correspond to the semionic RVB ($\lambda = 0$) and semionic dimer state ($\lambda = 1$). The top (bottom) panel corresponds to the bosonic (semionic) ground states.

5.3.2 Boundary Hamiltonians

Now we briefly present our results for the boundary Hamiltonian of semionic RVB state in the four topological sectors, i.e., vacuum, semion, anti-semion, and boson. We discussed boundary Hamiltonian in Sec. 3.1.2 and it has been defined as $H_b :=$

$-\ln(\sqrt{\sigma_L}\sigma_R\sqrt{\sigma_L})$, where $\sqrt{\sigma_L}\sigma_R\sqrt{\sigma_L}$ is related to the reduced density matrix ρ_A of the quantum state $|\psi\rangle$ on an infinite cylinder with the finite perimeter N_v.

To be able to compute the boundary Hamiltonian on an infinite cylinder with perimeter $N_v = 6$ we use the tensor network description of semionic RVB state from [65, 82]. Pictorially the segment of the tensor network of $|\psi_{\text{semRVB}}\rangle$ can be written as,

$|\psi_{\text{semRVB}}\rangle$ =

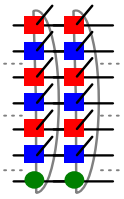

(5.16)

The red and blue squares form a unit tensor of the tensor network. Green circles indicate color tensors that are necessary for the weighting factor of singlet coverings. Before we describe the boundary Hamiltonians, for the purpose of convenience, we define two operators and set the notation for basis operators that act on two-and three-level systems. Let

$$\boldsymbol{P} := \left(\mathbb{I} + T + T^2 + T^3 + T^4 + T^5\right)$$

and

$$\boldsymbol{Q} := \left(\mathbb{I} + T^2 + T^4\right).$$

Where T is the generator of translation that does a circular shift on the cylinder in the vertical direction. And let

$$\left\{\sigma_I = \begin{pmatrix} 1 & 0 \\ 0 & 1 \end{pmatrix},\ \sigma_x = \begin{pmatrix} 0 & 1 \\ 1 & 0 \end{pmatrix},\ \sigma_y = \begin{pmatrix} 0 & i \\ -i & 0 \end{pmatrix},\ \sigma_z = \begin{pmatrix} 1 & 0 \\ 0 & -1 \end{pmatrix}\right\}$$

be the set of spin-1/2 Pauli matrices which act on the color degrees (green indices) of the tensor network and we define

$$\begin{aligned} &\{x := \text{diag}\,(\sigma_x/2, 0)\,,\ y := \text{diag}\,(\sigma_y/2, 0)\,,\ z := \text{diag}\,(\sigma_z/2, 0) \\ &\ p := |0\rangle\langle 2|,\ p^\dagger,\ m := |1\rangle\langle 2|,\ m^\dagger, \\ &D := \text{diag}(1, 1, -2)/6,\ I = \text{diag}(1, 1, 1)/3\} \end{aligned}$$

to be the set of basis matrices for the 3-level (blue and red) indices of the tensor network in (5.16).

Using the definition of projectors $\boldsymbol{P}$ and $\boldsymbol{Q}$ and the definitions of basis matrices for the 2- and 3-level systems, the computed boundary Hamiltonian of $|\psi_{\text{semRVB}}\rangle$ in the vacuum

sector is

$$
\begin{aligned}
H_b^{\text{vac.}} =& 3.56\sigma_I - 1.12\sigma_z + \\
& 0.15\left(\boldsymbol{Q}\left(D_1\right)\right)\sigma_I + 0.15\left(\boldsymbol{Q}\left(D_2\right)\right)\sigma_z + 0.13\left(\boldsymbol{Q}\left(D_1\right)\right)\sigma_z + 0.11 D_6\sigma_I + \\
& 0.49\left(\boldsymbol{Q}\left(D_2D_4 + D_2D_5\right)\right)\sigma_z + 0.48\left(\boldsymbol{Q}\left(D_4D_5 + D_5D_6 + D_1D_5\right)\sigma_z\right) + \\
& 0.29\left(ip_3m_4 - im_3p_4 + ip_5m_6 - im_5p_6 + h.c\right)\sigma_x + 0.28\left(m_4p_5 - p_4m_5 + h.c\right)\sigma_y \\
& - 0.25\left(\boldsymbol{Q}\left(p_1^\dagger p_2 + m_1^\dagger m_2 + h.c\right)\right)\sigma_I - 0.22\left(m_1m_6^\dagger + m_2^\dagger m_3 + p_1p_6^\dagger + p_2p_3^\dagger + h.c\right)\sigma_I \\
& - 0.22\left(p_4p_5^\dagger + m_4m_5^\dagger + h.c\right)\sigma_z + 0.18\left(m_1p_2 - p_1m_2 + h.c\right)\sigma_y + 0.15\left(\boldsymbol{Q}\left(p_1p_2^\dagger + m_1m_2^\dagger + h.c\right)\right)\sigma_z + \\
& 0.13\left(p_4^\dagger p_5 + m_4m_5^\dagger + h.c\right)\sigma_I + 0.13\left(p_1^\dagger p_6 + p_2p_3^\dagger + m_1m_6^\dagger + m_2m_3^\dagger + h.c\right)\sigma_z + \\
& 0.19 D_1D_3D_5\sigma_z + 0.18\left(\boldsymbol{Q}\left(D_1D_3D_6\right)\right)\sigma_z + 0.18\left(im_1D_5p_6 + ip_1D_5m_6 + im_2p_3D_4 - ip_2m_3D_4 + h.c\right)\sigma_x + \\
& 0.18\left(\boldsymbol{Q}\left(D_1D_3D_4 + D_1D_5D_6 + D_2D_3D_6 + D_3D_4D_6\right)\right)\sigma_z + 0.18\left(\boldsymbol{Q}\left(D_2D_3D_4\right)\right)\sigma_z + 0.17 D_2D_4D_6\sigma_z + \\
& 0.13\left(ip_1m_2D_3D_4 + ip_1m_2D_5D_6 - im_1p_2D_3D_4 - im_1p_2D_5D_6 + h.c\right)\sigma_x + \\
& 0.17\left(\boldsymbol{Q}\left(D_1D_2D_4D_5D_6\right)\right)\sigma_I + 0.16\left(\left(D_1D_2D_3D_4D_5\right)\right)\sigma_I + 0.12\left(\boldsymbol{P}\left(D_1D_2D_3D_5D_6\right)\right)\sigma_z + \\
& 0.28 D_1D_2D_3D_4D_5D_6\sigma_I + ...
\end{aligned}
\tag{5.17}
$$

Similarly, the boundary Hamiltonians in the semionic sectors are

$$
\begin{aligned}
H_b^{\text{sem.}} = H_b^{\overline{\text{sem.}}} =& \\
& 3.54\sigma_I - 0.73\sigma_z \\
& - 0.80\left(\boldsymbol{P}D_1\right)\sigma_z + 0.12\left(\boldsymbol{Q}\left(D_1\right)\right)\sigma_I + \\
& 0.28\left(ip_3m_4 - im_3p_4 - ip_5m_6 + im_5p_6 + h.c\right)\sigma_x + 0.27\left(im_4p_5 - ip_4m_5 + h.c\right)\sigma_y \\
& 0.26\left(\boldsymbol{Q}\left(m_1^\dagger m_2 - m_1m_2^\dagger + p_1^\dagger p_2 - p_1p_2^\dagger\right)\right)\sigma_I + 0.22\left(ip_4^\dagger p_5 - im_4m_5^\dagger + h.c\right)\sigma_z + \\
& 0.22\left(p_2^\dagger p_3 - p_2p_3^\dagger + p_1p_6^\dagger - p_1^\dagger p_6 + m_2^\dagger m_3 - m_2m_3^\dagger + m_1m_6^\dagger - m_1^\dagger m_6\right)\sigma_I + \\
& 0.17\left(m_3p_4 - m_3^\dagger p_4^\dagger + m_5p_6 - m_5^\dagger p_6^\dagger + p_3m_4 - p_3^\dagger m_4^\dagger + p_5m_6 + p_5^\dagger m_6^\dagger\right)\sigma_y + \\
& 0.17\left(-p_4m_5 + p_4^\dagger m_5^\dagger - m_4p_5 + m_4^\dagger p_5^\dagger\right)\sigma_x + 0.14\left(-m_2p_3 + m_2^\dagger p_3^\dagger + p_2m_3 - p_2^\dagger m_3^\dagger\right)\sigma_y + \\
& 0.14\left(im_1p_6 + ip_1m_6 + h.c\right)\sigma_y - 0.13\left(\boldsymbol{Q}\left(D_1D_3\right)\right)\sigma_z - 0.11\left(\boldsymbol{Q}\left(D_2D_5 + D_2D_3 + D_1D_2\right)\right)\sigma_z + \\
& 0.26 D_2D_4D_6\sigma_z + 0.25\left(\boldsymbol{Q}\left(D_1D_2D_4 + D_2D_4D_5 + D_4D_5D_6\right)\right)\sigma_z + \\
& 0.24\left(\boldsymbol{Q}\left(D_1D_4D_5 + D_1D_3D_4 + D_3D_4D_5\right)\right)\sigma_z + 0.23 D_1D_3D_5\sigma_z + \\
& 0.18\left(ip_1D_5m_6 - im_1D_5p_6 - im_2p_3D_4 + ip_2m_3D_4 + h.c\right)\sigma_x + \\
& 0.17\left(\boldsymbol{Q}\left(D_1D_3D_5D_6\right)\right)\sigma_z + 0.16\left(\boldsymbol{Q}\left(D_2D_3D_5D_6 + D_1D_2D_3D_6 + D_1D_2D_5D_6 + D_2D_3D_4D_6\right)\right)\sigma_z \\
& 0.13\left(-ip_1m_2D_3D_4 + im_1p_2D_3D_4 + ip_1m_2D_5D_6 - im_1p_2D_5D_6\right)\sigma_x \\
& 0.17\left(\boldsymbol{Q}\left(D_1D_2D_4D_5D_6\right)\right)\sigma_I - 0.16\left(\boldsymbol{Q}\left(D_1D_2D_3D_4D_5\right)\right)\sigma_I + \\
& - 0.28 D_1D_2D_3D_4D_5D_6\sigma_I ...
\end{aligned}
\tag{5.18}
$$

And for the bosonic sector

$$
\begin{aligned}
H_b^{\text{bos.}} = {} & 3.56\sigma_I - 1.12\sigma_z + \\
& 0.15\left(\boldsymbol{Q}\left(D_1\right)\right)\sigma_I + 0.15\left(\boldsymbol{Q}\left(D_2\right)\right)\sigma_z + 0.13\left(\boldsymbol{Q}\left(D_1\right)\right)\sigma_z + 0.11 D_6\sigma_I + \\
& 0.49\left(\boldsymbol{Q}\left(D_2D_4 + D_2D_5\right)\right)\sigma_z + 0.48\left(\boldsymbol{Q}\left(D_2D_3 + D_3D_4 + D_3D_5\right)\right)\sigma_z + \\
& 0.29\left(ip_3m_4 + ip_5m_6 - im_3p_4 - im_5p_6 + h.c\right)\sigma_x + 0.28\left(p_4m_5 - m_4p_5 + h.c\right)\sigma_y \\
& - 0.22\left(m_1m_6^\dagger + m_2m_3^\dagger + p_2^\dagger p_3 + p_1^\dagger p_6\right)\sigma_I + 0.22\left(m_4m_5^\dagger + p_4^\dagger p_5\right)\sigma_z + \\
& 0.18\left(m_1p_2 - p_1m_2 + h.c\right)\sigma_y + 0.15\left(\boldsymbol{Q}\left(m_1m_2^\dagger + p_1p_2^\dagger + h.c\right)\right)\sigma_z \\
& - 0.13\left(m_4m_5^\dagger + p_4^\dagger p_5 + h.c\right)\sigma_I + 0.13\left(p_1p_6^\dagger + p_2p_3^\dagger + m_1^\dagger m_6 + m_2m_3^\dagger + h.c\right)\sigma_z + \\
& 0.19 D_1D_3D_5\sigma_z + 0.18\left(\boldsymbol{Q}\left(D_1D_3D_6\right)\right)\sigma_z + 0.18\left(ip_1D_5m_6 - im_1D_5p_6 + h.c\right)\sigma_x + \\
& 0.18\left(\boldsymbol{Q}\left(D_3D_5D_6\right)\right)\sigma_z + 0.18\left(ip_2m_3D_4 + im_2p_3D_4 + h.c\right)\sigma_x + \\
& 0.18\left(\boldsymbol{Q}\left(D_1D_5D_6 + D_1D_4D_6 + D_1D_2D_4\right)\right)\sigma_z + 0.18\left(\boldsymbol{Q}\left(D_1D_2D_6\right)\right)\sigma_z + 0.17 D_2D_4D_6\sigma_z \\
& - 0.25\left(\boldsymbol{Q}\left(p_1^\dagger p_2 m_1^\dagger m_2 + h.c\right)\right)\sigma_I + \\
& 0.13\left(im_1p_2D_3D_4 + ip_1^\dagger m_2^\dagger D_3D_4 + im_1p_2D_5D_6 + ip_1m_2D_5D_6 + h.c\right)\sigma_x + \\
& 0.17\left(\boldsymbol{Q}\left(D_2D_3D_4D_5D_6\right)\right)\sigma_I + 0.16\left(\boldsymbol{Q}\left(D_1D_2D_3D_4D_5\right)\right)\sigma_I + \\
& - 0.12\left(\boldsymbol{Q}\left(D_1D_2D_3D_5D_6 + D_1D_2D_4D_5D_6\right)\right)\sigma_z + \\
& 0.28 D_1D_2D_3D_4D_5D_6\sigma_I \ldots
\end{aligned}
\tag{5.19}
$$

We give the leading terms of the boundary Hamiltonian where the magnitude of the coefficients is greater than 0.1. The subscript numbers are the labels for the site where the operator acts non-trivially. The last operator acts on the color degrees of the tensor network. To be compact, we have omitted the presence of I in each term. The terms of the boundary Hamiltonians have been ordered by the number of non-trivial operators (i.e., first the one body terms, second the two body terms, and so on). Due to finite size effects, it is hard to say conclusively about the locality of boundary Hamiltonian. We observe the presence of three body terms that act non-trivially on the color degree of freedom and create local singlets. Furthermore, we also find the existence of spin up/down hopping terms in the boundary Hamiltonian. The coefficients of similar terms in four topological sectors are slightly different which is a manifestation of finite size effects.

5.4 Summary

The formalism of tensor network states and the framework of anyon condensation not only enable the study of topological phase transitions in $D\left(\mathbb{Z}_4\right)$ quantum doubles as we did in the previous chapter but this approach is robust enough to map the phase diagram

of $\mathbb{Z}_2$ spin liquid. Furthermore, we have presented in this chapter our preliminary findings regarding the spin liquid of the DS model using the framework of $\mathbb{Z}_4$-invariant tensors.

Chapter 6

Spin liquid ansatzes for the ground state of Heisenberg antiferromagnet

Our understanding of the nature of the ground state of the Heisenberg antiferromagnet (HAF) on the kagome lattice has evolved continuously over the period of last three decades. Although there is a growing consensus that the ground state of HAF is a gapped spin liquid with $\mathbb{Z}_2$ or toric code topological order [20, 21, 77]. But, the gapped and $\mathbb{Z}_2$ spin liquid nature of the ground state wavefunction are still not completely established [84, 85] and the recent studies in [86], and [87] suggest that the ground state wavefunction lies in a gapless spin liquid phase. Furthermore, the gapped spin liquid phase of the double semion model has also been proposed as a contender for the ground state of HAF on the kagome [65, 88, 89].

The difficulty of the HAF problem on the kagome has served as the benchmark for remarkable innovations in different numerical strategies such as density matrix renormalization group (DMRG). However, an essential side-effect of these approaches is the presence of an exceedingly large number of variables used to parametrized the variational manifold. The description of the ground state in terms of these parameters because of their vast number eludes our comprehension of the wavefunction. The goal of this chapter is to develop the description for the ground state of HAF with as few parameters as possible in the spin liquid phases of toric code and double semion model.

This chapter has been organized as follows. In Sec. 6.1 we develop two very simple (i.e., these ansatzes are parametrized by few variables) variational ansatzes for the ground state of HAF on the kagome lattice in the gapped $\mathbb{Z}_2$ (i.e., toric code) spin liquid phase.

In Sec. 6.2 we present our findings regarding a variational ansatz in the double semion spin liquid phase. Lastly in Sec. 6.3, we make a digression to a separate but important topic to analyze the geometric structure of reduced density matrices for the Heisenberg model on the square lattice.

6.1 Gapped $\mathbb{Z}_2$ spin liquid ansatzes for the ground state of HAF on the kagome lattice

In this section, we construct two ansatzes for finding the ground state of HAF on the kagome lattice. We give the tensor network description of the ansatzes and present our findings regarding the ground state energies and correlation lengths within the two variational manifolds.

6.1.1 Variational ansatz of resonating valence bond states with 3rd neighbor singlets

A good starting point, to construct a ground state wavefunction which lies in the gapped $\mathbb{Z}_2$ spin liquid phase, is to consider the resonating valence bond (RVB) state. RVB wavefunction preserves all the lattice symmetries, and it has been shown rigorously that the nearest neighbor RVB wavefunction on the kagome lattice exhibits the toric code topological order [16, 17].

RVB wavefunction is a linear superposition of 1st neighbor singlet coverings and has the energy density that is approximately -0.3931 for the Heisenberg interaction. The energy density of RVB state is fairly large compared to the results of DMRG computations, but it is important to note that the variational manifold in the case of DMRG is characterized by an extremely large number of variables.

We show here that a simple modification in the tensor network description of RVB state allows for 3rd neighbor singlets in the singlet covering. Furthermore, it is possible to weight singlet coverings appropriately depending on the presence of 3rd neighbor singlets (Fig. 6.1a). The resulting ansatz parametrized by only one variational parameter allows for a considerably lower energy per site.

To describe the tensor network of the ansatz, we start by placing two copies of vertex tensor (see (2.15)) inside each triangle of the kagome. We modify the on-site tensor P

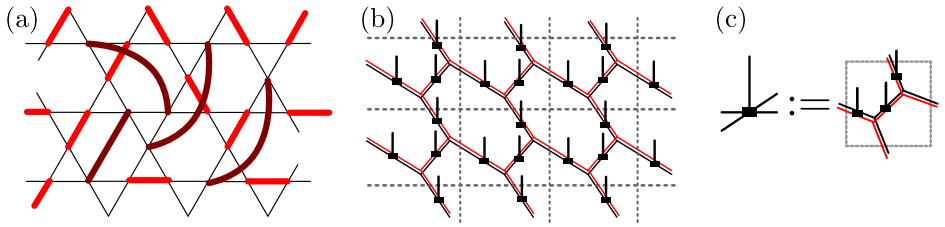

FIGURE 6.1: (a) A singlet covering containing 1st neighbor (light red) and 3rd neighbor (dark red) singlets on the kagome lattice. (b) Tensor network representation of the variational ansatz. Black and red lines represent two copies of vertex tensors. (c) Unit tensor containing three physical sites.

as follows,

$$P(\lambda) :=$$ 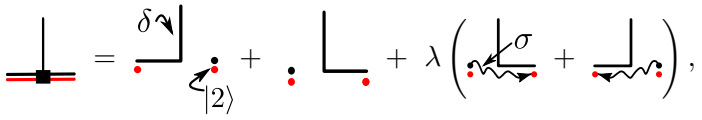 (6.1)

where $\delta = |0\rangle\langle 0| + |1\rangle\langle 1|$, and $\sigma = \frac{1}{\sqrt{2}}(|0\rangle\langle 1| - |1\rangle\langle 0|)$. Black and red virtual indices of on-site tensor $P(\lambda)$ contract with the two copies of the vertex tensor (Fig. 6.1(b,c)). The black lines with a bend on the RHS represent an identity map and project singlets from the virtual to the physical layer. Wiggly lines denote singlets, and the arrowheads indicate the orientation of the singlets.

The resulting family of states generated by the tensor network description in (6.1) as a function of variational parameter λ can be written as,

$$|\psi(\lambda)\rangle = \sum_{\sigma \in \mathcal{C}} \left(\lambda^2\right)^{k(\sigma)} |\sigma\rangle. \tag{6.2}$$

$\mathcal{C}$ is the set of singlet coverings such that each singlet covering contains only 1st and the 3rd neighbor singlets and

$$k(\sigma) = \text{No. of 3rd neighbor pairings in the singlet covering } \sigma.$$

The set of states generated by (6.2) preserves the lattice symmetries and the states are $SU(2)$-invariant. The results of optimization on the variational manifold as a function of λ using iMPS algorithm for different bond dimensions χ are shown in Fig. 6.2a. Furthermore, the smooth change in the value of correlation length ξ in Fig. 6.2b shows that the quantum states $|\psi(\lambda)\rangle$ for low values of λ also lie in the spin liquid phase with $\mathbb{Z}_2$ topological order.

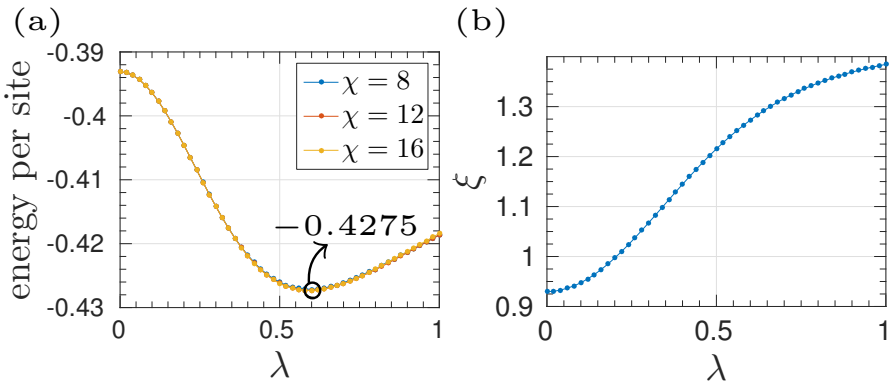

FIGURE 6.2: (a) Energy per site for the Heisenberg interaction $\boldsymbol{S}_i.\boldsymbol{S}_j$ as a function of λ. The value of energy per site is optimal at $\lambda = 0.59$. (b) Correlation length as the function of λ.

6.1.2 Simplex variational ansatz of resonating valence bond states with long range singlets

Here we describe the variational ansatz of simplex RVB states. The ansatz can be understood as an extension of the one proposed by Poiblanc et al. in [83]. The extension which has become possible due to the improvements in tensor network algorithms for infinite systems systematically allows for long-range singlets in the singlet covering.

The variational ansatz

Heisenberg Hamiltonian on the kagome lattice, $H = \sum_{\langle i,j \rangle} \mathbf{S}_i.\mathbf{S}_j$ can be expressed in terms of three body positive operators, $P^{3/2}$ which act on the kagome triangles. $P^{3/2}$ are projectors onto the spin-3/2 subspace of $\left(\frac{1}{2}\right)^{\otimes 3}$ and H in terms of $P^{3/2}$ takes the form,

$$H = \frac{3}{2} \sum_{(ijk)} \left(P^{3/2}_{(ijk)} - \frac{1}{2}\mathbb{I} \right). \tag{6.3}$$

The above description of Hamiltonian reduces our goal to the problem of finding the quantum state which lies in the null space of every projector. H is a frustrated Hamiltonian as any two projectors $P^{3/2}$ which act on the left- and right-pointing triangles of the kagome lattice and share a single vertex do not commute.

As in the case of the previous ansatz, the initial point of construction is the 1st neighbor RVB state. It has been pointed out in the earlier studies by Elser et al. in [80, 90] that a quarter of triangles in each covering are 'defective' (i.e., the covering does not assign any singlet to the triangle). The action of the projector $P^{3/2}$ on a singlet covering

is such that it annihilates the covering except in the case when it acts on a defective triangle. The action of $P^{3/2}$ on the defective triangles can be understood from the following decomposition,

$$P^{3/2} = \frac{1}{3}\Big(\mathbb{I} + R + R^2\Big), \tag{6.4}$$

where R is a generator of the cyclic group $\mathbb{Z}_3$, and its action on three spins produces a cyclic rotation. The action of $P^{3/2}$ on a defective triangle can be written pictorially as,

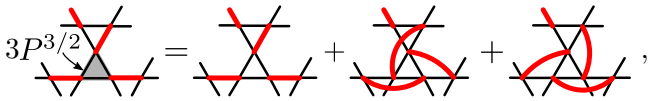

where red lines denote singlets, and the projector $P^{3/2}$ acts on the triangle shaded gray. The resulting state, after the application of $P^{3/2}$ projectors on the RVB wavefunction, contains coverings with next nearest neighbor singlets. And the repeated application of $P^{3/2}$ projectors effectively gives singlet coverings with long-range singlets.

Moreover, the variational ansatz of simplex RVB states developed by Poiblanc et al. [83] involves an application of operator

$$Q^{\triangleright}(\alpha) = \prod_{(ijk)\in\triangleright} \Big(\mathbb{I} - \alpha P^{3/2}_{ijk}\Big) \tag{6.5}$$

onto a tuned RVB wavefunction $|\psi_{\mathrm{RVB}}(\beta)\rangle$. $Q^{\triangleright}(\alpha)$ acts on the right pointing triangles and parameter β in the RVB wavefunction optimizes the probability of finding the left pointing triangles defective. An optimization with respect to only two variables α and β can give states $|Q^{\triangleright}(\alpha^\star)|\psi_{\mathrm{RVB}}(\beta^\star)\rangle$ in $\mathbb{Z}_2$ spin liquid phase with an energy density of -0.418 for Heisenberg Hamiltonian which is fairly close to the DMRG results.

A natural way to extend the simplex ansatz is to allow for the possibility of states with higher entanglement but within a variational manifold that is characterized by only a few parameters. That can be achieved by cascading the actions of Q operators onto the left and right pointing triangles. The resulting set of wavefunctions can be represented as

$$|\psi(\boldsymbol{\alpha})\rangle = Q^{\triangleright}(\alpha_n)...Q^{\triangleright}(\alpha_3)Q^{\triangleleft}(\alpha_2)Q^{\triangleright}(\alpha_1)\,|\psi_{\mathrm{RVB}}\rangle\,. \tag{6.6}$$

Here, we choose n to be odd because of a substantial advantage in numerical computations using tensor networks. The above ansatz allows for a state with a singlet covering where a singlet could extend up to n sites for a given n. Furthermore, by adjusting $\boldsymbol{\alpha} = (\alpha_1, \alpha_2, ...\alpha_n)$ it is possible to assign an appropriate weight to the singlet covering containing long range singlets. To be concrete, in the rest of this section, we study the family of wavefunctions in (6.6) for $n = 3$ and 5.

Tensor network description

Tensor network description of variational ansatz in (6.6) essentially involves the application of $\boldsymbol{Q}(\boldsymbol{\alpha}) = Q^{\triangleright}(\alpha_n)...Q^{\triangleright}(\alpha_3)Q^{\triangleleft}(\alpha_2)Q^{\triangleright}(\alpha_1)$ on the RVB wavefunction. $\boldsymbol{Q}(\boldsymbol{\alpha})$ can be represented as a tensor product operator or projected entangled pair operator (PEPO). The bond dimension of $\boldsymbol{Q}(\boldsymbol{\alpha})$ as a PEPO increases by a factor of four for every application of $Q^{\triangleleft}$ on the left pointing triangles of the kagome.

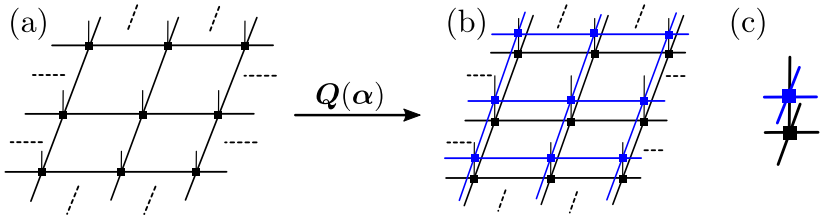

FIGURE 6.3: (a) Tensor network of resonating valence bond states. (b) Tensor network of resulting state obtained by the application of $\boldsymbol{Q}(\boldsymbol{\alpha})$ on the RVB wavefunction. Blue layer represents $\boldsymbol{Q}(\boldsymbol{\alpha})$ as a PEPO. (c) Unit tensor of simplex variational ansatz.

Results of numerical studies

Now we present our findings regarding variational optimization for simplex ansatz in (6.6). The results are given for the two implementations of $\boldsymbol{Q}(\boldsymbol{\alpha})$.

1. $\boldsymbol{Q}(\boldsymbol{\alpha}) = Q^{\triangleright}(\alpha_3)Q^{\triangleleft}(\alpha_2)Q^{\triangleright}(\alpha_1)$. The bond dimension of the PEPO is 4, the total bond dimension of resulting unit tensor (Fig. 6.3c) is $D = 3 \times 4 = 12$. The variational optimization has been performed for the exact tensor network description of the wavefunction.

2. $\boldsymbol{Q}(\boldsymbol{\alpha}) = Q^{\triangleright}(\alpha_5)..Q^{\triangleleft}(\alpha_2)Q^{\triangleright}(\alpha_1)$. The bond dimension of $\boldsymbol{Q}(\boldsymbol{\alpha})$ as PEPO is 16, and so the bond dimension of the unit tensor is $D = 3 \times 16 = 48$. The results have been computed for the approximate tensor network description of the wavefunction.

1. Exact tensor network description of the wavefunction

For $\boldsymbol{Q}(\boldsymbol{\alpha}) = Q^{\triangleright}(\alpha_3)Q^{\triangleleft}(\alpha_2)Q^{\triangleright}(\alpha_1)$, the variational ansatz, $|\psi(\boldsymbol{\alpha})\rangle = \boldsymbol{Q}(\boldsymbol{\alpha})\,|\psi_{\mathrm{RVB}}\rangle$, in general breaks the flip symmetry (which exchanges the left and right pointing triangles into each other) of the lattice. But the state with minimum energy state happens to restore that symmetry. The convex hull of the data points in Fig. 6.4a has a minimum at zero splitting. Due to the effects of finite size bond dimension used in the approximation of fixed points in the iMPS algorithm, there is small splitting in the energies on the

different edges of the unit tensor (Fig. 6.4b). The splitting goes away with increasing χ, and we get an energy per site of -0.4335(2).

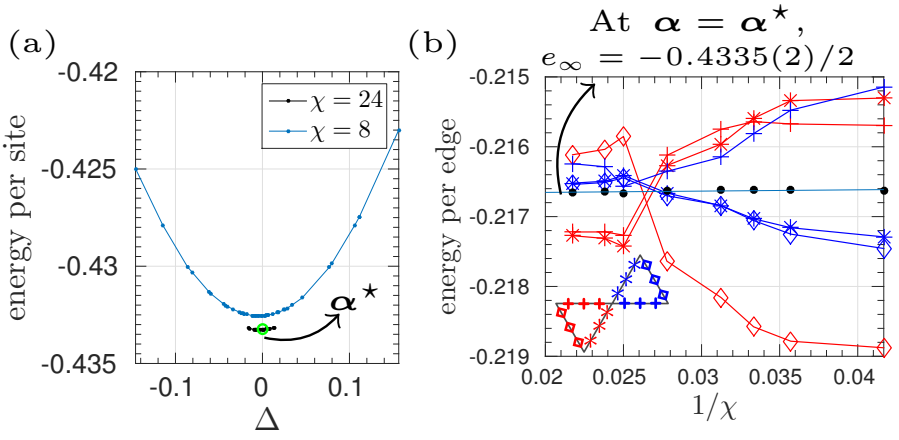

FIGURE 6.4: (a) Δ is the difference in the energy per site of left and right pointing triangles. The convex hull of the data points for optimization over three parameter manifold of states. $\boldsymbol{\alpha}^\star$ is the point of minimum energy and $\boldsymbol{\alpha}^\star = (0.9390,\ 0.8493,\ 0.3964)$ for $\chi = 24$. (b) Scaling of energy per edge vs the bond dimension χ. The legend of the curves has been defined by the markers on the edges of the triangles at the lower left corner.

Correlation lengths of anyonic excitations along the trajectory with endpoints consisting of RVB and optimal energy state remain finite. The behavior of correlation lengths shows that optimal energy point is in the $\mathbb{Z}_2$ spin liquid phase. And the anyons of $\mathbb{Z}_2$ spin liquid remain deconfined along the whole interpolation. The dominant correlation length along the whole interpolation is associated with the spinon (Fig. 6.4).

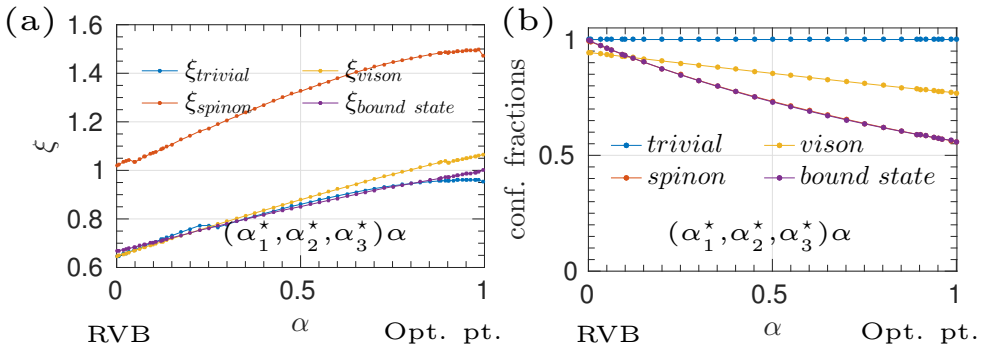

FIGURE 6.5: Computations have been made by using iMPS algorithm with bond dimension $\chi = 48$. (a) Correlation lengths of anyonic excitations of $\mathbb{Z}_2$ spin liquid as a function of α. At $\alpha = 0$, the system is in RVB state and at $\alpha = 1$ the system is in the optimal energy state. (b) Confinement fraction of anyonic excitations for different values of α.

2. Approximate tensor network description of the wavefunction

For $\boldsymbol{Q}(\boldsymbol{\alpha}) = Q^{\triangleright}(\alpha_5)..Q^{\triangleleft}(\alpha_2)Q^{\triangleright}(\alpha_1)$, we get an approximate PEPO representation of $\boldsymbol{Q}(\boldsymbol{\alpha})$ by using higher order singular value decomposition as in [91]. Pictorially,

, (6.7)

where $D = 16$ and $\tilde{D} = 4$ are the original and cut-off bond dimensions respectively. Original(approximated) PEPO are indicated by think(thin) blue tensor.

Again we see the restoration of flip symmetry at the optimal energy point from the convex hull of data points (Fig. 6.6a). The optimization over the variational manifold of five parameters gives an energy density of -0.4338(3) (Fig. 6.6b). Furthermore it can be shown that the point with optimal energy is in the $\mathbb{Z}_2$ spin liquid phase and it is gapped (Fig. 6.6(c,d)).

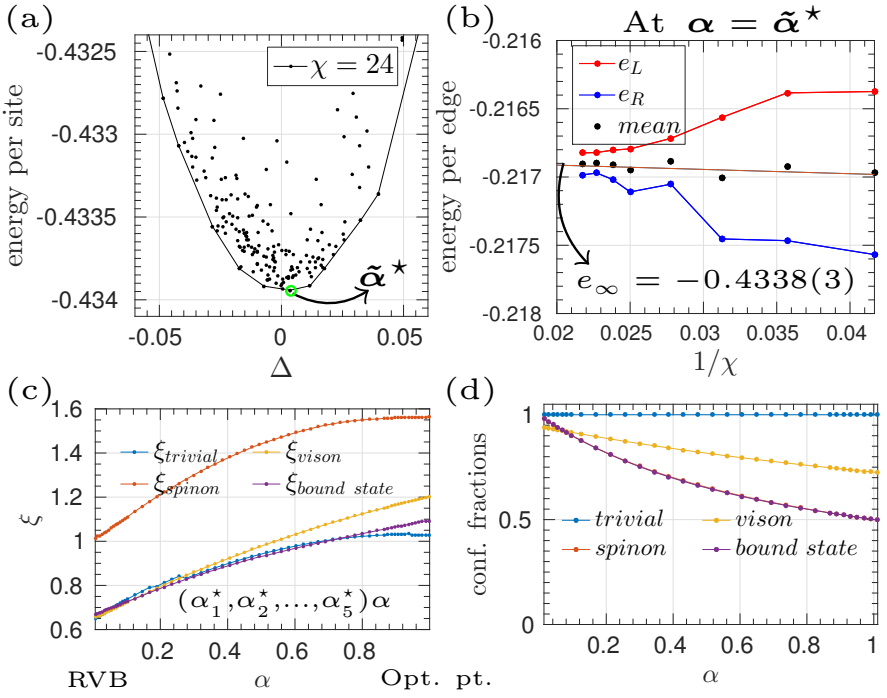

FIGURE 6.6: (a) Convex hull of the data points for optimization over the five parameter manifold of states. The value of $\tilde{\boldsymbol{\alpha}}^{\star} = (0.8992,\ 0.7343,\ 0.9147,\ 0.7568,\ 0.2987)$. (b) The scaling of mean energy per edge vs the bond dimension χ. (c,d) Anyon-anyon correlations lengths and the behavior of confinement fractions along the same trajectory between RVB and optimal energy point for $\chi = 48$.

6.2 Variational ansatz for the ground state of HAF in double semion spin liquid phase

Before we proceed to the description of variational ansatz, we analyze the behavior of Heisenberg interaction energy along a path which connects the spin liquids of toric code and double semion model.

6.2.1 Energy density between toric code and double semion spin liquids

We examine the interaction energy per edge for the Heisenberg Hamiltonian for the phase transition across the trajectory marked as (II) in Fig. 5.7b. The unit triangle contains 6-sites and comprise of 4 kagome triangles. Fig. 6.7 shows the continuous change in the interaction energy on the edges as the system is tuned from RVB state to semionic RVB state. At $\theta = 0$ (RVB point), the energy is the same on all the edges of the lattices, and the state preserves all the lattice symmetries. In the valence bond crystal phase the lattice symmetries are broken. Furthermore, at $\theta = 1$ (semionic RVB point), although the quantum state lies in a topologically non-trivial phase, it still breaks the lattice symmetries.

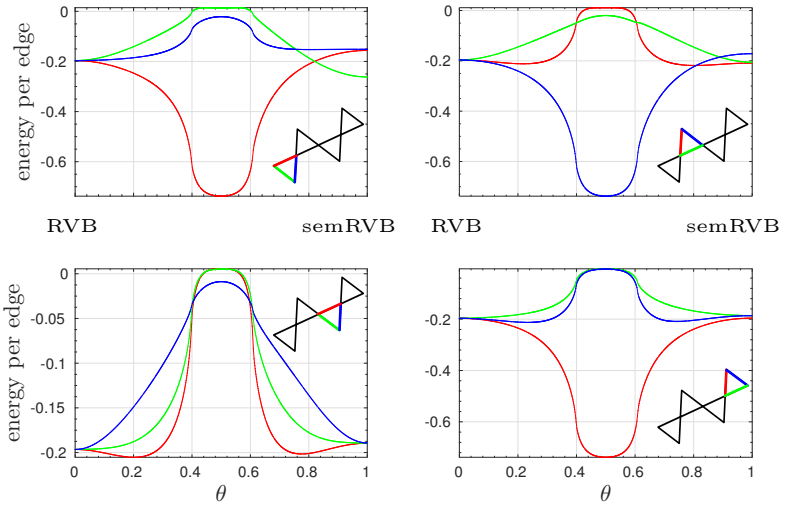

FIGURE 6.7: Energy of Heisenberg interaction for the different edges of the kagome lattice. The unit tensor contains $4 \times 3 = 12$ edges and four triangles of the kagome. Each subplot shows the behavior of interaction energy on the three edges of the triangle across (II) in Fig. 5.6.

The behavior of energy per site across the three trajectories in Fig. 5.6b indicate minimum energy at the RVB point. Moreover, the splitting in the energy of left and right hexagons is lowest for the RVB state (Fig. 6.8). Although the energy density of normal RVB is better compared to semionic RVB in the following subsection, we see that the simplex extension of semionic RVB gives better energy density.

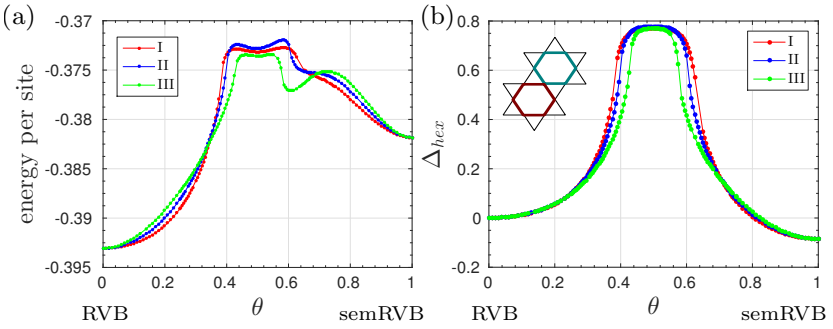

FIGURE 6.8: (a) Energy per site for the Heisenberg interaction across the three paths in Fig. 5.6b. (b) Splitting in the energy density of the two hexagons of the kagome.

6.2.2 Semionic simplex resonating valence bond states

We start by reviewing that the unit tensor in (5.14) provides the representation of semionic RVB state $|\psi_{\text{semRVB}}\rangle$ at $C = 1$. As in the case of (6.6), it is intuitive to consider the ansatz of the form

$$|\psi(\boldsymbol{\alpha})\rangle = Q^{\triangleright}(\alpha_n)...Q^{\triangleright}(\alpha_3)Q^{\triangleleft}(\alpha_2)Q^{\triangleright}(\alpha_1)\,|\psi_{\text{semRVB}}\rangle\,. \tag{6.8}$$

But the bond dimension for the translation invariant tensor network description of semionic RVB state is too large, and with the available numerical techniques, Q is restricted to be of the form $Q^{\triangleright}(\alpha_1)$. Here we apply the simplex ansatz originally developed for normal RVB states in [83]. The ansatz we consider has the form

$$|\psi(\alpha,\beta)\rangle = Q^{\triangleright}(\alpha)\,|\psi_{\text{semRVB}}(\beta)\rangle\,. \tag{6.9}$$

The parameter β in $|\psi_{\text{semRVB}}(\beta)\rangle$ optimizes the probability of left pointing triangles to be defective in the given singlet covering. The tensor network description of $|\psi_{\text{semRVB}}(\beta)\rangle$ is the same as the one given in (5.14) with the modified definition of vertex tensor for

the right pointing tirangles.

$$E'(\beta) = \overset{\beta_1}{\underset{\beta_2}{\succ}}\!\!-\!\!-_{\beta_3} = \begin{cases} \sigma_{\beta_2\beta_3} & \beta_1 = 2 \\ \sigma_{\beta_3\beta_1} & \beta_2 = 2 \\ \sigma_{\beta_1\beta_2} & \beta_3 = 2 \\ 1-\beta & \beta_1 = \beta_2 = \beta_3 = 2 \\ 0 & \text{otherwise,} \end{cases} \tag{6.10}$$

where $\beta_1, \beta_2, \beta_3 \in \{0, 1, 2\}$, and the matrix $\sigma = \mathrm{diag}\left(\frac{1}{\sqrt{2}}\begin{pmatrix} 0 & -1 \\ 1 & 0 \end{pmatrix}, 0\right)$.

The results for the variational optimization overs α and β in (6.9) are given in Fig. 6.9. The optimal energy density we get here is not good in comparison to the ones we got for variational ansatzes in (6.2) and (6.6). But it is important to note here the optimal energy density of semionic simplex RVB ansatz is better in comparison to the normal simplex RVB ansatz. The optimization over $Q^{\triangleright}(\alpha)\,|\psi_{\mathrm{RVB}}(\beta)\rangle$ gives an energy density of -0.418 [83].

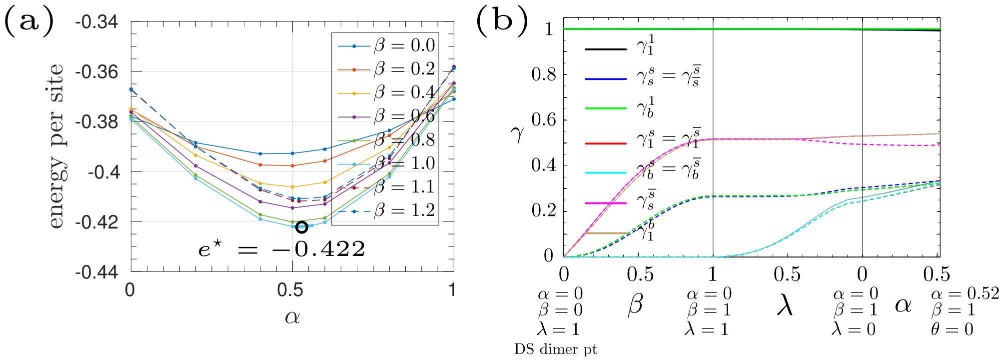

FIGURE 6.9: (a) Optimization of the two parameters variational ansatz of semionic simplex RVB states. The optimal energy point is at $\alpha = 0.52$ and $\beta = 1.0$. The extrapolated value of optimal energy density is -0.4196. (b) Interpolation between DS dimer point and semionic simplex optimal energy point. Eigenvalues γ of the transfer operator for the different anyonic sectors in the ket and bra layer of the infinite cylinder with $N_v = 6$. Largest (2nd largest) eigenvalues in different sectors are indicated by solid (dashed) lines.

6.3 Convex polytopes and HAF on the square lattice

In this section, we discuss a slightly different topic of the convex polytopes of the reduced density matrices. The model we study here is HAF on a square lattice with the first nearest neighbor and second nearest neighbor interactions in the presence of a magnetic

field. The goal is to analyze the geometric structure of reduced density matrices which are obtained from a tensor network ansatz for the ground state of the Hamiltonian.

Before we proceed further it is important to note that fundamental insights to utilize the geometric structure of reduced density matrices in the tensor networks context were made by Verstraete et al. in [92]. Later Zauner et al. in [93] rigorously investigated those ideas by studies related to symmetry breaking in classical and quantum systems. Chen et al. did similar studies in [94] with a focus on symmetry protected topological phases.

6.3.1 Geometry of reduced density matrices

The reduced density matrices form a convex set, and there is a very useful consequence of the convexity property: given a collection of observables $\{A_1, A_2, ...A_n\}$, the set of points which are associated with the expectation values of the observables $\{\mathrm{Tr}(A_1\rho), \mathrm{Tr}(A_2\rho), ...\mathrm{Tr}(A_n\rho)\}$ is also convex.

Consider a system defined on a lattice Λ with a Hamiltonian which is a sum of local operators, $H = \sum_{x\in\Lambda} h^{[x]}$. Then the problem of finding the ground of H can be reduced to the optimization problem over the set of reduced density matrices,

$$\min_{\{\rho^{[x]}\}} \sum_{x\in\Lambda} \mathrm{Tr}\left(h^{[x]}\rho^{[x]}\right). \tag{6.11}$$

The above version of the energy minimization problem is known as the quantum marginal problem [95]. And it is important to note that the optimization has to be performed over the set of valid reduced density matrices σ that is there exists a global density matrix σ such that $\mathrm{Tr}_x(\sigma) = \rho^{[x]}$ for every x. Now, if H has the translation symmetry (i.e., the non-trivial action of $h^{[x]}$ is independent of x) then the optimization in (6.11) over a set of reduced density matrices can be restricted to a single reduced density matrix ρ,

$$\rho_0 = \arg\min_{\rho} \mathrm{Tr}\,(h\rho), \tag{6.12}$$

and ρ is subjected to be a valid reduced density matrix.

If each local term has a further structure, i.e., $h = \sum_{i=1}^{n} J_i h_i$ is a sum of competing terms, then the set of points $\mathcal{S} := \{\mathrm{Tr}(h_1\rho), \mathrm{Tr}(h_2\rho), ...\mathrm{Tr}(h_n\rho)\}$ form a convex set. Furthermore, the set of points $\{\mathrm{Tr}(h_1\rho_0), \mathrm{Tr}(h_2\rho_0), ...\mathrm{Tr}(h_n\rho_0)\}$ over the solutions $\rho_0(J_1, J_2, ..J_n)$ in (6.12) form a convex envelop within $\mathcal{S}$ [92].

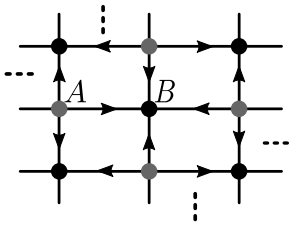

FIGURE 6.10: Top view of the tensor network of the variation ansatz for the ground state of HAF on a square lattice. Arrowheads denote the orientation of the singlets.

6.3.2 Geometric structure of tensor network ansatz - HAF on the square lattice

We begin by first writing down the Hamiltonian,

$$H = J_1 \sum_{\langle i,j \rangle} \boldsymbol{S}_i . \boldsymbol{S}_j + J_2 \sum_{\langle\langle i,j \rangle\rangle} \boldsymbol{S}_i . \boldsymbol{S}_j + h \sum_i S_z \tag{6.13}$$

The first two terms correspond to the first- and second nearest neighbor interactions. The third term explicitly breaks the $SU(2)$ symmetry of the Hamiltonian.

The ground state of H at the Heisenberg point ($J_2 = 0, h = 0$) has been studied to exhibit Néel phase, and Didier Poilblanc showed it in [96] that a tensor network ansatz with only one variational parameter can give an excellent description of the ground state wavefunction. The variational ansatz can be constructed by starting with nearest neighbor resonating valence (RVB) state on a square lattice (Fig. 6.10) and by doping the RVB wavefunction by spinons with opposite polarity on the lattice sites A and B. The addition of doping term to RVB wavefunction breaks the physical $SU(2)$ symmetry, but the well-defined orientation of spinons preserve the $U(1)$ symmetry.

The tensor network description of the wavefunction can be given be defining on-site tensors for the A and B lattice sites,

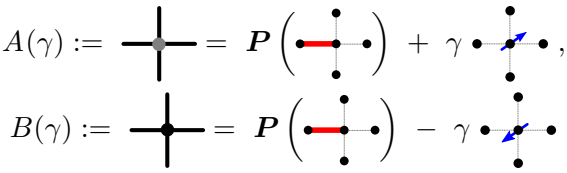

(6.14)

The bubble in center denote the physical index or particle, and the open ends specify the virtual indices or particles. Red lines indicate a maximally entangled state (i.e., the virtual particles at the end are bounded as $\frac{1}{\sqrt{2}}(|00\rangle + |11\rangle)$). Black bubbles on the RHS indicate particles in the state $|2\rangle$. Blue arrows with up and down orientation denote physical particle in the state $|0\rangle$ and $|1\rangle$ respectively. The operator $\boldsymbol{P}$ acts on the four virtual legs, and it is defined as $\boldsymbol{P} := (\mathbb{I} + \boldsymbol{R} + \boldsymbol{R}^2 + \boldsymbol{R}^3)$, where $\boldsymbol{R}$ is the generator of the

cyclic group $\mathbb{Z}_4$, and it produces a rotation in the anti-clockwise direction. Pictorially the action of $\boldsymbol{R}$ can be given as,

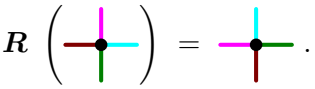

(6.15)

The tensor network of the ansatz is obtained by the putting on-site tensors on the lattices sites and joining the virtual indices of on-sites with a singlet tensor which could be denoted as  $:= \begin{pmatrix} 0 & -1 \\ 1 & 0 \end{pmatrix}$. The resulting tensor network is shown in Fig. 6.10. By tuning the value of γ, one can get a very good approximation of the ground state at the Heisenberg point.

The definition of on-site tensors in (6.14) only allow for the possibility of nearest neighbor (NN) singlet pairings in the RVB wavefunction. Wang et al. have shown in [97] that the tensor network description of the NN RVB wavefunction can be appended very simply to allow for the possibility of long-range singlet pairings.

$A(c) = B(c) :=$ 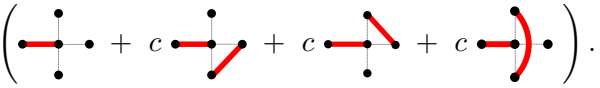

(6.16)

The definition of $\boldsymbol{P}$, and by putting on-site tensors together as in Fig. 6.10 one can get an RVB state with long-range singlets. The first term on the RHS generate the NN singlet pairings. The last three terms allow for long-range singlets between the lattice sites A and B. Due to the orientation of arrows the ansatz (6.16) only allow for the singlet pairings between A and B lattice sites. By optimizing the variational ansatz in (6.16) as a function of c, Wang et al. were able to get a variational description of the ground state of H at $(J_1 = 0.5J_2, h = 0)$ point.

Now we combine the two ansatzes in (6.14) and (6.16), and analyze the structure of reduced density metrics for the resulting ansatz.

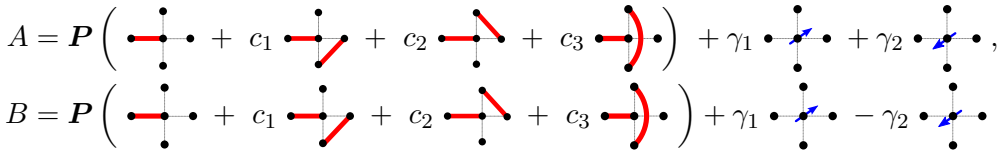

(6.17)

Five variables parameterize the variational manifold. We compute the expectation value of observables $E_1 = \langle S_i.S_{i+1}\rangle$, $E_2 = \langle S_i.S_{i+2}\rangle$ and $M = \langle S_z\rangle$ for random states within the five parameter variational manifold. The 3D plot containing the expectation values of these observables gives a projection of the set of reduced density matrices. The convex hull of the data points gives a convex polytope (Fig. 6.11). The states on the surface of the polytope correspond to the ground state of the H. Red data point of the surface of the polytope represents the Néel state (i.e., the optimal energy state which have been

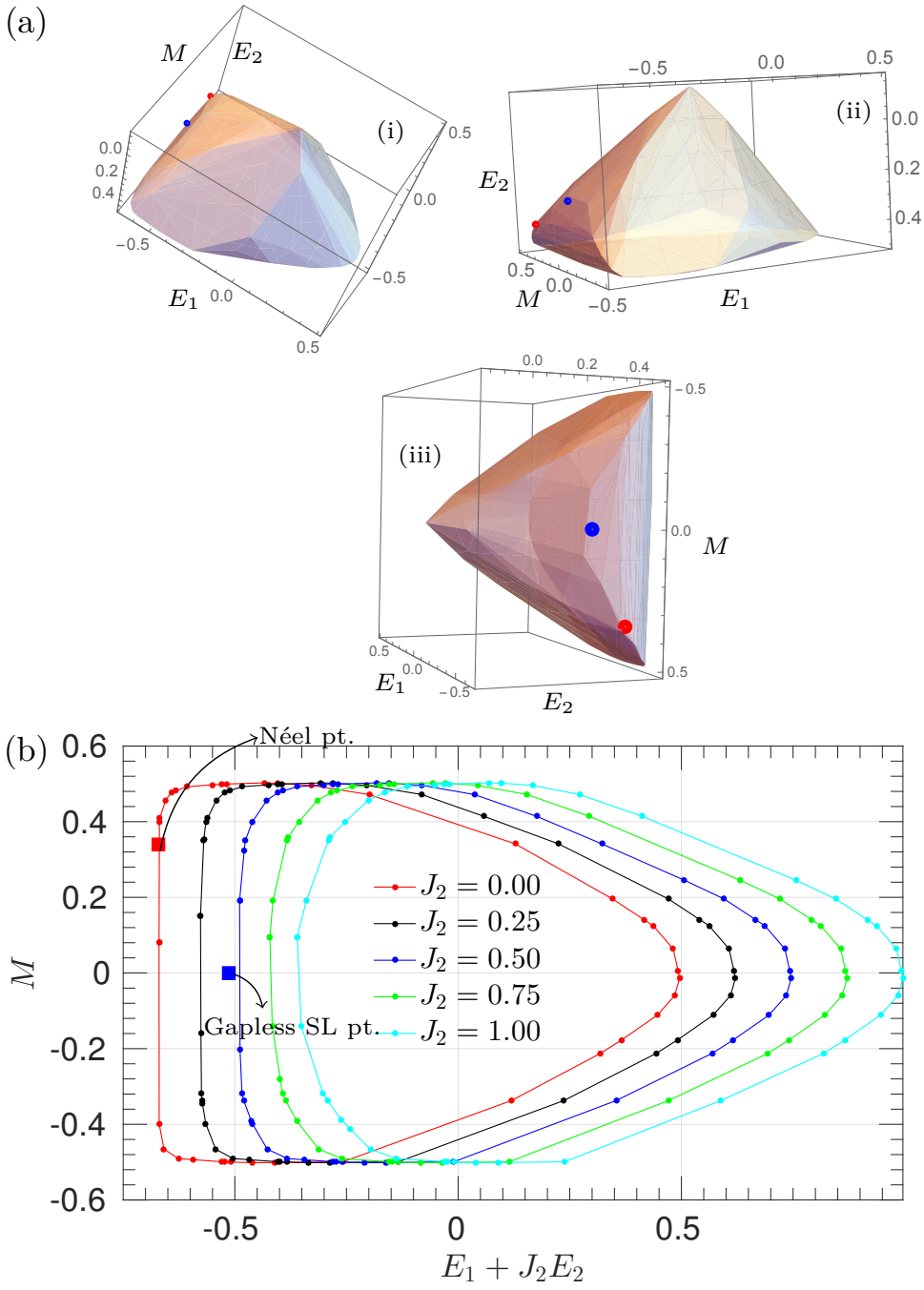

FIGURE 6.11: (a) Three different views of the convex polytope generated from a data set of more than 50,000 points. The expectation values have been computed by iMPS algorithm (b) Sliced views of the polytope in (a) for different values of J_2.

computed from the spinon doping ansatz of Didier Poiblanc in 6.14). The blue data point corresponds to the gapless spin liquid ansatz of Wang et al. in (6.16).

Although, there is a need for further analysis, and as suggested in [93] we also observe the appearance of a ruled surface[1]. The ruled surface is most visible in Fig. 6.11a(iii)

[1]A ruled surface is a surface which could be traced by moving a line in an ambient space.

between the blue point and the rightmost line on the polytope. The ruled surface signifies the presence of explicit symmetry breaking in the Hamiltonian.

6.4 Summary and outlook

An efficient (requires a few variational parameters) description for the ground state of HAF of the kagome lattice in $\mathbb{Z}_2$ spin liquid phase can be obtained by using tensor networks. Furthermore, the analysis of the geometric structure of reduced density matrices enables a new way to the explore different features of the many-body Hamiltonians.

One obvious difficulty in studying the double semion spin liquid as ansatz for the ground state of HAF is that the local tensor description of the variational ansatz would require a large bond dimension. As an outlook, this difficulty can be resolved by the development of new local tensor approximation strategies which preserve the virtual $\mathbb{Z}_4$ symmetries while doing the truncations.

Chapter 7

Conclusions and outlook

The approach to analyze the entanglement structure of a quantum many-body system by dividing the wavefunction into local tensors as formulated by the tensor network framework is a robust method for studying quantum phase transitions which include both topologically trivial and nontrivial phases of matter. Besides enabling the usage of other remarkable probes such an anyon-anyon correlation functions, tensor networks also offer a natural way to examine the condensation and confinement of anyons and allow us to extract the universal features of topological phase transitions.

The set of $\mathbb{Z}_4$-invariant tensors includes the phases of $D(\mathbb{Z}_4)$ quantum doubles, the toric code model, the double semion model, and trivial phases. The different tensor network realizations of these phases can be labeled by different patterns of symmetry breaking in the fixed points of the transfer operator. The phase diagram of $\mathbb{Z}_4$-invariant tensors exhibits a rich variety of behavior. The phase transitions from $D(\mathbb{Z}_4)$ quantum double to the toric code, to the double semion model, and to a trivial phase (i.e., the $\mathbb{Z}_2 \boxtimes \mathbb{Z}_2$ trivial phase) are continuous and typically lie in the Ising universality class. The phase boundaries of the toric code and double semion model allow for the first-order phase transitions. However, it is also possible to induce continuous phase transitions between the toric code and double semion model which could lie either in the Ising universality class or the universality class of the Ashkin-Teller model. Typically, the Ising universality class characterizes the phase transitions from the toric code model to the trivial phases. A first-order phase transition has also been observed between the double semion model and the $\mathbb{Z}_4 \boxtimes \mathbb{Z}_4$ trivial phase. We also observe a continuous change in the universality of the phase transitions across the phase boundaries of the double semion model and $\mathbb{Z}_2 \boxtimes \mathbb{Z}_2$ trivial phase.

By enriching the topological structure (i.e., the G-invariance of local tensors) with physical symmetries such as $SU(2)$ enable the study of quantum spin liquids. In the case

of $\mathbb{Z}_2$-invariant tensors, while also considering physical symmetries (i.e., the lattice and the spin rotation symmetries), the phase diagram contains the gapped spin liquid phase, the valence bond crystal phase and the spinon doped phase. The spin liquid phase preserves all the physical symmetries, the valence bond crystal phase breaks the lattice symmetries, and the spinon doped phase breaks the $SU(2)$ symmetry. However, the anyon condensation governs the phase transitions from the gapped $\mathbb{Z}_2$ spin liquid phase. The condensation of visons drives the system from the spin liquid to the valence bond crystal phase. On the other hand, the condensation of spinons induces phase transition to a spinon doped phase. The behavior of the system at the phase boundaries cannot be explained by the conventional local order parameters associated with the broken symmetries.

Furthermore, by enhancing the topological structure of local tensors from $\mathbb{Z}_2$ to $\mathbb{Z}_4$, we can study the spin liquid states of toric code and double semion model in a unified framework. Gapped spin liquid with the double semion topological order is unusual in the sense that it carries semionic excitations and also preserves the spin symmetries but breaks the lattice symmetry. As an outlook, the systematic investigation of toric code and double semion spin liquid could potentially settle the strongly debated question regarding the true topological nature of the ground state of Heisenberg antiferromagnet (HAF) on the kagome lattice.

Tensor network states not only make the backbone of the numerical techniques but they also further the construction of variational ansatzes for the ground state wavefunction with a very compact description. The variational ansatz of resonating valence bond states with third neighbor singlets by using only one real parameter give an energy density of -0.4275 for the ground state of HAF which is fairly close to the energy density from DMRG calculations that is -0.4385. Moreover, tensor networks framework allows for a systematic increase of entanglement (i.e., by increasing the bond dimension) which in turn also increase the computational complexity of the variational ansatz. Only a few variables parametrize the extended ansatz of simplex resonating valence bond states which include highly entangled wavefunctions. The optimization over the three-parameter family of simplex resonating valence bond states gives an energy density of -0.4335(2) which has a relative difference of about 1% with state of the art DMRG results. Furthermore, it can be shown that optimal energy state from the three parameters variational ansatz lies in the gapped $\mathbb{Z}_2$ spin liquid and the spinon gap is finite.

As a concluding remark, tensor network framework offer a promising endeavor for the simulation of quantum systems on classical hardware, and the success of this field does not rely upon the reliable implementation of a large-scale quantum computer.

Bibliography

[1] Luigi Amico, Rosario Fazio, Andreas Osterloh, and Vlatko Vedral. Entanglement in many-body systems. *Reviews of modern physics*, 80(2):517, 2008.

[2] Ryszard Horodecki, Paweł Horodecki, Michał Horodecki, and Karol Horodecki. Quantum entanglement. *Reviews of modern physics*, 81(2):865, 2009.

[3] Frank Verstraete and J Ignacio Cirac. Renormalization algorithms for quantum-many body systems in two and higher dimensions. *arXiv preprint cond-mat/0407066*, 2004.

[4] Xiao-Gang Wen. *Quantum field theory of many-body systems: from the origin of sound to an origin of light and electrons*. Oxford University Press on Demand, 2004.

[5] Lev Davidovich Landau. On the theory of phase transitions. i. *Zh. Eksp. Teor. Fiz.*, 11:19, 1937.

[6] LD Landau. Em lifshitz statistical physics. *Course of Theoretical Physics*, 5:230, 1958.

[7] A Yu Kitaev. Fault-tolerant quantum computation by anyons. *Annals of Physics*, 303(1):2–30, 2003.

[8] Michael Freedman, Alexei Kitaev, Michael Larsen, and Zhenghan Wang. Topological quantum computation. *Bulletin of the American Mathematical Society*, 40(1): 31–38, 2003.

[9] Norbert Schuch, Ignacio Cirac, and David Perez-Garcia. Peps as ground states: degeneracy and topology. *Annals of Physics*, 325(10):2153–2192, 2010.

[10] Oliver Buerschaper. Twisted injectivity in projected entangled pair states and the classification of quantum phases. *Annals of Physics*, 351:447–476, 2014.

[11] Mehmet Burak Şahinoğlu, Dominic Williamson, Nick Bultinck, Michael Mariën, Jutho Haegeman, Norbert Schuch, and Frank Verstraete. Characterizing topological order with matrix product operators. *arXiv preprint arXiv:1409.2150*, 2014.

[12] FA Bais and JK Slingerland. Condensate-induced transitions between topologically ordered phases. *Physical Review B*, 79(4):045316, 2009.

[13] Jutho Haegeman, Valentin Zauner, Norbert Schuch, and Frank Verstraete. Shadows of anyons and the entanglement structure of topological phases. *Nature communications*, 6, 2015.

[14] PW Anderson. The resonating valence bond state in la2cuo4 and superconductivity. 1987.

[15] Steven A Kivelson, Daniel S Rokhsar, and James P Sethna. Topology of the resonating valence-bond state: Solitons and high-t c superconductivity. *Physical Review B*, 35(16):8865, 1987.

[16] Didier Poilblanc, Norbert Schuch, David Pérez-García, and J Ignacio Cirac. Topological and entanglement properties of resonating valence bond wave functions. *Physical Review B*, 86(1):014404, 2012.

[17] Norbert Schuch, Didier Poilblanc, J Ignacio Cirac, and David Pérez-García. Resonating valence bond states in the peps formalism. *Physical Review B*, 86(11): 115108, 2012.

[18] Lucile Savary and Leon Balents. Quantum spin liquids. *arXiv preprint arXiv:1601.03742*, 2016.

[19] Michael Freedman, Chetan Nayak, Kirill Shtengel, Kevin Walker, and Zhenghan Wang. A class of p, t-invariant topological phases of interacting electrons. *Annals of Physics*, 310(2):428–492, 2004.

[20] Simeng Yan, David A Huse, and Steven R White. Spin-liquid ground state of the s= 1/2 kagome heisenberg antiferromagnet. *Science*, 332(6034):1173–1176, 2011.

[21] Stefan Depenbrock, Ian P McCulloch, and Ulrich Schollwöck. Nature of the spin-liquid ground state of the s= 1/2 heisenberg model on the kagome lattice. *Physical review letters*, 109(6):067201, 2012.

[22] Steven R White. Density matrix formulation for quantum renormalization groups. *Physical review letters*, 69(19):2863, 1992.

[23] Stellan Östlund and Stefan Rommer. Thermodynamic limit of density matrix renormalization. *Physical review letters*, 75(19):3537, 1995.

[24] Jorge Dukelsky, Miguel A Martín-Delgado, Tomotoshi Nishino, and Germán Sierra. Equivalence of the variational matrix product method and the density matrix renormalization group applied to spin chains. *EPL (Europhysics Letters)*, 43(4):457, 1998.

[25] Ian Affleck, Tom Kennedy, Elliott H Lieb, and Hal Tasaki. Rigorous results on valence-bond ground states in antiferromagnets. *Physical review letters*, 59(7):799, 1987.

[26] Reinhard F Werner. Quantum states with einstein-podolsky-rosen correlations admitting a hidden-variable model. *Physical Review A*, 40(8):4277, 1989.

[27] Michael A Nielsen and Isaac Chuang. Quantum computation and quantum information, 2002.

[28] Matthew B Hastings. An area law for one-dimensional quantum systems. *Journal of Statistical Mechanics: Theory and Experiment*, 2007(08):P08024, 2007.

[29] Alexei Kitaev and John Preskill. Topological entanglement entropy. *Physical review letters*, 96(11):110404, 2006.

[30] Michael Levin and Xiao-Gang Wen. Detecting topological order in a ground state wave function. *Physical review letters*, 96(11):110405, 2006.

[31] Hong-Chen Jiang, Zhenghan Wang, and Leon Balents. Identifying topological order by entanglement entropy. *Nature Physics*, 8(12):902–905, 2012.

[32] Zheng-Cheng Gu, Michael Levin, Brian Swingle, and Xiao-Gang Wen. Tensor-product representations for string-net condensed states. *Physical Review B*, 79(8): 085118, 2009.

[33] Frank Verstraete, Michael M Wolf, David Perez-Garcia, and J Ignacio Cirac. Criticality, the area law, and the computational power of projected entangled pair states. *Physical review letters*, 96(22):220601, 2006.

[34] Linus Pauling. A resonating-valence-bond theory of metals and intermetallic compounds. In *Proceedings of the Royal Society of London A: Mathematical, Physical and Engineering Sciences*, volume 196, pages 343–362. The Royal Society, 1949.

[35] Guifré Vidal. Efficient classical simulation of slightly entangled quantum computations. *Physical Review Letters*, 91(14):147902, 2003.

[36] Frank Verstraete, Juan J Garcia-Ripoll, and Juan Ignacio Cirac. Matrix product density operators: simulation of finite-temperature and dissipative systems. *Physical review letters*, 93(20):207204, 2004.

[37] Guifré Vidal. Efficient simulation of one-dimensional quantum many-body systems. *Physical review letters*, 93(4):040502, 2004.

[38] Ian P McCulloch. Infinite size density matrix renormalization group, revisited. *arXiv preprint arXiv:0804.2509*, 2008.

[39] Roman Orus and Guifre Vidal. Infinite time-evolving block decimation algorithm beyond unitary evolution. *Physical Review B*, 78(15):155117, 2008.

[40] Philippe Corboz. Variational optimization with infinite projected entangled-pair states. *Physical Review B*, 94(3):035133, 2016.

[41] Laurens Vanderstraeten, Jutho Haegeman, Philippe Corboz, and Frank Verstraete. Gradient methods for variational optimization of projected entangled-pair states. *Physical Review B*, 94(15):155123, 2016.

[42] Jutho Haegeman and Frank Verstraete. Diagonalizing transfer matrices and matrix product operators: a medley of exact and computational methods. *Annual Review of Condensed Matter Physics*, 8:355–406, 2017.

[43] J Ignacio Cirac, Didier Poilblanc, Norbert Schuch, and Frank Verstraete. Entanglement spectrum and boundary theories with projected entangled-pair states. *Physical Review B*, 83(24):245134, 2011.

[44] Norbert Schuch, Didier Poilblanc, J Ignacio Cirac, and David Perez-Garcia. Topological order in the projected entangled-pair states formalism: Transfer operator and boundary hamiltonians. *Physical review letters*, 111(9):090501, 2013.

[45] Hui Li and F Duncan M Haldane. Entanglement spectrum as a generalization of entanglement entropy: Identification of topological order in non-abelian fractional quantum hall effect states. *Physical review letters*, 101(1):010504, 2008.

[46] Paolo Zanardi and Nikola Paunković. Ground state overlap and quantum phase transitions. *Physical Review E*, 74(3):031123, 2006.

[47] Huan-Qiang Zhou, Roman Orús, and Guifre Vidal. Ground state fidelity from tensor network representations. *Physical review letters*, 100(8):080601, 2008.

[48] Marco Cozzini, Radu Ionicioiu, and Paolo Zanardi. Quantum fidelity and quantum phase transitions in matrix product states. *Physical Review B*, 76(10):104420, 2007.

[49] Paolo Zanardi, Paolo Giorda, and Marco Cozzini. Information-theoretic differential geometry of quantum phase transitions. *Physical review letters*, 99(10):100603, 2007.

[50] Jutho Haegeman, Tobias J Osborne, and Frank Verstraete. Post-matrix product state methods: To tangent space and beyond. *Physical Review B*, 88(7):075133, 2013.

[51] David Perez-Garcia, Frank Verstraete, Michael M Wolf, and J Ignacio Cirac. Matrix product state representations. *arXiv preprint quant-ph/0608197*, 2006.

[52] Ulrich Schollwöck. The density-matrix renormalization group in the age of matrix product states. *Annals of Physics*, 326(1):96–192, 2011.

[53] Valentin Zauner, Damian Draxler, Laurence Vanderstraeten, Matthias Degroote, Jutho Haegeman, Marek M Rams, Vid Stojevic, Norbert Schuch, and Frank Verstraete. Transfer matrices and excitations with matrix product states. *New Journal of Physics*, 17(5):053002, 2015.

[54] B Pirvu, F Verstraete, and G Vidal. Exploiting translational invariance in matrix product state simulations of spin chains with periodic boundary conditions. *Physical Review B*, 83(12):125104, 2011.

[55] Jutho Haegeman, Bogdan Pirvu, David J Weir, J Ignacio Cirac, Tobias J Osborne, Henri Verschelde, and Frank Verstraete. Variational matrix product ansatz for dispersion relations. *Physical Review B*, 85(10):100408, 2012.

[56] Xiao-Gang Wen. Vacuum degeneracy of chiral spin states in compactified space. *Physical Review B*, 40(10):7387, 1989.

[57] Xiao-Gang Wen and Qian Niu. Ground-state degeneracy of the fractional quantum hall states in the presence of a random potential and on high-genus riemann surfaces. *Physical Review B*, 41(13):9377, 1990.

[58] Xiao-Gang Wen. Topological orders in rigid states. *International Journal of Modern Physics B*, 4(02):239–271, 1990.

[59] Matthew B Hastings and Xiao-Gang Wen. Quasiadiabatic continuation of quantum states: The stability of topological ground-state degeneracy and emergent gauge invariance. *Physical review b*, 72(4):045141, 2005.

[60] Bei Zeng, Xie Chen, Duan-Lu Zhou, and Xiao-Gang Wen. Quantum information meets quantum matter–from quantum entanglement to topological phase in many-body systems. *arXiv preprint arXiv:1508.02595*, 2015.

[61] Alexander F Bais, Bernd J Schroers, and Joost K Slingerland. Hopf symmetry breaking and confinement in (2+ 1)-dimensional gauge theory. *Journal of High Energy Physics*, 2003(05):068, 2003.

[62] F Alexander Bais, Bernd J Schroers, and Joost K Slingerland. Broken quantum symmetry and confinement phases in planar physics. *Physical review letters*, 89 (18):181601, 2002.

[63] Kasper Duivenvoorden, Mohsin Iqbal, Jutho Haegeman, Frank Verstraete, and Norbert Schuch. Entanglement phases as holographic duals of anyon condensates. *arXiv preprint arXiv:1702.08469*, 2017.

[64] Michael A Levin and Xiao-Gang Wen. String-net condensation: A physical mechanism for topological phases. *Physical Review B*, 71(4):045110, 2005.

[65] Mohsin Iqbal, Didier Poilblanc, and Norbert Schuch. Semionic resonating valence-bond states. *Physical Review B*, 90(11):115129, 2014.

[66] Claudio Castelnovo and Claudio Chamon. Quantum topological phase transition at the microscopic level. *Physical Review B*, 77(5):054433, 2008.

[67] Jutho Haegeman, Karel Van Acoleyen, Norbert Schuch, J Ignacio Cirac, and Frank Verstraete. Gauging quantum states: from global to local symmetries in many-body systems. *Physical Review X*, 5(1):011024, 2015.

[68] Bogdan Pirvu, Jutho Haegeman, and Frank Verstraete. Matrix product state based algorithm for determining dispersion relations of quantum spin chains with periodic boundary conditions. *Physical Review B*, 85(3):035130, 2012.

[69] Huan-Qiang Zhou, Roman Orús, and Guifre Vidal. Ground state fidelity from tensor network representations. *Physical review letters*, 100(8):080601, 2008.

[70] David Aasen, Roger SK Mong, and Paul Fendley. Topological defects on the lattice i: The ising model. *arXiv preprint arXiv:1601.07185*, 2016.

[71] Siddhardh C Morampudi, Curt Von Keyserlingk, and Frank Pollmann. Numerical study of a transition between z 2 topologically ordered phases. *Physical Review B*, 90(3):035117, 2014.

[72] Jutho Haegeman, David Pérez-García, Ignacio Cirac, and Norbert Schuch. Order parameter for symmetry-protected phases in one dimension. *Physical Review Letters*, 109(5):050402, 2012.

[73] Kasper Duivenvoorden and Thomas Quella. From symmetry-protected topological order to landau order. *Physical Review B*, 88(12):125115, 2013.

[74] Claire Lhuillier and Grégoire Misguich. Frustrated quantum magnets. In *High magnetic fields*, pages 161–190. Springer, 2002.

[75] JS Helton, K Matan, MP Shores, EA Nytko, BM Bartlett, Y Yoshida, Y Takano, A Suslov, Y Qiu, J-H Chung, et al. Spin dynamics of the spin-1/2 kagome lattice antiferromagnet zncu 3 (oh) 6 cl 2. *Physical Review Letters*, 98(10):107204, 2007.

[76] P Mendels, F Bert, MA De Vries, A Olariu, A Harrison, F Duc, JC Trombe, JS Lord, A Amato, and C Baines. Quantum magnetism in the paratacamite family: towards an ideal kagomé lattice. *Physical review letters*, 98(7):077204, 2007.

[77] Tian-Heng Han, Joel S Helton, Shaoyan Chu, Daniel G Nocera, Jose A Rodriguez-Rivera, Collin Broholm, and Young S Lee. Fractionalized excitations in the spin-liquid state of a kagome-lattice antiferromagnet. *Nature*, 492(7429):406–410, 2012.

[78] PWAP Fazekas and PW Anderson. On the ground state properties of the anisotropic triangular antiferromagnet. *Philosophical Magazine*, 30(2):423–440, 1974.

[79] Daniel S Rokhsar and Steven A Kivelson. Superconductivity and the quantum hard-core dimer gas. *Physical review letters*, 61(20):2376, 1988.

[80] Veit Elser and Chen Zeng. Kagomé spin-1/2 antiferromagnets in the hyperbolic plane. *Physical Review B*, 48(18):13647, 1993.

[81] G Misguich, D Serban, and V Pasquier. Quantum dimer model on the kagome lattice: Solvable dimer-liquid and ising gauge theory. *Physical review letters*, 89 (13):137202, 2002.

[82] Mohsin Iqbal. Semionic resonating valence bond states on the kagome lattice. Master's thesis, RWTH Aachen University, 2013.

[83] Didier Poilblanc and Norbert Schuch. Simplex z 2 spin liquids on the kagome lattice with projected entangled pair states: Spinon and vison coherence lengths, topological entropy, and gapless edge modes. *Physical Review B*, 87(14):140407, 2013.

[84] Andreas M Läuchli, Julien Sudan, and Roderich Moessner. The $s = 1/2$ kagome heisenberg antiferromagnet revisited. *arXiv preprint arXiv:1611.06990*, 2016.

[85] Yin-Chen He, Michael P Zaletel, Masaki Oshikawa, and Frank Pollmann. Signatures of dirac cones in a dmrg study of the kagome heisenberg model. *Physical Review X*, 7(3):031020, 2017.

[86] Yasir Iqbal, Federico Becca, Sandro Sorella, and Didier Poilblanc. Gapless spin-liquid phase in the kagome spin-1 2 heisenberg antiferromagnet. *Physical Review B*, 87(6):060405, 2013.

[87] HJ Liao, ZY Xie, J Chen, ZY Liu, HD Xie, RZ Huang, B Normand, and T Xiang. Gapless spin-liquid ground state in the s= 1/2 kagome antiferromagnet. *Physical Review Letters*, 118(13):137202, 2017.

[88] Yang Qi, Zheng-Cheng Gu, and Hong Yao. Double-semion topological order from exactly solvable quantum dimer models. *Physical Review B*, 92(15):155105, 2015.

[89] Oliver Buerschaper, Siddhardh C Morampudi, and Frank Pollmann. Double semion phase in an exactly solvable quantum dimer model on the kagome lattice. *Physical Review B*, 90(19):195148, 2014.

[90] Chen Zeng and Veit Elser. Quantum dimer calculations on the spin-1/2 kagomé heisenberg antiferromagnet. *Physical Review B*, 51(13):8318, 1995.

[91] ZY Xie, Jing Chen, MP Qin, JW Zhu, LP Yang, and Tao Xiang. Coarse-graining renormalization by higher-order singular value decomposition. *Physical Review B*, 86(4):045139, 2012.

[92] Frank Verstraete and J Ignacio Cirac. Matrix product states represent ground states faithfully. *Physical Review B*, 73(9):094423, 2006.

[93] V Zauner, D Draxler, Laurens Vanderstraeten, Jutho Haegeman, and Frank Verstraete. Symmetry breaking and the geometry of reduced density matrices. *New Journal of Physics*, 18(11):113033, 2016.

[94] Ji-Yao Chen, Zhengfeng Ji, Zheng-Xin Liu, Yi Shen, and Bei Zeng. Geometry of reduced density matrices for symmetry-protected topological phases. *Physical Review A*, 93(1):012309, 2016.

[95] Alexander A Klyachko. Quantum marginal problem and n-representability. In *Journal of Physics: Conference Series*, volume 36, page 72. IOP Publishing, 2006.

[96] Didier Poilblanc. Entanglement hamiltonian of the quantum néel state. *Journal of Statistical Mechanics: Theory and Experiment*, 2014(10):P10026, 2014.

[97] Ling Wang, Didier Poilblanc, Zheng-Cheng Gu, Xiao-Gang Wen, and Frank Verstraete. Constructing a gapless spin-liquid state for the spin-1/2 j 1- j 2 heisenberg model on a square lattice. *Physical review letters*, 111(3):037202, 2013.

Acknowledgments

First of all, I would like to thank my doctoral advisor Norbert Schuch for giving me the opportunity to work in his group. I thank him for being an excellent teacher and heartily appreciate the effort and patience he has put in explaining different things to me during the last four years. The valuable lessons I have learned from him will profit me for the rest of my life.

I would also like to thank Kasper Duivenvoorden for the scientific collaboration we had and most importantly for being a good friend. It was a great pleasure to work with him.

I am grateful to Manuel Risplar for being a wonderful friend and a great officemate. I strongly appreciate his help on many different occasions. I would also like to thank Thilo Plucker and Micheal Hell for being good officemates during the first half of my Ph.D. studies in Aachen. I am also grateful to my officemates Ivana Kurečić, David Stephen, and Caroline De Groot during my stay at MPQ. I am also thankful to my friends Nikolas Breuckmann, Susanne Richer, Firat Solgun, Lauri Lehman, Andreas Bauer, Anna Hackenbroich, Henrik Dreyer, Johannes Knörzer, Andras Molnar, Nicola Pancotti, Julian Roos, Stefan Kühn, Asli Cakan, Andrew Goldsborough, Antoine Sterdyniak and many others at JARA IQI and MPQ, and most importantly to Gillian Hewitt, Helene Barton, and Andrea Kluth for their help on different problems. I am thankful to my friend Jamshaid Ali for the delightful/frustrated conversations during the whole course of my studies.

Last but most importantly, I am deeply grateful to my family especially my parents for their unconditional love and support during all the critical periods of my life.

Declaration

I, Mohsin Iqbal, declare that this thesis titled, 'Topological Phenomena in Tensor Network States of Quantum Spin Systems' and the work presented in it are my own. I confirm that:

- This work was done wholly or mainly while in candidature for a research degree at RWTH Aachen University.
- The findings presented in the chapter titled, 'Anyon condensation and topological phase transitions' were found in collaboration with Norbert Schuch and Kasper Duivenvoorden and these results have already appeared in the preprint archive, arXiv: 1712.04021. There are some numerical results in the chapter which have appeared in the related paper 'Entanglement phases as holographic duals of anyon condensates' (Phys. Rev. B 95, 235119, 2017), and I am using only those results in this thesis where I contributed in that paper.
- The results presented in the chapters titled, 'Toric code and double semion spin liquids' and 'Spin liquid ansatzes for the ground state of Heisenberg antiferromagnet' were found in collaboration with Norbert Schuch. The work on the phase diagram of gapped $\mathbb{Z}_2$ spin liquids was performed in collaboration with Helena Casademunt. The results regarding the entanglement properties of semionic resonating valence bond states and simplex semionic resonating valence bond states were found in collaboration with Didier Poilblanc and Norbert Schuch, and these findings have already appeared in the paper 'Semionic resonating valence-bond states' (Phys. Rev. B 90, 115129, 2014). I am using only those results about semionic resonating valence bond states in this thesis on which I worked while I was enrolled as a Ph.D. student.
- Where I have consulted the published work of others, this is always clearly attributed.